Yokohama National Univeristy

Dissertation

博士論文

Ab initio study of electronic structure and carrier localization in two-dimensional materials

（第一原理計算による二次元物質の電子構造と
キャリアの局在化の究研）

横浜国立大学大学院

理工学府

Soungmin Bae

ベ　ソンミン

裵 星旻

Acknowledgements

I am pleased to write these acknowledgements at the end of a long journey that has lasted eight years since my first research activity in 2013. Despite many difficult moments in my academic career so far, I could continue my research until now thank to warm encouragements and valuable advices from my advisors, colleagues, friends, and my family. I would like to express my heartfelt gratitude to each and every one of them.

First and foremost, I would like to thank my advisor, Prof. Hannes Raebiger. During my master and doctoral courses, he taught me not only research skills and knowledge but also the attitude and mindset as a scientist. I would also like to express my gratitude to Prof. Yong-Hoon Kim, my previous PI in Korea Institute of Science and Technology (KAIST), for providing me the excellent opportunity for valuable research experience at his group during one year and a half. I especially thank Prof. Mohammad Khazaei, Mr. Yoon-Gu Kang, and Mr. Noriyuki Egawa for their significant contributions to my dissertation work. I owe debt of gratitudes to faculty members of this department: Prof. Kaoru Ohno, Prof. Ken-ichi Shudo, Prof. Jun Takeda, and Prof. Ikufumi Katayama of Yokohama National University. Again I sincerely thank them for many advices and supports.

I thank my collaborators for valuable discussions: Prof. Yeon-Ho Im at Jeonbuk National University, Dr. Tae Young Jeong and Prof. Ki Ju Yee at Chungnam National University, Prof. Seokhyun Yoon at Ewha Woman's University, Prof. Myung Joon Han and Prof. Kee Joo Chang at KAIST.

I would like to express appreciation to my old colleagues. Alumni of the Solid States and Molecule Theory Group (SSMT): Dr. Yoshida Daisuke, Mr. Toshiya Kagawa, Dr. Takeshi Fujita, Mr. Hikaru Nakayama, Mrs. Ririe Tadokoro, Mr. Koichi Koshino, Mr. Kodai Ichihashi, and Mr. Riku Shirota. Alumni of Ohno group: Prof. Shota Ono, Mr. Toru Shoji, Dr. Tsubasa Aoki, Dr. Kazuaki Kuwahata, and Prof. Yusuke Noda. First principles nano device lab in KAIST: Dr. Juho Lee, Dr. Muhammad Ejaz Khan, Dr. Min Jong Noh, Dr. Junga Ryou, Mr. Tae-Hyung Kim, Mr. Hyeonwoo Yeo, Dr. Hu Sung Kim, and Mr. Seongjae Byeon.

I greatly thank my friends and colleagues. Colleagues in my research field: Dr. Rafael Costa-Amaral, Dr. Yasuhide Mochizuki, Dr. Juho Lee; My old friends of Department of Physics in YNU: Mr. Aoki, Mr. Fuseya, Mr. Okada, Mr. Isohata, Mr. Nakamaru, Mr. Fukunaga, Mr. Horiuchi; The YNU-ISC (international student center) members: Prof. Hanzawa, Prof. Kim, Prof. Yomota, Prof. Ogawa, Prof. Nakagawa, Prof. Kawano, Mrs. Suto; The members of Himawari Rotary Club: Mr. Usui, Mr. Tsuchiya and many others; Supporters of Iwaki Scholarship Foundation: Mr. Kikuchi and Mrs. Yamato; My old physics teacher Dr. Yong Hwan Lee and Mr. Hyunjin Kim, Administrative staffs: Mrs. Watanabe and Mrs. Jeon; Korea-Japan Joint Government Scholarship (KJJG) 10th generation members: Mr. G. Kang a.k.a. Sozan-Sensei (beikoku financial advisor of animated combat ships) and Mr. G Park a.k.a. Astrificus (the pioneer of 2D red pill material), Mr. J. Jeong, Mr. D. Kim, Mr. Y. Jeong, Mr. S. Baek, Mr. G. Shim, Mr. J. Jang, Mr. K. Han, and Mr. K. Yoon; 8th generation of KJJG: Mr. D. Shin, Mr. J. Hong; My dear neighbors: Mr. and Mrs. Watanabe (Amanoya) for everyday Japanese soba noodles, Mr. and Mrs. Hamada (Yakiniku Minae) for their wonderful place to drink.

Lastly, I would like to express my deepest gratitude and appreciation to my parents and family for their ultimate support.

List of Publications

This thesis consists of an overview of the following publications.

I. Electronic and magnetic properties of carbide MXenes—the role of electron correlations

Soungmin Bae, Yoon-Gu Kang, Mohammad Khazaei, Kaoru Ohno, Yong-Hoon Kim, Myung Joon Han, Kee Joo Chang, and Hannes Raebiger

Materials Today Advances, **9**, 100118 (2021)
DOI: doi.org/10.1016/j.mtadv.2020.100118

II. MXene Phase with C_3 Structure Unit: A Family of 2D Electrides

Soungmin Bae, William Espinosa-García, Yoon-Gu Kang, Noriyuki Egawa, Juho Lee, Kazuaki Kuwahata, Mohammad Khazaei, Kaoru Ohno, Yong-Hoon Kim, Myung Joon Han, Hideo Hosono, Gustavo M Dalpian, and Hannes Raebiger

Advanced Functional Materials, 2100009 (2021)
DOI: doi.org/10.1002/adfm.202100009 **Journal frontispiece**

III. Strain engineering to release trapped hole carriers in p-type haeckelite GaN

Soungmin Bae, Yoon-Gu Kang, Kodai Ichihashi, Mohammad Khazaei, Varghese Swamy, Myung Joon Han, Kee Joo Chang, Ken-ichi Shudo, and Hannes Raebiger

ACS applied electronic materials (Accepted November 8th, 2021)
DOI: doi.org/10.1021/acsaelm.1c00765

Other related publications by the author are listed below.

IV. Higher-order optical response of coherent phonons in transition metal dichalcogenides resolves acoustic phonon momentum

Soungmin Bae, Kana Matsumoto, Hannes Raebiger, Ken-ichi Shudo, jan Sele Handeg, Tadaaki Nagao, Masahiro Kitajima, Yuji Sakai, Xiang Zhang, Robert Vajtai, Pulickel Ajayan, Junichiro Kono, Jun Takeda, and Ikufumi Katayama
In preparation

V. Electronic structures of group III-V element haeckelite compounds: a Novel Family of Semiconductors, dirac semimetals, and topological insulators

Mohammad Khazaei, Ahmad Ranjbar, Yoon-Gu Kang, Yunye Liang,Rasoul Khaledialidusti, **Soungmin Bae**, Hannes Raebiger, Vei Wang, Myung Joon Han, Hiroshi Mizoguchi, Mohammad S. Bahramy, Thomas D. Khne, Rodion V. Belosludov,Kaoru Ohno, and Hideo Hosono
Advanced Functional Materials (in press)

VI. 伝導キャリアの局在性とその制御—原子レベルのスイッチングデバイスに向けて—

Hannes Raebiger and **Soungmin Bae**

セラミックス Vol. 56, No. 10, pp. 663-668 (2021)

Link

VII. Coherent phonon generation from ultrafast exciton trapping at defect complexes in two-dimensional materials

Soungmin Bae, Tae-Yong Jeong, Hannes Raebiger, Ki-Ju Yee and Yong-Hoon Kim
Submitted to *Physical Review Letters*

VIII. Parallel alignment of methylammonium cations in orthorhombic $CH_3NH_3PbCl_3$ single crystal observed by polarized micro-Raman scattering spectroscopy

Yejin Kim*, **Soungmin Bae***, Joohee Park, Trang Thi Thu Nguyen, Hye Ri Jung, Hye, William Jo, Yong-Hoon Kim, Hannes Raebiger, and Seokhyun Yoon

*co-first author (equal contribution)
Chemistry of Materials (under revision)

IX. Valley depolarization in monolayer transition-metal dichalcogenides with zone-corner acoustic phonons

Tae-Young Jeong*, **Soungmin Bae***, Seong-Yeon Lee, Suyong Jung, Yong-Hoon Kim, and Ki-Ju Yee

*co-first author (equal contribution)
Nanoscale **12**, 22487-22494 (2020)
DOI: doi.org/10.1039/D0NR04761A

X. Raman Scattering Studies of the Structural Phase Transitions in Single-Crystalline $CH_3NH_3PbCl_3$

Trang Thi Thu Nguyen, Yejin Kim, **Soungmin Bae**, Maryam Bari, Hye Ri Jung, William Jo, Yong-Hoon Kim, Zuo-Guang Ye, and Seokhyun Yoon

The journal of physical chemistry letters **10**, 3773-3781 (2020)
DOI: doi.org/10.1021/acs.jpclett.0c00920

XI. Control of hole localization in magnetic semiconductors by axial strain

Hannes Raebiger, **Soungmin Bae**, Carlos Echeverría-Arrondo, and Andrés Ayuela

Physical Review Materials **2**, 024402 (2018)
DOI: 10.1103/PhysRevMaterials.2.024402

XII. Defect-Induced Vibration Modes of Ar^+-Irradiated MoS_2

Soungmin Bae, Natsuki Sugiyama, Takatoshi Matsuo, Hannes Raebiger, Ken-ichi Shudo, and Koichi Ohno

Physical Review Applied **7**, 024001 (2017)
DOI: 10.1103/PhysRevApplied.7.024001

XIII. Critical metal-insulator transition due to nuclear quantum effects in Mn-doped GaAs

Soungmin Bae and Hannes Raebiger

Physical Review B **94**, 241115(R) (2016) (Rapid communication)
DOI: 10.1103/PhysRevB.94.241115

XIV. Phonon Properties of Few-Layer Crystals of Quasi-One-Dimensional ZrS_3 and $ZrSe_3$

Kazuki Osada*, **Soungmin Bae***, Masatoshi Tanaka, Hannes Raebiger, Ken-ichi Shudo, and Takanori Suzuki

*co-first author (equal contribution)
The Journal of Physical Chemistry C **120**, 4653-4659 (2016)
DOI: doi.org/10.1021/acs.jpcc.5b12441

Contents

1 Introduction **1**
1.1 Two-dimensional transition metal carbides and nitrides (MXene) 2
1.2 Low-dimensional GaN and its application 5
1.3 Chapter overview 8

2 Theoretical framework **11**
2.1 Density-functional theory 11
2.2 Approximations of exchange-correlation functionals 13
2.2.1 Local density approximation (LDA) 14
2.2.2 Generalized gradient approximation (GGA) 15
2.2.3 Meta-generalized gradient approximation (MGGA) . . . 17
2.2.4 Hybrid functional 18
2.3 DFT+U formalism 19
2.4 Plane waves and pseudopotentials 21
2.5 The projector augmented-wave (PAW) method 21
2.6 Computational details of self-consistent DFT calculations 23

3 *Ab initio* prediction of electronic and magnetic properties of carbide MXenes **25**
3.1 Research backgroud 26
3.2 Computational details 26
3.3 Structural and electronic properties of M_2CO_2 MXenes 26
3.3.1 Atomic configurations of M_2CT_2 MXenes 26
3.3.2 Formal oxidation numbers and related properties 28
3.3.3 Ground state configurations predicted by various XC functionals 29
3.4 Electronic and magnetic properties of carbide MXenes 30
3.4.1 d^0-type1 MXenes: Sc_2CO_2, Y_2CO_2, La_2CO_2 31
3.4.2 d^0-type2 MXenes: Ti_2CO_2, Zr_2CO_2, Hf_2CO_2, Sc_2CF_2, Y_2CF_2, and La_2CF_2 . 33
3.5 Magnetic and vibronic properties of d^n $(n > 0)$ MXenes 34
3.5.1 Nonmagnetic d^n $(n > 0)$ MXenes 35
3.5.2 Carbide MXenes with magnetic order: V_2CO_2, V_2CF_2, and Mo_2CF_2 37
V_2CO_2 : magnetic property and dynamical stability . . . 38
V_2CF_2 : magnetic property and dynamical stability . . . 42

Mo_2CF_2 : magnetic property and dynamical stability . . 44
3.6 Chapter summary 46

4 Discovery of C_3 MXene electride family 47
4.1 Research backgroud 48
4.1.1 Previous predictions of ferroelectric Sc_2CO_2 48
4.1.2 Searching for the C_3–Sc_2CO_2 ground state structure within $\sqrt{3} \times \sqrt{3}$ commensurate unit 49
4.1.3 Polymorph of scandium carbides with various carbon guises 50
4.2 Computational details 51
4.3 Atomic structure of C_3–M_2CO_2 52
4.4 Energy profile of transformation path of hex- and AFE-Sc_2CO_2 → C_3-Sc_2CO_2 53
4.5 Electronic structure of C_3-M_2CO_2 electrides 54
4.6 Ionization mechanism of C_3-M_2CO_2 electrides 56
4.7 Vibrational properties of C_3-M_2CO_2 58
4.7.1 Harmonic phonon dispersion and dynamical stability 58
4.7.2 Phonon density of states and IR and Raman activities 59
4.7.3 Molecular vibrations of the isolated C_3 and embedded C_3 in C_3-Sc_2CO_2 60
4.7.4 Molecular dynamics of M_2CO_2 in 300K 61
4.8 C_3–Sc_2CO_2 as an anode material of litihum-ion battery 62
4.9 Chapter summary 63

5 Strain engineering of hole carriers in p-type haeckelite GaN 65
5.1 Research backgroud 66
5.2 Purpose of this work 67
5.3 Computational details 67
5.4 Primitive band structure of w-GaN and 4|8-GaN 68
5.5 Hole states induced by Mg and Be impurities in 4|8-GaN 69
5.6 Strain control of hole states for efficient p-type doping of 4|8-GaN 71
5.7 Photoluminescence from multiple polaronic hole states 72
5.8 Chapter summary 74

6 Concluding remarks 75

Bibliography 77

Chapter 1

Introduction

Two-dimensional (2D) materials are those with an atomic thickness of less than a few nanometers. Since the first exfoliation of graphene from graphite in 2004 [1], 2D materials have attracted lots of attention not only for the miniaturization of devices but also as playgrounds for seeking novel physical and chemical properties that are exotic and distinct from those of conventional 3D materials [2, 3]. In such 2D materials, electronic states and charge charge carriers are strongly confined in the vertical directions while delocalized and mobile along in-plane direction [4, 2]. The strong confinement character in 2D materials largely affects in their electric current, heat flow, and photon-matter interactions that, sometime, result in extraordinary electronic, optical and magnetic properties with strong excitonic effect and high quantum emission yield etc. [5].

Many different types of 2D materials have been synthesized so far for various atomic compositions of elements across of the periodic table [6, 7]. The 2D materials exhibit diverse electrical and vibrational properties, behaving as metals, semimetals, insulators, and direct band gap semiconductors with a wide range of band gaps from ultraviolet to infrared. The two-dimensional geometry of 2D materials is highly compatible with current thin film production techniques in the semiconductor industry, which allows micro-integrations of 2D materials on solid substrates. The device applications of 2D materials now cover memory, logic gates, amplifiers, oscillators, and switches [8, 9].

During the last two decades, 2D materials have significantly contributed to the discovery of new physics through their carefully prepared and typically controlled lab-scale environments. However, technology for efficient, handy, and large area fabrication of 2D materials is still in its infancy despite its high demand from the material industry. In this regard, this dissertation presents a series of 2D materials that are possibly suited to practical fabrication, i.e., including MXenes (2D transition metal carbides and nitrides) and atomically thin GaN, which are emerging as viable candidates for many practical applications with large-scale production feasibility compared to other 2D materials. In the following sections, 2D materials, including MXene and ultra-thin GaN, are introduced as the main topics of this dissertation.

1.1 Two-dimensional transition metal carbides and nitrides (MXene)

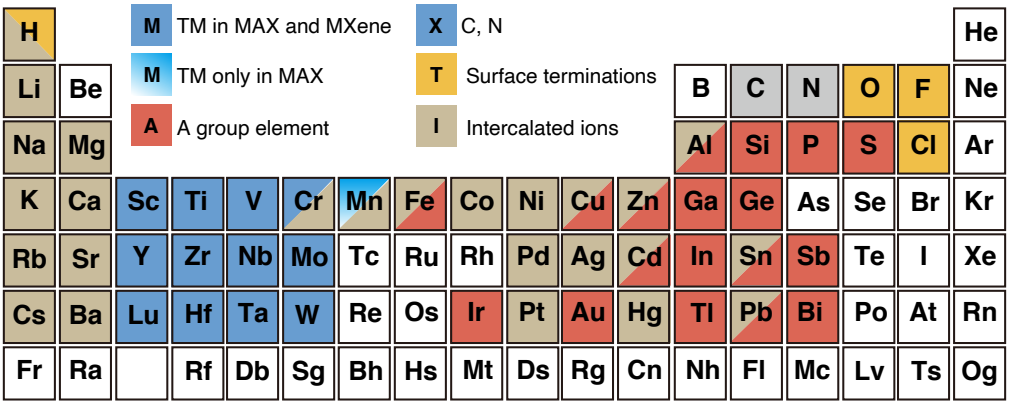

FIGURE 1.1: Periodic table of elements in MAX phases, MXenes, surface terminations, and itinerary cations. MXene surface terminations are yellow, whereas MAX phase A components are red. The yellow color shows the intercalated cations into MXenes. Solid solutions occur in TM atomic planes (blue) or A-element planes (red). This periodic table excludes elements discovered only by first principle calculations [10].

The investigation of transition metal carbides and nitrides for energy storage applications was initiated by the discovery in the 1970s. Since then, several nanostructure designs have been proposed, each small step increasing the surface area and performance of transition metal carbides and nitrides.

The fabarication of the first two-dimensional (2D) titanium carbide ($Ti_3C_2T_x$) in 2011 [11] paved the way for the discovery of a family of 2D transition metal carbides and nitrides, known as MXenes (pronounced "maxines") [12, 10]. MXenes are transition metal carbides and nitrides that are two-dimensional (2D) atomically thin sheets. The research field of MXenes is growing rapidly with expanding family of 2D materials for a wide range of applications.

MXenes are represented with the chemical formula $M_{n+1}X_nT_x$, where M is a transition metal (such as Sc or Y) and X is carbon or nitrogen; in the case of $M_{n+1}X_nT_x$, $n = 1 \sim 3$ [15, 16, 17]. The possible transition metal elements are in blue in Fig. 1.1 (periodic table). MXenes are usually terminated during the exfoliation process with hydroxyl (OH), oxygen (O) or fluorine (F), which often has significant effects on their electrical and magnetic characteristics. T denotes the surface termination groups, the majority of which are = O, OH, and F, and x in T_x denotes the number of surface functionalities. A representative figure related with chemical exfoliation of Ti_3C_2 MXenes is presented in Fig. 1.2.

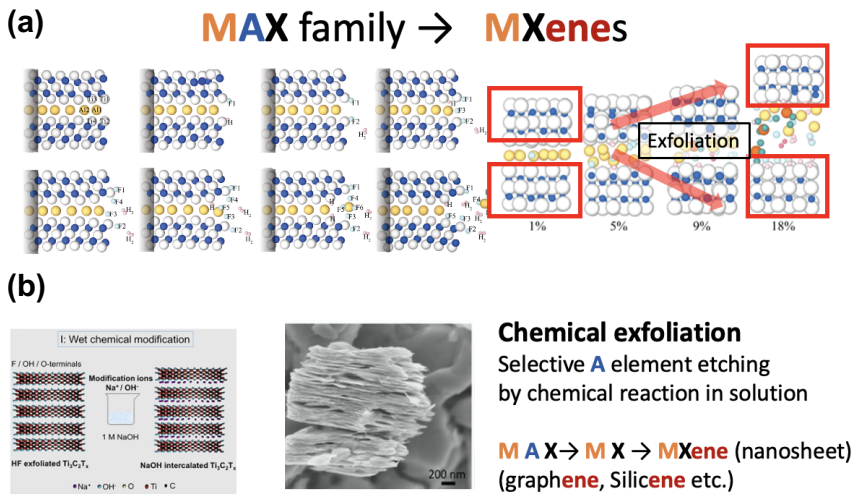

FIGURE 1.2: Chemical exfoliation process and optical image of experimentally synthesized Ti_3C_2 MXenes. (a) Chemical exfoliation process in hydrofluoric acid obtained with molecular dynamics simulation [13] (Reprinted with permission from [13]. Copyright 2016 American Chemical Society). (b) The SEM (Scanning Electron Microscope) image of exfoliated Ti_3C_2 MXenes (Reprinted from [14], with permission from Elsevier).

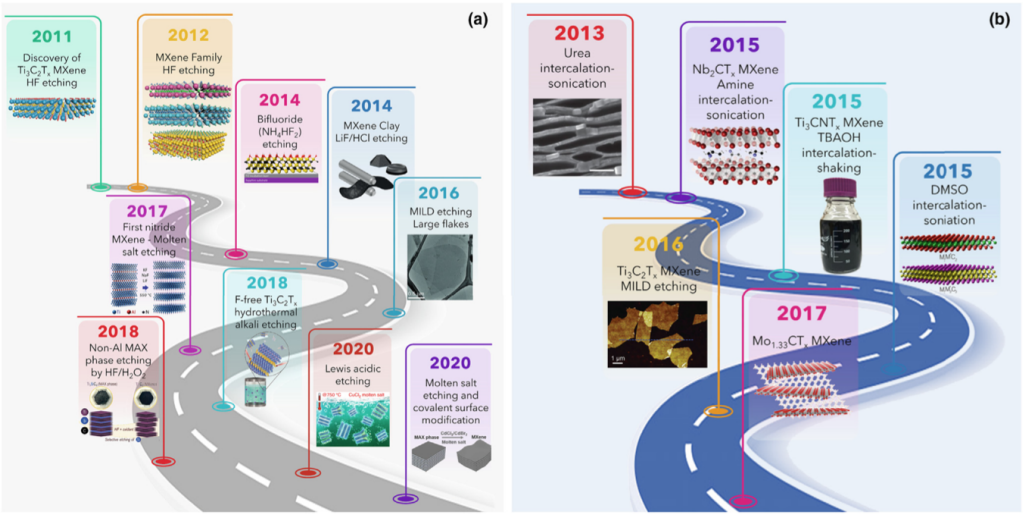

FIGURE 1.3: Milestones of etching MAX phases and delamination of multilayered MXenes. (Reprinted from [18], with permission from Elsevier)

The experimentally confirmed surface terminations are in yellow in Fig. 1.1. The anticipated atomic structures of MXenes with various positions of termination groups are shown in Fig. 1.3. The thickness of the two-dimensional sheets is adjustable in the range of 1 nm by changing the number of MXenes in the formula from M_2XT_x to $M_3X_2T_x$ and $M_4X_3T_x$, respectively.

From the discovery of MXenes in 2011 [11], MXenes are widely applied to catalysis, electrode technology, gas sensor technology, and electromagnetic screening [12, 19, 20, 21] (cf. Fig. 1.3). With the radical growth of interest

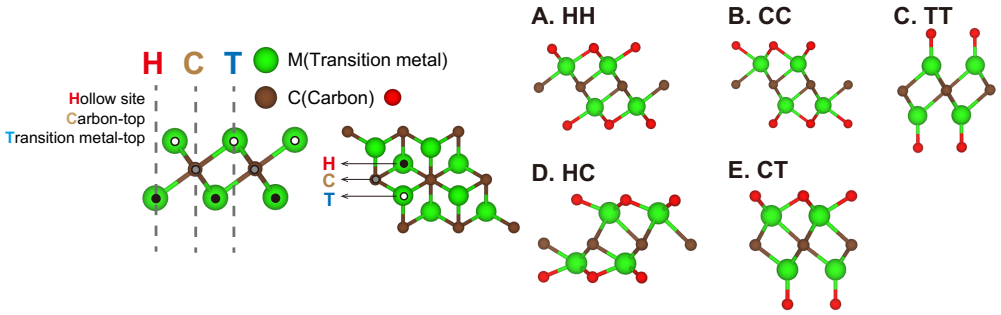

FIGURE 1.4: [From Fig. 1 of publication I] (reprinted with permission by Elsevier) Representative geometrical structures of the functionalized T_2C MXenes.

in MXene, large number of theoretical studies using first principles calculations based on density functional theory (DFT) have been extensively conducted [22, 23, 24]. However, many of the electronic and magnetic properties of MXenes still remain unclear. Theoretical limitations of approximate exchange-correlation functionals mostly caused by self-interaction error that often spuriously delocalizes $3d$ states of transition metal elements. The delocalization problem of $3d$ states should be resolved for correct analysis of electronic, magnetic, and vibrational properties of MXenes. On the other hand, underlying MXene studies limit their focus to a triangular carbon network while non-triangular C_3 structures of MXene phase were theoretically predicted by Bae *et al.* in publication II. In this dissertation, a series of MXene studies based on *ab initio* calculations are presented in chapter 3 and chapter 4.

1.2 Low-dimensional GaN and its application

During last two decades, a diverse range of 2D materials have been found and synthesized, such as black phosphorene, transition metal dichalcogenides, and MXenes. The majority of these two-dimensional materials are exfoliated from three-dimensional van der Waals materials, in which layered materials comprised of 2D sheets are stacked on top of each other and held together by weak van der Waals forces. While exfoliation and isolation of the 2D materials using mechanical, chemical, or electrochemical methods by breaking relatively week van der Waals linked layered compounds have been successfully achieved,the exfoliation technique of 2D materials from the conventional covalently connected three-dimensional crystals currently remains as a horrendous task; for example, exfoliation of 2D III-V materials have been hardly realized due to unsaturated dangling bonds on the cleaved surface delivered from the tetrahedral covalent coordination of wurtzite gallium nitride (w-GaN) and other III-V compounds.

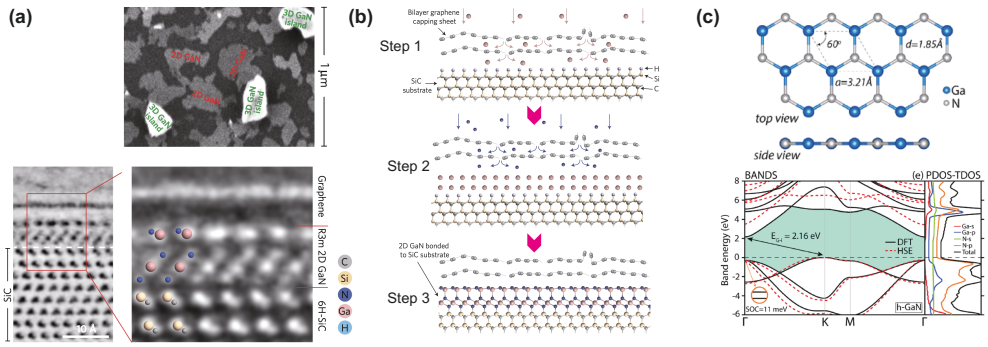

FIGURE 1.5: (a) SEM (Scanning Electron Microscopy) image of 2D GaN (patchwork regions of bright contrast) concentrated near 3D GaN islands (Reprinted from Ref. [25] by permission from Springer Nature Materials). (b) The MEEG process for the creation of 2D GaN is as follows: step 1, breakdown of the trimethylgallium precursor and surface diffusion of gallium adatoms; step 2, intercalation and lateral interface diffusion; and step 3, gallium transformation to 2D GaN by ammonolysis (Reprinted from Ref. [26] by permission from Springer Nature Materials). (c) Atomic structure of 2D h-GaN and its band structure obtained using density-functional theory (Reprinted from Ref. [27], with the permission of AIP Publishing)

As a remarkable breakthrough made in 2016, Al Balushi *et al.* achieved two-dimensional GaN by passivating surface dangling bonds through a migration-enhanced encapsulation growth (MEEG) approach [26, 25]. In the fabrication process, the atomically thin GaN is sandwiched between graphene layers for capping that significantly stabilizes the 2D-GaN layer. The graphene capping sheet is realized by selective extraction of Si from the SiC substrate and subsequent decomposition of trimethylgallium on the graphene/SiC surface, as described in Fig. 1.7 (b). The atomic and electronic structure of the hexagonal 2D GaN (h-GaN) was calculated by first principles calculation using density-functional

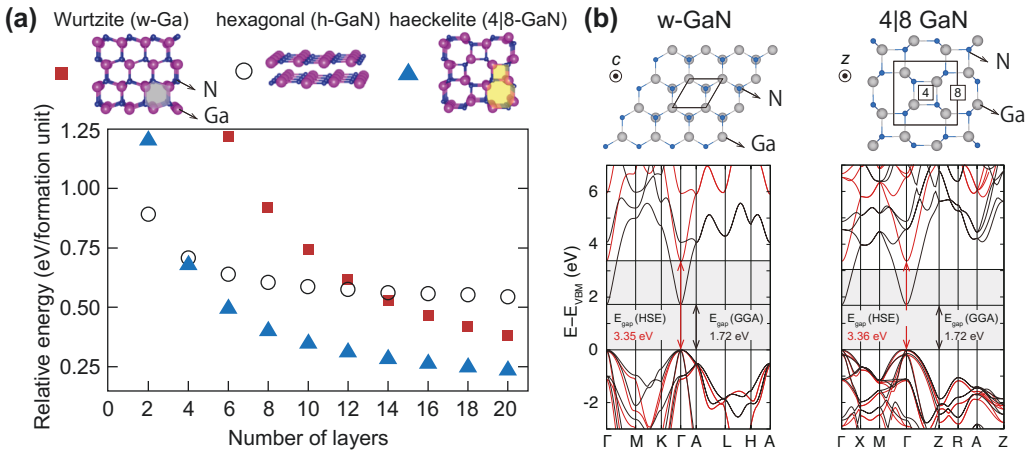

FIGURE 1.6: (a) Relative energies of hexagonal, wurtzite, and haeckelite GaN per formation unit i.e., two atoms of GaN (reprinted with permission from Ref. [28], APS). (b) Band structure of wurtzite and haeckelite GaN (w-GaN and 4|8 GaN). The total energies and electronic structures are obtained by density-functional theory with PBE-GGA exchange-correlation functional [29].

theory [27], as shown in Fig. 1.7 (c).

Inspired by the discovery of 2D-GaN, the polymorph of GaN, including various phases, was extensively explored for a various range of layer thicknesses [28, 30]. From first principles studies based on density-functional theory, From first principles studies based on density-functional theory, it has been revealed that non-polar haeckelite GaN (4|8-GaN) is the most stable ground state phase compared to the conventional wurtzite GaN (w-GaN) for a wide range of layer thickness between 2 and 47 GaN layers [28]. In contrast to w-GaN, 4|8-GaN has a non-polar surface in the normal direction that results in nearly zero internal electric field that stabilizes 4|8-GaN compared when the thickness of GaN is atomically thin [30]. Surprisingly, the optoelectronic properties of 4|8-GaN are similar to those of w-GaN, implying that 4|8-GaN could be used in atomically thin light-emitting diodes (LEDs). Moreover, 4|8-GaN is expected to be superior to w-GaN in in-plane hole mobility due to zero built-in electric field in the normal direction [30].

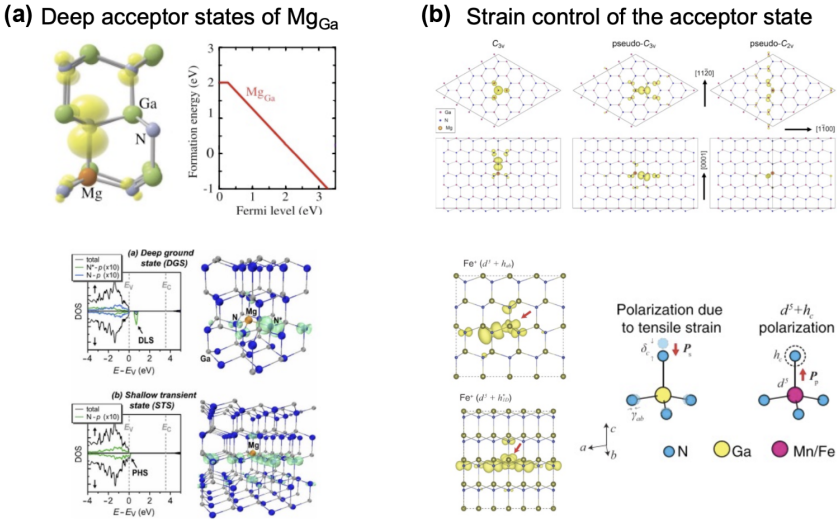

FIGURE 1.7: Previous studies of Mg acceptor and its polaronic hole state in wurtzite GaN. (a) The deep acceptor character of Mg acceptor (upper panel, reprinted with permission from Ref. [31], APS) and bistability of the acceptor state(lower panel, reprinted from Ref. [32], with the permission of AIP Publishing). (b) Strain control of the Mg acceptor state (upper panel, reprinted with permission from Ref. [33], APS) and the hole state bound to transition metal impurities (lower panel, reprinted with permission from Ref. [34], APS).

The hole dopability of p-type GaN is known to be typically low. This typically degrades the operating efficiency of conventional GaN-based LEDs [35, 36, 37]. While Mg is used as a primary p-type dopant in GaN, hole carriers are frequently trapped in localized acceptor states of Mg impurity, which act as deep acceptors [38, 32, 39, 40, 41]. However, the p-type dopability of 4|8-GaN remains unknown, which should be elucidated for the realization of atomically thin GaN-based LED devices for future technologies. In this dissertation, an *ab initio* study of p-type doping of 4|8-GaN (haeckelite GaN) and its strain control is presented in Chapter 5.

1.3 Chapter overview

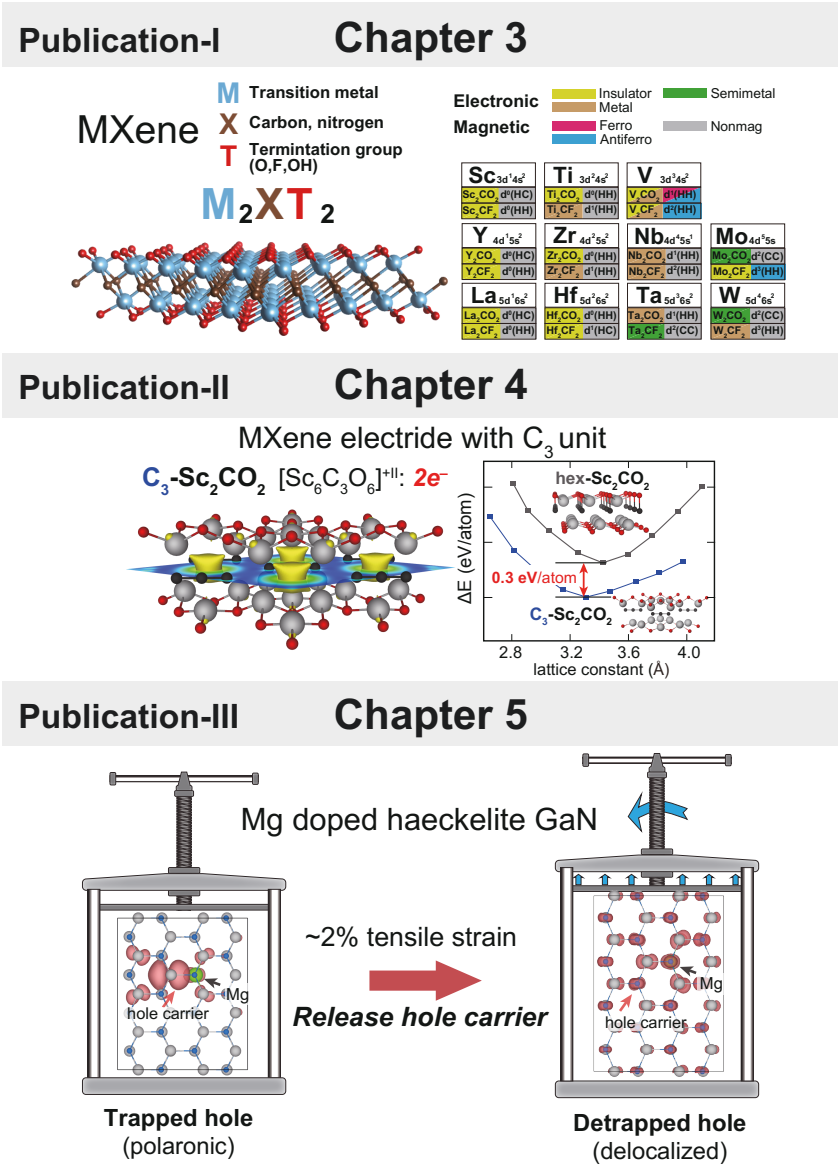

FIGURE 1.8: Concept illustration the topics of chapter 3, chapter 4, and chapter 5 partially adapted from graphical abstracts of Publication I (upper panel), Publication II (middle panel), and Publication III (lower panel).

This dissertation provides first principles studies of two-dimensional (2D) materials, including 2D transition metal carbides and nitrides (MXenes) and atomically thin haeckelite GaN based on Publications I, II, and III.

This dissertation consists of the following chapters:

- In Chapter 2, the theoretical framework of first principles calculation based on density-functional theory and related methods are described.

- Chapter 3 overviews publication I. A comprehensive first-principles study of carbide MXenes explored with various theoretical approaches are presented.

- Chapter 4 provides detailed descriptions of publication II. The new theoretical discovery of a family of 2D MXene elctrides with C_3 trimer unit and their mechanical, vibronic, and electronic properties are discussed.

- Chapter 5 summarizes publication III. The p-type doping of atomically thin haeckelite GaN intimately related to strong polaronic character of the bound hole state and its strain control are outlined.

- Finally, a concluding remark of this dissertation is provided in Chapter 6.

Chapter 2

Theoretical framework

2.1 Density-functional theory

The *ab initio* calculations presented throughout of this dissertation employ density-functional theory (DFT) for obtaining electronic and atomic structures that give electrical, optical, and mechanical properties of various materials. Density-functional theory (DFT) is a theoretical framework that enables calculations of quantum mechanical properties for a wide variety of atomic system, ranging in size from tens to thousands of atoms, by efficiently balancing its computational cost and accuracy.

By adopting Born-Oppenheimer approximation to many body systems consisting of electrons and nuclei, the time-independent electronic Schröedinger equation reads

$$\hat{H}\Psi = [\hat{T} + \hat{V}_{ext} + \hat{V}_{int} + E_{II}]\Psi = E\Psi, \tag{2.1}$$

where $\hat{V}_{ext}$ is the attractive potential energy from the nuclei, $\hat{T}$ is the kinetic energy operator,$\hat{V}_{int}$ represents the electron-electron repulsive interactions, E_{II} is the classical coulomb repulsion between nuclei, and E is the total energy [42]. Although the many body Schröedinger equation is straightforward to construct, it is not suitable to solve more than two particles. For this complexity, Density-functional theory present a practical way to convert the many body problem more tractable.

The formalism of density-functional theory (DFT) is based on the fundamental theorem referred to as the Hohenberg-Kohn theorem [43]. For arbitrary many-body systems, the ground state with electron density $n(\mathbf{r})$) under an aribtral external potential $\hat{V}_{ext}(\mathbf{r})$ is expressed as a functional of the electron density shown as

$$E[n(\mathbf{r})] = \int d\mathbf{r}\hat{V}_{ext}(\mathbf{r})n(\mathbf{r}) + F[n(\mathbf{r})] + E_{II}. \tag{2.2}$$

Here, $F[n(\mathbf{r})]$ is a universal density functional that includes the following terms

$$F[n(\mathbf{r})] = E_{\text{ee}}[n(\mathbf{r})] + T[n(\mathbf{r})]. \tag{2.3}$$

Here $E_{\text{ee}}[n(\mathbf{r})]$ is the electron-electron interaction energy and $T[n(\mathbf{r})]$ is the kinetic energy of electrons.

The electron-electron interaction energy $E_{\text{ee}}[n(\mathbf{r})]$ can be further divided into

$$E_{\text{ee}}[n(\mathbf{r})] = \frac{1}{2}\int\int \frac{n(\mathbf{r}_i)n(\mathbf{r}_j)}{r_{ij}} d\mathbf{r}_i\mathbf{r}_j + E_{\text{xc}}[n(\mathbf{r})], \tag{2.4}$$

where the first term is the electron-electron coulomb repulsion and the second term $E_{\text{xc}}[n(\mathbf{r})]$ is the exchange-correlation functional which includes the quantum contribution to the electron-electron interaction.

The Hohenberg-Kohn theorem shows that the ground state total energy of an interacting system consisting of electrons and nuclei is determined by the ground state electron density. In other words, the electron density of the ground state is the electron density that minimizes the total energy. To solve for the ground state electron density variationally, we simply need to know the energy functional $E[n(\mathbf{r})]$. While a wavefunction may include up to 3N variables, a charge density has three spatial variables. Density-functional theory has much decreased degree of freedom, which makes the theory a potentially more powerful approach compared to more costly wavefunction-based approaches unless more accurate.

Beside the Hohenberg-Kohn theorem that connects the ground state total energy to the electron density instead of the electronic wave function that critically reduces computational cost, there are obstacles to practical electronic structure calculations that need to be resolved. First, the exact form of the exchange-correlation functional $E_{\text{xc}}[n(\mathbf{r})]$ remains unknown. Second, the exact form of the kinetic energy functional $T[n(\mathbf{r})]$ for arbitrary electron densities is also unknown. The first attempt to approximate $T[n(\mathbf{r})]$ was to adopt the Thomas-Fermi model of the uniform electron gas [44] although its accuracy was insufficient to practically describe quantum systems.

In 1965, Kohn and Sham derived an equation of motion of non-interacting electrons obtained by the density mapping from the interacting system, which is the cornerstone of modern DFT calculations [45]. The Kohn-Sham framework gives the equation of motion of non-interacting electrons in a mean-field effective potential. Specifically, the Kohn-Sham technique rewrites the Hohenberg-Kohn statement for the ground state functional as follows

$$E_{\text{KS}} = T_{\text{s}}[n] + \int d\mathbf{r}\hat{V}_{\text{ext}}(\mathbf{r})n(\mathbf{r}) + E_{\text{hartree}}[n] + E_{II} + E_{\text{xc}}[n]. \tag{2.5}$$

Here $T_{\text{s}}[n]$ is the kinetic energy of non-interacting electron system, $E_{\text{hartree}}[n]$ is the mean-field Coulomb interaction energy of the electron density, and $E_{\text{xc}}[n]$ is the exchange-correlation functional. The first three terms of this equation are well-known and may be evaluated directly. The $E_{\text{xc}}[n]$ term indicates the differences between the kinetic energies and potential of an interacting versus a non-interacting system, as shown by the following formulation [45],

$$E_{\text{xc}}[n] = \hat{T} - T_{\text{s}}[n] + \hat{V}_{int} - E_{\text{hartree}}[n], \tag{2.6}$$

and is unknown.

By using the variational principle for the total energy functional for non-interacting Kohn-Sham orbitals, the Kohn-Sham equation is derived:

$$\left(-\frac{\hbar^2}{2m}\nabla^2 + v_{\text{eff}}(\mathbf{r})\right)\phi_i(\mathbf{r}) = \epsilon_i\phi_i(\mathbf{r}), \tag{2.7}$$

where $-\frac{\hbar^2}{2m}\nabla^2$ is the kinetic energy operator, v_{eff} is the effective potential affecting non-interacting electrons, ϵ_i is the Kohn-Sham eigenvalue, and $\phi_i(\mathbf{r})$ is the Kohn-Sham electron orbital.

The effective potential $v_{\text{eff}}(\mathbf{r})$ consists of

$$v_{\text{eff}}(\mathbf{r}) = v_{\text{ext}}(\mathbf{r}) + e^2\int\frac{n(\mathbf{r}')}{|\mathbf{r}-r'|}dr' + \frac{\delta E_{\text{XC}}[n(\mathbf{r})]}{\delta n(\mathbf{r})}, \tag{2.8}$$

where v_{ext} is the external potential and the last term

$$v_{\text{xc}} = \frac{\delta E_{\text{xc}}[n]}{\delta n(\mathbf{r})} \tag{2.9}$$

is the exchange-correlation potential.

2.2 Approximations of exchange-correlation functionals

For practical calculations of DFT various approximations of E_{xc} (exchange-correlation functional) have been proposed. Among the large number of approximate exchange-correlation functionals, some representative density functionals are introduced in the next section. In the DFT calculations presented in dissertation, GGA (GGA: generalized gradient approximation) and its $+U$ correction were adopted, and HSE06 hybrid functional has been employed for the verification of quantitative results of GGA and GGA$+U$ functionals.

2.2.1 Local density approximation (LDA)

In the local density approximation (LDA), the exact exchange and correlation energy of a homogeneous electron gas are applied as calculated using Hartree-Fock approximation and quantum Monte Carlo calculations [46, 47].

The E_{xc} of the LDA approximation is directly determined from the local charge density,

$$E_{\text{xc}}^{LDA}[n] = \int d\mathbf{r} n(\mathbf{r}) \epsilon_{XC}^{homogen.}[n(\mathbf{r})]. \tag{2.10}$$

The exchange energy per unit electron is

$$\epsilon_X^{homogen.} = -\frac{3}{4\pi}(3\pi^2 n)^{1/3} = -\frac{0.458}{r_s}, \tag{2.11}$$

where $r_s = (3/4\pi n)^{1/3}$ represents an average distance between electrons.

For the electron correlation energy of the homogeneous electron gas, the only high-density limit ($r_s 0$) and low-density limit r_s inf) are analytically known [47]. Several parameterizations have been proposed to interpolate the high-density and low-density limit, for instance in the Perdew-Zunger parameterization [48],

$$\epsilon_C^{\text{PZ}}[r_s] = \begin{cases} 0.0311 \ln r_s - 0.048 + 0.002 r_s \ln r_s - 0.0116 r_s & \text{for } r_s \leq 1 \\ (-0.1423)/(1 + 1.0529\sqrt{r_s} + 0.3334 r_s) & \text{for } r_s > 1. \end{cases} \tag{2.12}$$

Despite its simplicity, LDA has been applied to a wide variety of material systems predicting considerably accurate structural parameters and valance electronic states.

2.2.2 Generalized gradient approximation (GGA)

The generalized gradient approximation (GGA) is a extension of LDA that contains the dependence of the gradient of the charge density expressed as,

$$E_{\mathrm{xc}}^{GGA}[n] = \int d\mathbf{r} n(\mathbf{r}) \epsilon_{\mathrm{xc}}^{GGA}(n(\mathbf{r}), \nabla n(\mathbf{r})). \tag{2.13}$$

While the concept of the generalized expansion was proposed in the original paper of Hohenberg and Kohn [43], a successful development of gradient approximation of the exchange-correlation functional was made two decades after. The reason of the slow emergence of the successful gradient approximation was originated from the fundamental physical properties of the exchange-correlation functional where several fundamental conditions should be fulfilled [49]. In 1996, Perdew, Burke, and Ernzerhof (PBE) proposed the PBE-GGA functional that fulfills three essential fundamental physical conditions [29].

The following is a brief note of the PBE-GGA functional as presented in Ref. [29]. First, the exchange energy is expressed as

$$E_x[n(\mathbf{r})] = \int d\mathbf{r} \epsilon_{\mathrm{x}}^{PBE} F_x(s), \tag{2.14}$$

where $s = |\nabla n|/[2(3\pi^2)^{1/3} n^{4/3}]$ is a density gradient.

The following conditions should be satisfied upon constructing the exchange energy functional

1. Electron gas limit being uniform: $F_x(0) = 1$
2. Linear response to local spin density approximation (LSDA): as $F_x \to 1 + \mu s^2$, $\mu = 0.22$ as $s \to \infty$
3. Lieb-Oxford lower bound condition: For $F_x(s) \leq 1.804$, the function $F_x(s)$ that satisfies the conditions above is extracted to be

$$F_x(s) = 1 + \kappa - \frac{\kappa}{1 + \mu s^2/\kappa} \tag{2.15}$$

with $\kappa = 0.804$. In the same manner, the correlation energy is expressed as

$$E_c[n(\mathbf{r})] = \int d\mathbf{r} [\epsilon_{\mathrm{c}}^{PBE}(r_s, \xi) + H(r_s, \xi, t)], \tag{2.16}$$

where $t = |\nabla n|/(2\phi k_s n)$ is a density gradient, k_s is the screening wave vector (Thomas Fermi), and $\phi(\xi) = [(1+\xi)^{2/3} + (1-\xi)^{2/3}]/2$ is a scaling factor. The $H(r_s, \xi, t)$ has the form

$$H(r_s, \xi, t) = \gamma \phi^3 ln[1 + \frac{\beta}{\gamma} t^2 \frac{1 + At^2}{1 + At^2 + A^2 t^4}], \tag{2.17}$$

where

$$A = \frac{\beta}{\gamma exp(-\epsilon_c/\gamma\phi^3) - 1]^{-1}}. \tag{2.18}$$

The coefficients $\gamma = 0.03109$ and $\beta = 0.066725$

The $H(r_s, \xi, t)$ is constructed for satisfying the following conditions.

1. At slow-varying density i.e., $t \to 0$, $H \to \beta\phi^3 t^2$.
2. At rapid-varying density i.e., $t \to \infty$, H asymptotically approaches $H \to -\epsilon_c$ that impose the zero correlation energy at the rapid-varying density limit.
3. H should eliminate the logarithmic singularity in ϵ_c at the high-density limit ($r_s \to 0$) by fulfilling $\epsilon_c(r_s, \xi) \to (e^2/a_0)\phi^3[\gamma ln(r_s/a_0) - \omega]$, where $\omega \approx 0.046644$, $\gamma \approx 0.031091$, and a_0 is the bohr length.

While GGAs outperform LDA for many systems, LDA and GGA are still considerably inaccurate for describing several material properties e.g., van der Waals dispersion interaction, localized polaronic states and optical properties such as band gap. The theoretical limitations of LDA and GGA are caused by several origins. First of all, approximations of exchange potential LDA and GGA exhibit much more decay compared to the exact exchange that is proportional to $1/r$ where r is the distance [50]. This causes imperfect cancellation of self-interaction in the electron Coulomb energy remaining as a *self-interaction error* (SIE) that tends to spuriously delocalize the electronic states. Second, the band gaps of insulators predicted by LDA and GGA are grossly underestimated by approximately by 50%, which is not only caused by SIE of approximate functionals but also originated from the theoretical limitation of the Kohn-Sham theory [45] due to a lack of *functional discontinuity* that should be included in the fundamental band gap [51].

2.2.3 Meta-generalized gradient approximation (MGGA)

The exchange-correlation energy in meta-generalized approximation (MGGA) is expressed as

$$E_{xc}^{\mathrm{MGGA}} = \int d\mathbf{r} e_{xc}(n, \nabla n, \tau) \tag{2.19}$$

where $\tau = 1/2 \sum_i^{\mathrm{occupied}} |\nabla \phi_i|^2$ is the kinetic energy density of Kohn-Sham orbitals. Introducing τ makes MGGA recover the fourth-order gradient expansion in the slowly-varying density limit [50]. The SCAN (strongly constrained and appropriately normed) functional is a type of MGGA functional that satisfies 17 known exact constraints that a meta-GGA can fulfill [52]. Details of fundamental conditions related to SCAN functional can be found in Ref. [52].

SCAN functional outperforms conventional LDA and GGA functionals for e.g., metal surfaces [53], formation energies, liquid silicon [54] and liquid water [55]. SCAN predicts correct phase stability of several 2D materials [56]. Remarkably, several successes of SCAN functional for strongly correlated systems have been addressed; 1) SCAN predicts correct relative phase stability of the MnO_2 while Hubbard-U correction on PBE-GGA functional fails to predict the ground-state structure [57]; 2) SCAN presents correct descriptions of the structural, electronic, and magnetic properties of the La_2CuO_4 and $La_{2-x}Sr_xCuO_4$ and their phase stabilities [58, 59, 60].

Despite many successes of SCAN functional, failures of SCAN functional were also reported. For several transition metal compounds, SCAN fails to predict correct formation enthalpies and this pitfalls were corrected by the SCAN+U approach [61, 62]. Especially SCAN predicts false relative phase stability of CuO and Cu_2O i.e., excessively stabilizing Cu_2^+ (d^9) over Cu_1^+ (d^{10}) such that Cu_2O cannot be thermochemically stable in SCAN prediction [63]. The performance of SCAN for transition metal carbides (MXenes) compared to PBE-GGA functional and other exchange correlation functionals is discussed in chapter 3.

2.2.4 Hybrid functional

One successful improvement of the LDA and GGA approximations is the hybrid functional that contains a fraction of exact Hartree-Fock exchange that is not present in LDA and GGA functionals. Perdew, Ernzerhof, and Burke proposed the PBE0 functional with the following form:

$$E_{\mathrm{xc}}^{\mathrm{PBE0}} = E_{\mathrm{xc}}^{\mathrm{PBE-GGA}} + a_0(E_x^{\mathrm{exact}} - E_{\mathrm{x}}^{\mathrm{PBE-GGA}}), \tag{2.20}$$

where E_{xc} is the exchange-correlation energy, E_{x} is the exchange energy and a_0 is the mixing parameter that is set to 0.25 for the PBE0 functional [29].

While PBE0 functional remarkably cures the band gap underestimations of LDA and GGA functionals and delocalization problems of surface states and polaronic states, the PBE0 functional has been found to overcorrect *self-interaction errors* that spuriously prefer localized states compared to delocalized states.

The HSE functional proposed by Heyd, Scuseria, and Ernzerhof (HSE) comprises both localized and delocalized states by including a fraction of exact exchange for short range interactions and GGA exchange for longer range interactions. The HSE hybrid functional is written as

$$E_{\mathrm{xc}}^{\mathrm{HSE}} = aE_{\mathrm{x}}^{\mathrm{HF,SR}}(\omega) + (1-a)E_{\mathrm{x}}^{\mathrm{PBE,SR}}(\omega) + E_{\mathrm{x}}^{\mathrm{PBE,LR}} + E_{\mathrm{c}}^{\mathrm{PBE}}, \tag{2.21}$$

where a is 0.25 and ω, the range separation parameter ω is 0.2 [64] and the exact exchange potential are separated into SR (short range) and LR (long range) parts. Due to the optimized mixing of the exact exchange, HSE tends to predict better band gaps and electronic localizations than LDA and GGA functionals. However, the calculation of exact exchange energy requires 50∼100 times larger computational costs than that of LDA and GGA calculations, which are a main bottleneck for practical DFT calculations of large solid systems with a few hundred atoms. In the next section, an alternative correction of LDA and GGA functionals is introduced that corrects self-interaction correction by applying on-site potential to localized orbitals.

2.3 DFT+U formalism

In the previous section, several approximations of the exchange-correlation functional E_{xc} have been introduced. In a wide consensus currently made in the field of DFT calculation, PBE-GGA functional and its derivatives work properly for a wide range of materials but they typically fail to describe localized electronic states that are mostly originate from $3d$ electrons in transition metal elements and $2p$ electrons in oxygen and nitrogen atoms. It is obvious that the traditional approximations obtained from the characteristics of the free electron gas are insufficient to characterize the electron correlation in these highly correlated electronic systems with tightly laid energy bands. To rectify the PBE-GGA functional's erroneous behavior, it is compelling that localized $3d$ and $2p$ states might be selectively remedied by applying an on-site potential exertion to the specified localized states.

The DFT+U technique is based on a mixture of the DFT approach and the Hubbard model, [65], which incorporates on-site repulsion between electrons through the Hubbard type energy defined by the U and J parameters. The method has been applied to challenging cases of DFT calculations, including d and f electrons [66]. The energy functional of DFT+U scheme is represented as

$$E_{\text{DFT}+U}[\rho, n^{\sigma}] = E_{\text{DFT}} + E_U[n^{\sigma}] = E_{DFT}[\rho] + E_{\text{Hubbard}}[n^{\sigma}] - E_{\text{dc}}[n^{\sigma}], \quad (2.22)$$

where n is the occupation matrix of d orbital, σ represents the spin, and E_{DFT} is the original DFT energy functional. The E_U can be divided into two terms; E_{Hubbard} is the Hubbard Hamiltonian [67]; (E_{dc}) is a the double-counting term to describes the part of the electron correlations that is already accounted for by DFT [67]. The rotationally invariant energy functional i.e., E_{Hubbard} and E_{dc} term were derived by Liechtenstein et al. [68]. The derivation reads

$$\begin{aligned} E_{\text{Hubbard}} = \frac{1}{2}\sum_{m,\sigma}(\langle m, m''|V_{ee}|m', m''\rangle n^{\sigma}_{mm'} n^{-\sigma}_{m''m'''} + \\ (\langle m, m''|V_{ee}|m', m''\rangle - \langle m, m''|V_{ee}|m''', m'\rangle) n^{\sigma}_{mm'} n^{-\sigma}_{m''m'''} \end{aligned} \quad (2.23)$$

$$E_{\text{dc}} = \frac{1}{2}Un(n-1) - \frac{1}{2}J[n^{\uparrow}(n^{\uparrow}-1) + n^{\downarrow}(n^{\downarrow}-1)]. \quad (2.24)$$

More simplified form of the DFT+U correction term was introduced by Dudarev et al. [69]. In this approach, F^2,F^4 and F^6 (the higher order integrals) are assumed to be 0. The energy functional E_U can be simplified as

$$E_U = E_{\text{Hubbard}} - E_{\text{dc}} = \sum_{l,\sigma} \frac{U_{\text{eff}}}{2} \text{Tr}[\mathbf{n}^{l,\sigma}(1 - \mathbf{n}^{l,\sigma})] \quad (2.25)$$

. The $U_{\text{eff}} = U - J$ is referred as an effective U parameter [69]. Throughout

of this dissertation, the simplified Dudarev $+U$ approach has been employed in DFT calculations

2.4 Plane waves and pseudopotentials

For handling the Kohn-Sham equation with numerical calucaltions, a basis set is required to represent wavefunctions with the coefficients filled in a matrix form that is diagonalized. In the DFT calculations presented in the dissertation, the plane-wave base set was employed in periodic boundary conditions. The wave function is expanded with plane waves:

$$\Psi_{n\mathbf{k}}(\mathbf{r}) = \frac{1}{\Omega^{1/2}} \sum_{\mathbf{G}} C_{\mathbf{G}n\mathbf{k}} e^{i(\mathbf{G}+\mathbf{k})\cdot\mathbf{r}}, \tag{2.26}$$

where Ω is the volume of the simulation cell, $\mathbf{G}$ is a reciprocal lattice vector, and $\mathbf{k}$ is a momentum vector of the reciprocal space. The number of plane-wave basis depends on the lattice vectors and the energy cutoff energy E_{cutoff}. For a given cut-off energy, plane waves following equation span the Kohn-Sham wavefunction

$$\frac{\hbar^2}{2m_e}|\mathbf{G}+\mathbf{k}|^2 < E_{cutoff}. \tag{2.27}$$

2.5 The projector augmented-wave (PAW) method

For many systems, treating all electrons in DFT calculations is computationally prohibitively costly due to rapid oscillational behavior of core electron wavefunction due to the orthogonality of electronic states in the core region. The wave function behaves differently in various areas of space (i.e. core and interatomic region), therefore plane wave base set is not suited to express core electrons that are highly localized and oscillatory. To tackle such problems, the projector augmented-wave (PAW) approach has been introduced. The wave function oscillates rapidly around atomic nuclei (augmentation region Ω_R), thus it is easy to expand the wave function as partial waves (spherical harmonics); yet, the wave function behaves relatively smoothly in the zone between atoms outside the nucleus (interstitial region), and it is convenient to extend the wave function as envelope functions (e.g. plane waves). Blöchl [70] divides the electron wave function as follows:

$$|\Psi\rangle = \begin{cases} |\Psi^{\mathrm{PW}}\rangle = \sum_{\mathbf{G}} C_{\mathbf{G}} |e^{i\mathbf{G}\cdot\mathbf{r}}\rangle & \text{outside of } \Omega_R \\ \Sigma_i a_i |\phi_i\rangle & \text{inside of } \Omega_R, \end{cases} \tag{2.28}$$

where $|\Psi^{\mathrm{PW}}\rangle$ is the plane wave part and $|\phi_i\rangle$ are atomic partial wave part. As usual, the wave function needs to be continuous and differentiable at the edge of augmentation sphere.

The projector-augmented wave (PAW) method was introduced by Blöchl [70]. The electron wave function is transformed into auxiliary functions (here I denote with the tilde '~') $|\Psi\rangle = T|\tilde{\Psi}\rangle$, so the entire system can be efficiently spanned

with plane wave basis. The transformation in PAW method has the form

$$T = 1 + \sum_R T_R, \tag{2.29}$$

where T_R is a local operator. For each partial wave $|phi_i\rangle$ a corresponding auxiliary function $|\tilde{\phi}\rangle$ is chosen such that

$$|\Psi\rangle = \begin{cases} T_R|\tilde{\phi}_i\rangle = |\phi_i\rangle - |\tilde{\phi}_i\rangle & \\ |\psi^{\mathrm{PW}}\rangle = \sum_i a_i|\tilde{\phi}_i\rangle & \text{inside of } \Omega_R, \\ |\tilde{\phi}_i\rangle = |\phi_i\rangle & \text{outside of } \Omega_R. \end{cases} \tag{2.30}$$

The total wave function can be represented as

$$|\Psi\rangle = |\psi^{\mathrm{PW}}\rangle + \sum_i (|\phi_i\rangle - |\tilde{\phi}_i\rangle), \tag{2.31}$$

where the total wave function is expressed only in terms of the projector functions, the plane wave basis, and the physical and auxiliary partial waves.

2.6 Computational details of self-consistent DFT calculations

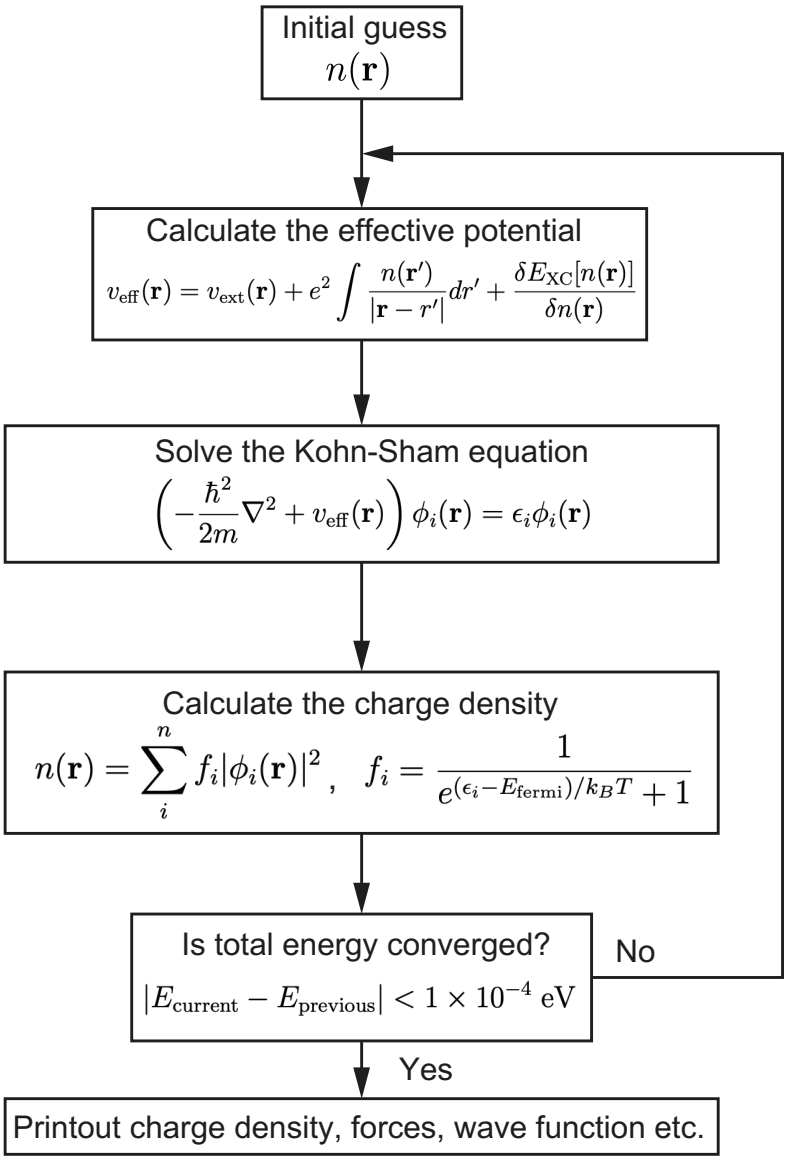

FIGURE 2.1: The self-consistent loop of DFT calculation solving the Kohn-Sham equation. The self-consistent convergence criteria has been imposed on the total energy difference between the previous and current step i.e., $\Delta E < 1 \times 10^{-4}$ eV.

In this dissertation, first-principles calculations based on density-funcitonal theory (DFT) have been performed for transition metal carbides and nitrides (MXenes) and gallium nitride (GaN) in haeckelite phase. For overall calculations, the PBE-GGA exchange-correlation functional (the generalized gradient approximation of the exchange-correlation functional proposed by Perdew, Burke, and Ernzerhof [29]) has been employed. The electronic structures are obtained from self-consistent calculation for solving the Kohn-Sham equation. A schematic of the self-consistent loop of DFT calculation is shown in Fig. 2.1. The self-consistent DFT calculations have been carried out with the VASP package [71, 72, 73, 74] using plane wave base sets and the projector augmented-wave (PAW) method [70].

For treating localized features of $3d$ electrons of transition metals in MXenes, GGA+U scheme with the form of Dudarev using adequate U_{eff} parameters was adopted [69]. The SCAN meta-GGA functional [33] was adopted for DFT calculations of MXenes. For simulating vibrational properties of MXenes, the Phonopy package [75] and Dynaphopy package [76] were used. Additional computational details such as cut-off energy and $\boldsymbol{k}$-point sampling are presented in each chapter.

Chapter 3

Ab initio prediction of electronic and magnetic properties of carbide MXenes

This chapter provides an overview of **Publication-1:** Electronic and magnetic properties of carbide MXenes—the role of electron correlations, **Soungmin Bae** *et al.*, Materials Today Advances **9** (2021): 100118.

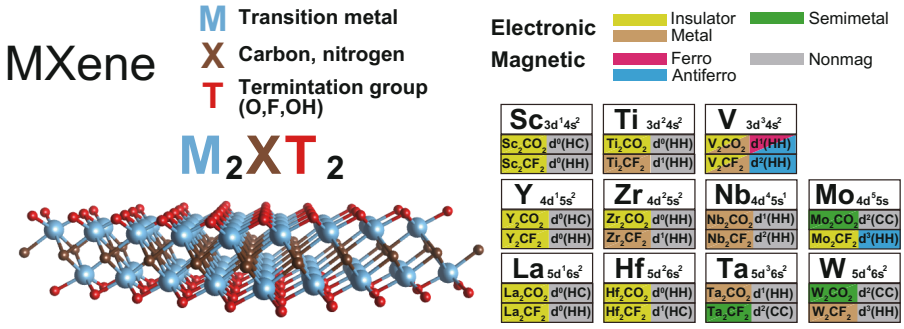

In this chapter, 22 carbide MXenes (M_2CT_2 with M= Sc, Y, La, Ti, Zr, Hf, V, Nb, Ta, Mo, W and T= O, F) have been explored using density-funcitonal theory with different exchange-correlation functionals, i.e., PBE-GGA, GGA+U, SCAN, and HSE06 functionals, which include different degrees of electron correlation and self-interaction correction. From the results, three magnetic MXenes V_2CO_2, V_2CF_2 and Mo_2CF_2 and one topological insulator Ta_2CF_2 have been found, which have not been predicted by DFT calculations of PBE-GGA functional due to its self-interaction error. The comprehensive description of vibronic properties of carbide MXenes has been outlined.

3.1 Research backgroud

Since the first discovery of Ti_3C_2 MXenes in the last decade, a large number of DFT (density functional theory) calculations have been performed to reveal the electronic and magnetic structures of MXenes [77, 78, 79, 80, 81, 82, 22, 23, 83, 24, 84, 85, 86]. In previous studies, the PBE-GGA functional (a semi-local generalized gradient approximation developed by Perdew, Burke and Ernzerhof) [29] was dominantly used despite its well-known erroneous description of $3d$ states due to its self-interaction error [87, 88, 89, 34, 90, 91, 92]. While erroneous behavior of PBE-GGA functional is usually corrected by several self-interaction correction methods, such as the PBE+U correction or meta-GGA, PBE+U (PBE functional with the Hubbard-U potential) has been recently applied to several MXenes and the specific choices of U parameters are still poorly clarified. Because many DFT predictions using PBE and PBE+U (with a wide range of parameters) coexist in the MXene field, many questions remain unanswered, particularly about the magnetic properties of MXenes [93, 94, 95].

In this work, a wide range of carbide MXenes were systematically explored using density functional theory with various approximate exchange-correlation functionals. The work establishes a determinative description of electronic and vibronic properties of MXenes through presenting comprehensive and comparative predictions that reflect the effects of different functionals and different Hubbard $+U$ corrections.

3.2 Computational details

For 22 carbide MXenes, the kinetic cutoff energy was set to 520 eV, Γ-centered $12 \times 12 \times 1$ and $21 \times 21 \times 1$ **k**-points grids are adopted for structure optimization and density of state calculations, respectively. The interlayer spacing of slab models was fixed as 15 Å. The structures are optimized using each of PBE, PBE+U, HSE06, and SCAN functional. The force exerted on atoms are minimized less than 10^{-5} eV/Å after the structure relaxation. The vibronic properties including phonon dispersion are calculated with Phonopy package [97]. Force constants required for the phonon calculations are calculated by the finite displacements added in $4 \times 4 \times 1$ supercells.

3.3 Structural and electronic properties of M_2CO_2 MXenes

3.3.1 Atomic configurations of M_2CT_2 MXenes

Five atomic structures of M_2CT_2 with different positions of termination groups are considered in the present work, as presented in Fig. 3.1 (a). In experiments, surfaces of MXenes are terminated with a mixture of O, F, or OH functional groups depending on the type of utilized acid during the exfoliation

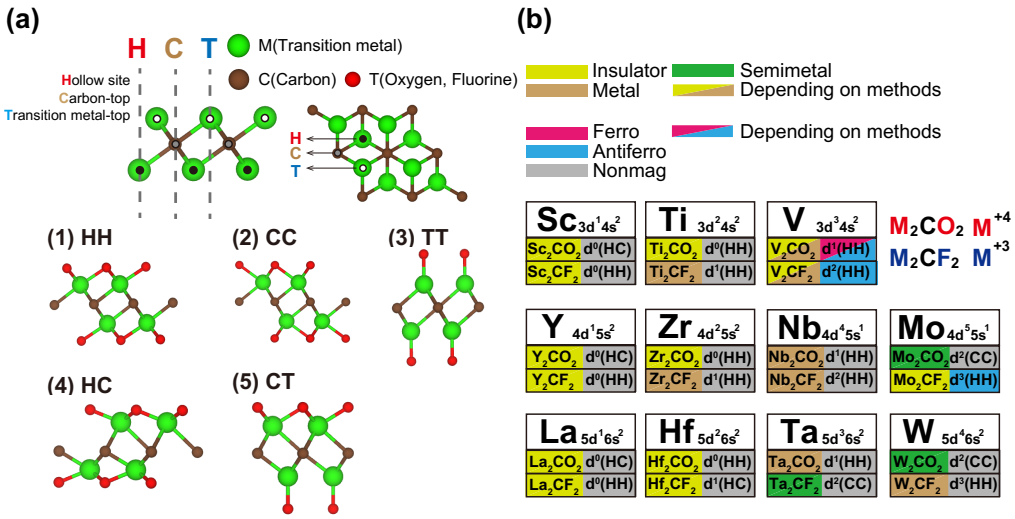

FIGURE 3.1: [From Fig. 1 of Publication I] (reprinted with permission by Elsevier) (a) Five representative geometrical structures of the functionalized MXenes. (b) An illustrative description of the structure, electronic, and magnetic properties of carbide MXenes obtained from ab initio calculations using density-functional theory. For each MXene, information of electronic property (insulator, metal or semimetal), magnetic property (non-magnetic, ferromagnetic, and antiferromagnetic) as well as the ground state structure and the formal d^n configuration are presented.

process, e.g. hydrofluoric acid [17, 16]. The O and F terminations on M_2C MXenes are considered as T atoms (termination groups) in this study. The T atoms can occupy 3 distinct positions on the M_2C layer, i.e., the H site (hollow site), C site (carbon-top site), and the T site (transition metal top site), respectively. Accordingly, five different structures (HH, CC, TT, HC, and CT) are considered in our calculations.

3.3.2 Formal oxidation numbers and related properties

Figure 3.1 (b) summarizes the calculated properties of the carbide MXenes obtained in this work. Formal d^n configurations ($n = 0 \sim 3$) for M elements in M_2CO_2 and M_2CF_2 based on the usual oxidation number have been defined for the analysis with the typical octet rule.

First, typical oxidation numbers are assigned as C: -4, O: -2, and F: -1. The oxidation numbers of M elements are +4 in M_2CO_2 and +3 in M_2CF_2 imposed by the octet rule. After assigning the oxidation numbers, formal d^n configurations for M elements are defined, which show the number of d electrons (d^n configurations) belonging to the M element. As a representative example, Ti has its outermost electron configuration of $3d^2 4s^2$, Ti^{4+} in Ti_2CO_2 is assigned to the d^0 configuration after 4 electrons are removed, and Ti^{3+} in Ti_2CF_2 is assigned to the d^1 configuration.

The d^n configuration offers an intuitive description of the electronic and magnetic properties of MXenes. For example, the d^0 MXenes (9 MXenes labeled with d^0 in Fig. 3.1 (b)) were predicted as insulators due to the empty d band [15]. For d^n configurations of $n > 0$, electrons are filling d shells, which would lead to the metallic or magnetic properties of d^n MXenes. The DFT calculations predict most of the d^n ($n > 0$) MXenes are metallic and three of the MXenes are magnetic (V_2CO_2, V_2CF_2, and Mo_2CF_2).

For an additional note, the oxygen terminated MXenes having transition metals belonging to group-three (Sc_2CO_2, Y_2CO_2, and La_2CO_2) have also been assigned to d^0 MXenes because their HC ground state structure (one oxygen is not located on the transition metal but the carbon) takes three electrons from M (= Sc, Y, or La) elements, leading to d^0 configurations and insulating properties with finite band gaps.

3.3.3 Ground state configurations predicted by various XC functionals

Density-functional theory was used to determine the ground state structures of carbide MXenes using PBE-GGA [29], PBE+U [69] (U= 3 eV, U= 5 eV for transition metal d states), and SCAN [33] functionals across five different termination configurations (HH, CC, TT, HC, CT).The obtained ground state structures and their relative total energies are summarized in Table 3.1.

TABLE 3.1: [From Table 1 of Publication I] (reprinted with permission by Elsevier) The ground state atomic configurations of MXenes among 5 possible atomic structures (HH, CC, TT, HC, CT displayed in Fig. 3.1) and configurations of the second stable structure (the type of structure, the relative total energy in parentheses) obtained by PBE, SCAN and PBE+U(U= 3 eV on transition metal d states) functionals. SCAN and PBE+U functional predict the same ground state structure with PBE functional except for two cases i.e., Hf_2CF_2 and Ta_2CF_2.

	PBE	PBE+U (U=3 eV)	SCAN
Category: d^0 type-1			
Sc_2CO_2	HC(CC,0.136),NM	HC(CC,0.071),NM	HC(CC,0.168),NM
Y_2CO_2	HC(CC,0.144),NM	HC(CC,0.132),NM	HC(CC,0.174),NM
La_2CO_2	HC(CC,0.403),NM	HC(CC,0.374),NM	HC(CC,0.384),NM
Category: d^0 type-2			
Ti_2CO_2	HH(HC,0.768),HH	HH(HC,0.892),NM	HH(HC,0.855),NM
Zr_2CO_2	HH(HC,0.903),NM	HH(HC,0.994),NM	HH(HC,0.903),NM
Hf_2CO_2	HH(HC,0.982),NM	HH(HC,1.093),NM	HH(HC,1.058),NM
Sc_2CF_2	HH(HC,0.590),NM	HH(HC,0.292),NM	HH(HC,0.650),NM
Y_2CF_2	HH(HC,0.504),NM	HH(HC,0.553),NM	HH(HC,0.555),NM
La_2CF_2	HH(HC,0.342),NM	HH(HC,0.388),NM	HH(HC,0.339),NM

First of all, most of the MXenes (15 cases among 22 MXenes) have HH structure as their ground state structure, and d^0-type1 MXenes have HC structure as their ground state structure, which are in agreement with previous DFT studies of MXenes [16, 17]. Whereas SCAN and PBE+U mostly do not change the ground structure from PBE results, two exceptional cases are found: Hf_2CF_2 and Ta_2CF_2. Their ground state structures with PBE functional are Hf_2CF_2 (HH) and Ta_2CF_2 (HH), but changed to Hf_2CF_2 (HC) and Ta_2CF_2 (CC) with SCAN and PBE+U functionals. For these two cases, I further examined dynamical stability with phonon dispersions calculation with both PBE and SCAN functionals. It is demonstrated that Hf_2CF_2 (HC) and Ta_2CF_2 (CC) are dynamically unstable. Hf_2CF_2 (HH) and Ta2CF2 (HH) are also shown to be dynamically unstable. This suggests that PBE+U and SCAN functionals predict ground state structures correctly. As demonstrated here, +U corrections or other functionals (HSE, SCAN, and so on) should not be regarded as electronic perturbations on top of structures evaluated by PBE, but rather their

results should be carefully considered when predicting the structural and vibronic properties of MXenes. Intriguingly, the CC structure of Ta_2CF_2 exhibits a semimetal character similar to Mo_2CF_2 and W_2CF_2 which were previously reported as topological insulators [98, 99]. This implies that Ta_2CF_2 is also a topological insulator like Mo_2CF_2 and W_2CF_2, as shown in Fig. 3.4.

3.4 Electronic and magnetic properties of carbide MXenes

Once the ground state structures of carbide MXenes are clarified, the electronic structures of carbide MXenes were extensively studied with PBE, PBE+U, SCAN, HSE06 and functionals. The 22 carbide MXenes have been categorized into d^0-type1, d^0-type2, d^1, d^2 and d^3 with their formal d^n configurations of M elements which are intimately related to their electronic and magnetic properties. Among the 22 MXenes reported in this work, three magnetic MXenes: V_2CO_2, V_2CF_2, and Mo_2CF_2 were not reported in previous works, to the best of my knowledge. The electronic structures and magnetic phases of these three MXenes are discussed with their vibronic properties and dynamic stability.

3.4.1 d^0-type1 MXenes: Sc_2CO_2, Y_2CO_2, La_2CO_2

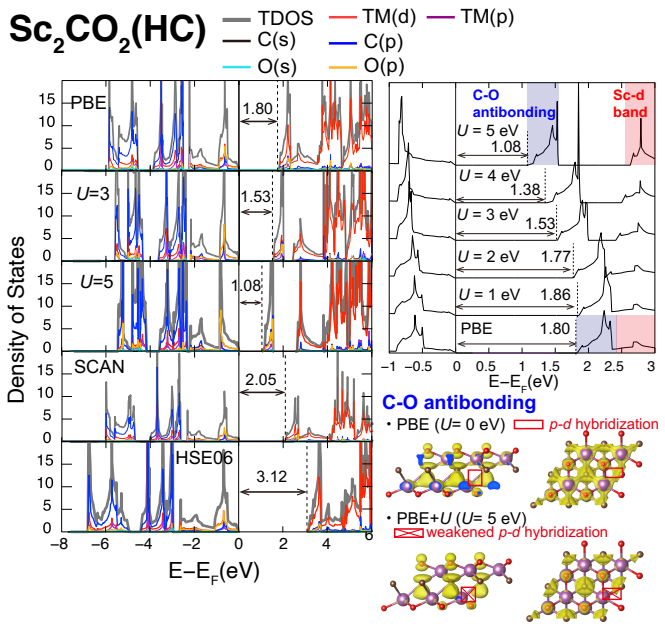

FIGURE 3.2: [From Fig. 2 (a) of Publication I] (reprinted with permission by Elsevier) The density of states of Sc_2CO_2 (HC structure) obtained with PBE, PBE+U, SCAN, and HSE06 functionals and their partial charge densities related to the C-O antibonding of Sc_2CO_2 (HC structure). Density of states of Sc_2CO_2 (HC structure) is shown as representative cases of d^0-type1 categories. Density of states of PBE+U calculations with various U parameters (U= 0∼5 eV) are illustrated with the denoted bandgap (in eV). The top view and side view of partial charge densities of the C-O antibonding obtained with PBE and PBE+U (U= 5 eV) are shown. The isosurface cut-off of the partial charge density plots is 0.01e/bohr^3.

The d^0-type MXenes Sc_2CO_2, Y_2CO_2, and La_2CO_2 should be differentiated from the other d^0 MXenes due to their unconventional HC structure. As a representative case of d^0-type1 MXenes, the density of states of Sc_2CO_2 obtained using PBE, PBE+U (U= 3 eV, 5 eV), SCAN, and HSE06 functionals are presented in Figure 3.2. Unoccupied levels of Sc_2CO_2 are dominantly contributed from the transition metal (TM) d states with a weak hybridization between O-p states and C-p states. Sc_2CO_2, Y_2CO_2, and La_2CO_2 band gaps are formed by completely unoccupied bands. It is noted that SCAN and HSE06 shift the bonding states of TM-d O-p states and TM-d C-p states downward. This indicates that SCAN and HSE06 reduce self-interaction error of the PBE functional and thus make bonding states more energetically deeper and spatially localized. Conversely, the PBE+U correction does not affect the bonding states selectively in contrast to SCAN and HSE06 functionals because the correction affects transition metal d states selectively (not to p states).

The type functional and various +U parameters change the prediction of the band gaps of d^0-type1 MXenes. The band gap of Sc_2CO_2 is enlarged from

1.77 eV (PBE) to 2.13 eV (SCAN) and 3.12 eV (HSE06). The band gap opening can be attributed to the reduction of the self-interaction and partially restores the functional discontinuity of SCAN and HSE06 functionals compared to the erroneous PBE functional [52, 100]. On the other hand, the band gap gets narrower than the PBE band gap (1.53 eV with U= 3 eV and 1.08 eV with U= 5 eV) after PBE+U (U= 3 eV, 5 eV) is employed. The variation of the bandgap and electronic structure with various U parameter of PBE+U funcitonal (U = $0 \sim 5$ eV) of Sc_2CO_2 (HC structure) are described in Figure 3.2. This band gap narrowing is seemingly not induced by the downshift of unoccupied d levels, but invoked by a considerable downshift of the C-O antibonding state with the $+U$ correction. For U= 3 eV and 5 eV, the C-O antibonding state is completely isolated at the mid-gap. The side view and top view of partial charge density of C-O antibonding state of PBE and PBE+U (U= 5 eV) functionals are shown in the Figure 3.2. While a chemical connection between scandium and carbon atoms is observed in PBE result, the bonding is being disconnected in PBE+U (U= 5 eV) result. This shows that $+U$ correction exerted on transition metal d-states induces artificially weakening $p - d$ hybridization in contrast to the meta-GGA and hybrid functional (SCAN and HSE06) which enhance $p - d$ hybridization by making p states of carbon and functional groups more localized.

3.4.2 d^0-type2 MXenes: Ti_2CO_2, Zr_2CO_2, Hf_2CO_2, Sc_2CF_2, Y_2CF_2, and La_2CF_2

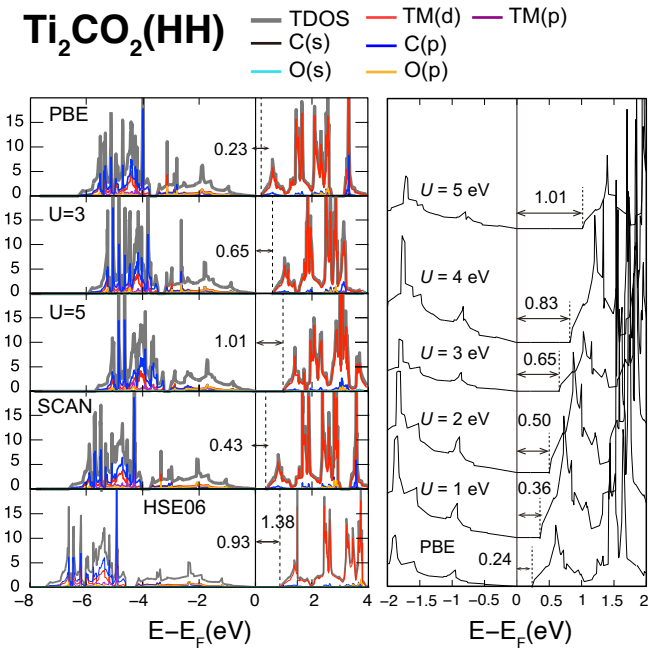

FIGURE 3.3: [From Fig. 2 (b) of Publication I] (reprinted with permission by Elsevier) The density of states of Ti_2CO_2 (HH structure) obtained with PBE, PBE+U, SCAN, and HSE06 functionals. Density of states of PBE+U calculations with various U parameters (U= 0∼5 eV) are illustrated with the denoted bandgap (in eV).

d^0-type2 MXenes have an HH type structure as shown in Figure 3.3. The density of states of Ti_2CO_2 is presented as a representative case of d^0-type2 MXenes. It is shown that PBE+U, SCAN, and HSE06 functionals increase the band gap compared to the PBE result, while any remarkable change of the valance band and conduction band structures are not introduced at vicinity of the Fermi level. Similar to cases of d^0-type1 MXenes, SCAN and HSE06 functionals bring down the bonding states of Ti_2CO_2 (located at −6 eV) and shrink lattice constants of d^0-type2 MXenes compared to that of PBE functional. This indicates that SCAN and HSE06 functionals enhance chemical interaction between TM-d and C-p states, while PBE+U selectively localizes TM-d states and rather reduces the chemical bonding in-between C-p and TM-d. The bandgap is monotonically increased from 0.24 eV (PBE) to 1.01 eV (PBE+U, U = 5 eV) as the U parameter is increased, which is attributed to the increased electron correlation effect of transition metal d states induced by the +U correction.

3.5 Magnetic and vibronic properties of d^n $(n > 0)$ MXenes

d^n $(n > 0)$ MXenes have occupied d shells that are anticipated to induce metallic or magnetic properties that d^0 MXenes do not exhibit. From DFT calculations, it has been found that SCAN, HSE06, and PBE+U predict three magnetic MXenes (V_2CO_2, V_2CF_2, and Mo_2CF_2) while the other d^n $(n > 0)$ MXenes remain nonmagnetic even with a strong $+U$ correction (U= 5 eV) and HSE06 functional. For Hf_2CF_2 and Ta_2CF_2, the ground state structures are predicted as HC and CC structures using PBE+U, SCAN and HSE06 functionals, while PBE functional predicts HH structure for their ground state structures. Among nonmagnetic MXenes, Mo_2CO_2 and W_2CO_2 are shown to be topological insulators, as reported in previous studies [98, 99]. The vibronic properties of three magnetic MXenes are presented to explore the intimate correlation between magnetic properties and the dynamical stability of magnetic MXenes.

3.5.1 Nonmagnetic d^n $(n > 0)$ MXenes

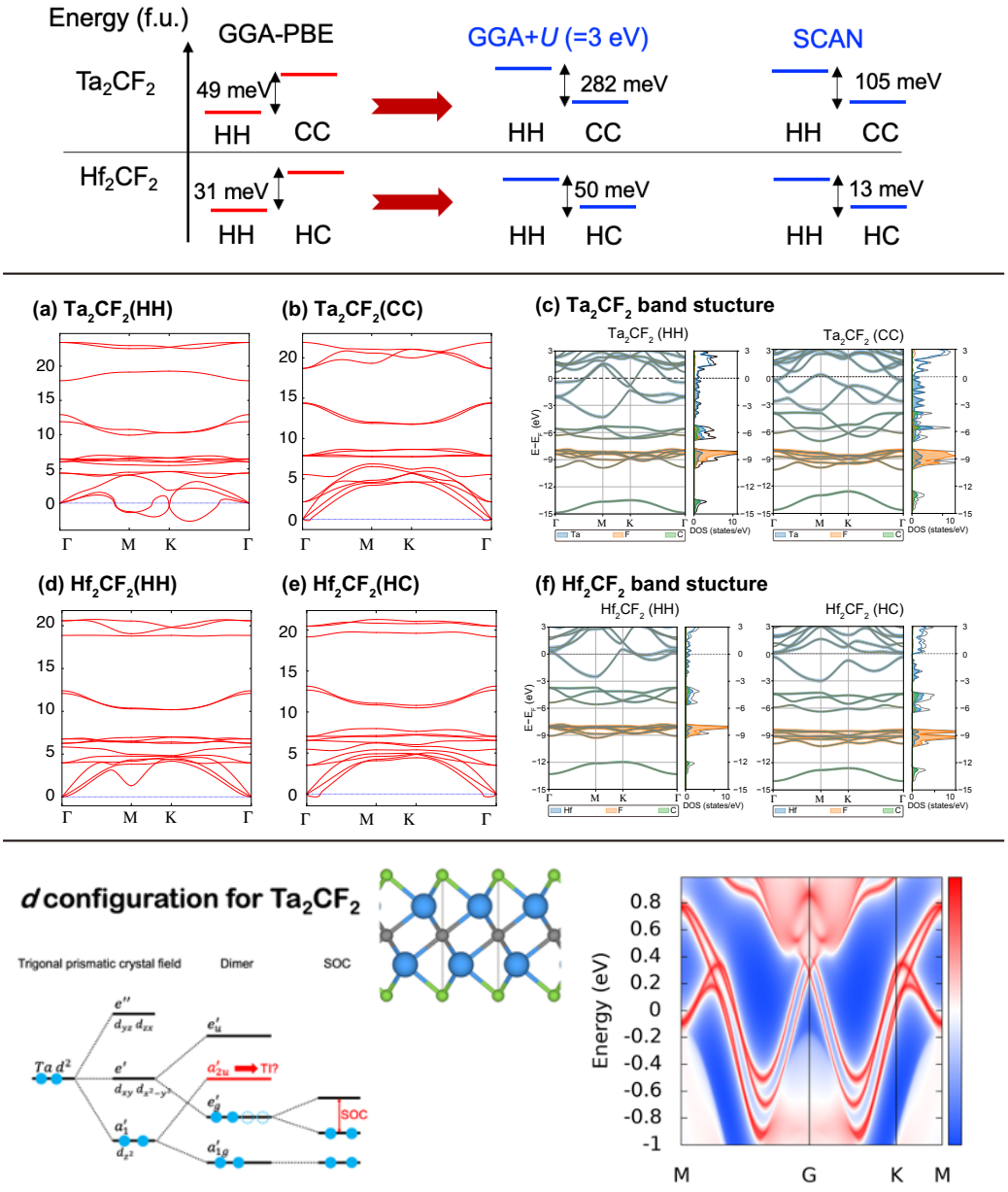

FIGURE 3.4: Top panel: Alternating of relative stability of Ta_2CF_2 and Hf_2CF_2 between different termination positions by changing exchange-correlation functional. Middle panel: [From Fig. 3 of Publication I] (reprinted with permission by Elsevier) Phonon dispersions and band structures of Ta_2CF_2 (HH and CC structure) and Hf_2CF_2 (HH and HC structure). Phonon dispersions and electronic band structures of Ta_2CF_2 and Hf_2CF_2 are calculated by SCAN functional. Bottom panel: the electronic structure of Ta_2CF_2 behaving as a topological insulator with a gigantic gap ~ 0.7 eV [101] (private communication).

By adopting PBE+U, SCAN functionals, Hf_2CF_2 and Ta_2CF_2 are found to be different ground state structures compared to that PBE predicts. While PBE assigns the HH structure to their ground state structures of Hf_2CF_2 and Ta_2CF_2, PBE+U and SCAN predict the HC structure of $Hf_2CF_2$and the CC structure of Ta_2CF_2. In Figure 3.4, the phonon dispersions and band structures of $Hf_2CF_2$and Ta_2CF_2 calculated by SCAN are shown. In the phonon dispersions, it has been found that Ta_2CF_2 (HH) is dynamically unstable, whereas Ta_2CF_2 (CC) dynamically stable. Remarkably, Ta_2CF_2 is a semimetal in analogy to Mo_2CO_2 and W_2CO_2, which were reported as topological insulators [98, 99]. Kang et al., revealed that Ta_2CF_2 is a topological insulator whose SOC (spin-orbit coupling) gap is close to 0.7 eV evaluated by PBE0 hybrid functional [101] (private communication).

For Hf_2CF_2, both Hf_2CF_2(HH) and Hf_2CF_2(HC) are shown to be dynamically stable and Hf_2CF_2(HH) and Hf_2CF_2(HC) exhibit metallic and semiconducting characteristics. The two distinct phases of Hf_2CF_2 are similar to the polymorph 1T' (metallic) and 2H (semiconducting) phases of transition metal dichalcogenides. The energy difference between Hf_2CF_2(HH) and Hf_2CF_2(HC) (less than 50 meV/cell) would imply the feasibility of phase engineering of Hf_2CF_2 in-between Hf_2CF_2(HH) (metal) and Hf_2CF_2(HC) (semiconductor), which is already experimentally realized in transition metal dichalcogenides [102].

3.5.2 Carbide MXenes with magnetic order: V_2CO_2, V_2CF_2, and Mo_2CF_2

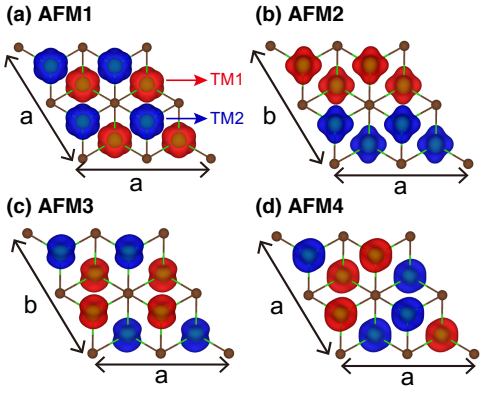

FIGURE 3.5: [From Fig. 4 of Publication I] (reprinted with permission by Elsevier) The spin polarization density of V_2CF_2 for different AFM patterns considered in this work. Four different AFM phases (a) AFM1, (b) AFM2, (c) AFM3, (d) AFM4 are tested in our calculations. Blue and red show up- and down-spin polarization densities residing in transition metal atoms that are labeled as TM1 (up spin) and TM2 (down spin).

Three of carbide MXenes, V_2CO_2, V_2CF_2, and Mo_2CF_2, were found to be magnetic when SCAN, PBE+U, and HSE06 are applied, while PBE always predicts the nonmagnetic phase of them. This indicates that PBE functional fail to predict magnetic phases that originate from strongly localized d-electrons. Thee electronic structures and phonon dispersions for nonmagnetic phase and five magnetic phases, including antiferromagnetic phases (AFM1, AFM2, AFM3, and AFM4 in Figure 3.5) and ferromagnetic phase (FM) with PBE, SCAN, HSE06, and PBE+U (U= 3 eV, 5 eV) have been calculated to understand the magnetic phases of MXenes and their magnetic and vibronic properties in detail.

V_2CO_2 : magnetic property and dynamical stability

The discussion of a representative magnetic MXene V_2CO_2 is firstly presented. A few number of DFT studies have explored the electronic and magnetic properties of vanadium carbides using PBE functional to achieve practical predictions for Li ion battery applications [103, 94, 104]. In previous studies, V_2CO_2 and V_2CF_2 were revealed as nonmagnetic with the HH ground state structure [103, 94]. Previous studies applied the PBE+U method for vanadium carbides. For example, Champagne *et al.* reported the nonmagnetic phase of V_2CO_2 in the HH structure, but the HH structure is dynamically unstable [94]. Hu *et al.* et al., reported the antiferromagnetic ground state of V_2CF_2 obtained by DFT calculation with PBE+U (U= 4 eV) [105]. The description of vanadium carbides has been confused due to inconsistently applied various methods for different cases (spin polarized or unpolarized, and PBE or PBE+U). Remarkably, Champagne *et al.* also reported a symmetry broken V_2CO_2 (HH) structure as the ground state found in their study [94]. This implies the Peierls like instability of non-magnetic V_2CO_2 that might be caused by spurious localization of d states whose stability competes with antiferromagnetic ordering as previously shown for magnetic surface states [106, 107].

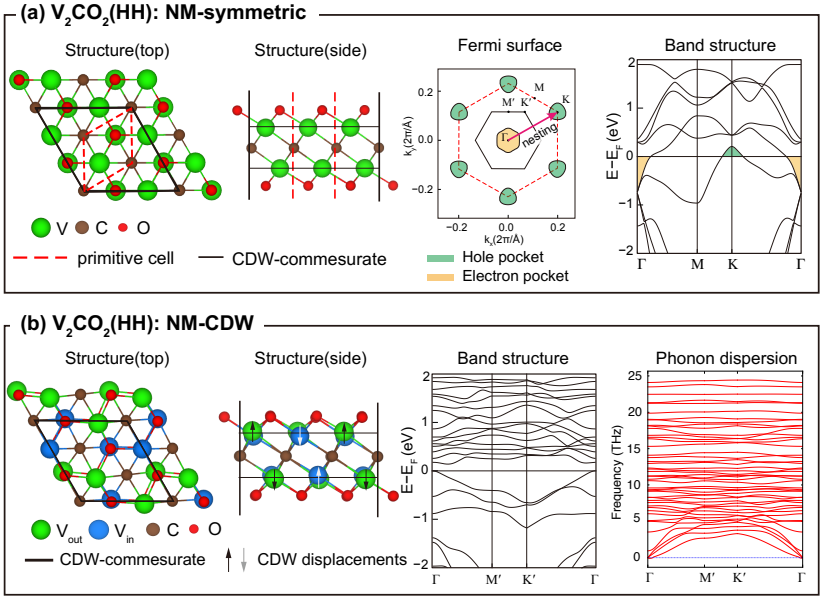

FIGURE 3.6: [From Fig. 5 of Publication I] (reprinted with permission by Elsevier) The atomic structures and electronic structures of V_2CO_2(HH) in symmetric and CDW structure with the phonon dispersion of CDW structure obtained using PBE functional. (a) The electronic structures are shown with the band structure and the Fermi surface, which exhibits electron- and hole-pocket implying the Peierls instability via Fermi surface nesting also shown in the phonon dispersion as imaginary modes. The primitive cell and the CDW-commensurate cell are delineated with dash and bold lines. The nesting vector from $\Gamma \rightarrow$ K is shown. (b) The CDW structure is illustrated with the distortion displacements of vanadium atoms from the symmetric structure induced by the CDW distortion.

To resolve the confusion of inconsistency reported by previous studies on V_2CF_2 and V_2CO_2 [103, 94, 105], the electronic structure and dynamic stability of V_2CO_2(HH) with the PBE functional were explored. In PBE results, V_2CO_2(HH) does not show magnetism despite of the partially filled d-shall (d^1 configuration) of the vanadium atom in V_2CO_2. By the fact that the partially filled d band may induce large Peierls instability through enhanced electron-phonon coupling by Fermi surface nesting [108]. To verify the existence of Fermi surface nesting in the nonmagnetic V_2CO_2 band structure, the band structure and Fermi surface of the nonmagnetic phase V_2CO_2 in the $P31m$ symmetry group (NM-symmetric structure) are presented in Figure 3.6 (a). From the Fermi surface and band structure, a hole-pocket residing around the Γ point and electron-pockets around the K point are observed. The presented electron- and hole-pockets induce the Peierls instability caused by the Fermi-surface nesting, which is again shown as the dynamical instability in the phonon dispersion of the V_2CO_2 NM-symmetric structure.

The dynamical instability of the V_2CO_2 NM-symmetric structure induces the Peierls distortion in a larger commensurate unit, which would stabilize the structure accompanied with a charge density wave (CDW) with spontaneous symmetry breaking [108, 109, 110]. Searching for the CDW phase of V_2CO_2(HH), the NM-symmetric structure has been optimized in its commensurate $\sqrt{3}\times\sqrt{3}$ supercell to consider the instability at the K point of the phonon diseprsion. The fully relaxed structure in the $\sqrt{3} \times \sqrt{3}$ supercell of the nonmagnetic V_2CO_2 (NM-CDW) structure is presented in Figure 3.6 (b). The distorted NM-CDW structure is belong to the Cm space group lowered from $P31m$ space group. The NW-CDW V_2CO_2 exhibits CDW behavior is observed with outward/inward shifts of vanadium atoms in the vertical direction (illustrated with blue and green colors in Figure 3.6 (b)) accompanied with oscillationary behavior in electron numbers of vanadium atoms obtained with Bader charge analysis [111] fluctuating between 2.91 and 2.79 electrons. Remarkably, the CDW distortion opens up a band gap, therefore removing dynamical instability via a metal-insulator transition. As presented in the phonon dispersion in Figure 3.6 (b), the NM-CDW structure is being dynamically stable, while the NM-symmetric structure is dynamically unstable. The total energy lowering through the structure distortion from the NM-symmetric structure to the NM-CDW structure is estimated about 0.06 eV/cell.

In a series of previous studies, it has been shown that the CDW behavior and magnetic ordering would compete against each other when stabilizing the Peierls instability [106, 107, 112, 113]. The PBE calculations presented in this work do not exhibit any magnetic ordering for V_2CO_2 and thus prefers the delocalized states due to large self-interaction error (SIE) of the PBE functional [114]. In order to obtain a correct description free of self-interaction error bias, SCAN and HSE06 and Hubbard-U corrections were applied to DFT calculations of the electronic, magnetic, and vibronic properties of V_2CO_2.

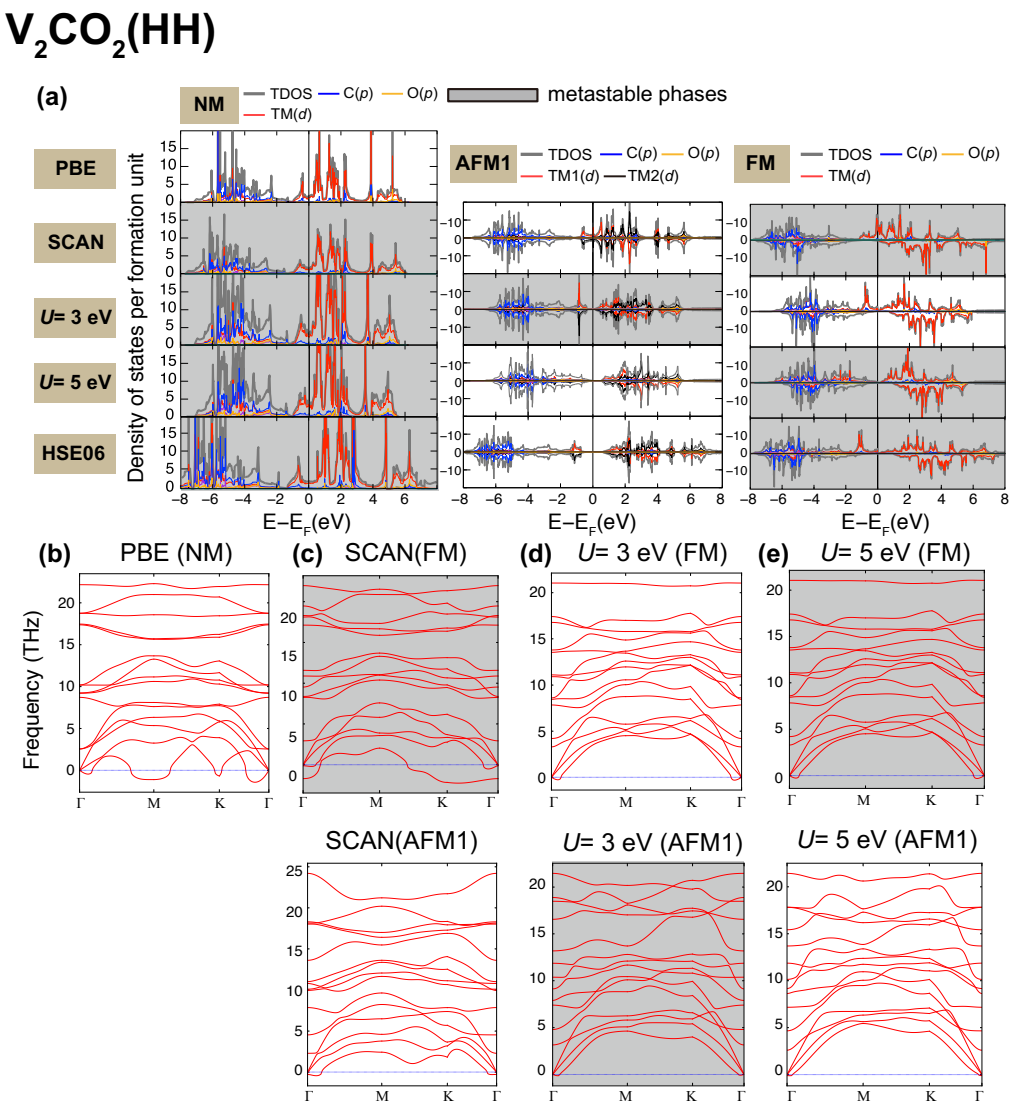

FIGURE 3.7: [From Fig. 6 of Publication I] (reprinted with permission by Elsevier) The density of states and phonon dispersions of magnetic and nonmagnetic phases of V_2CO_2. (a) Density of states of V_2CO_2 in nonmagnetic (NM) and magnetic phases (AFM1 and FM) obtained with PBE, SCAN, PBE+U (U= 3 eV, 5 eV), and HSE06 functionals. (b), (c), (d), and (e) are phonon dispersions of magnetic (SCAN, PBE+U) and nonmagnetic (PBE) phases. The density of states and phonon dispersions of metastable states are highlighted with gray shading.

Figure 3.7 presents the density of states of magnetic phases and phonon dispersions of V_2CO_2(HH) calculated with PBE, SCAN, PBE+U and HSE06 functionals. From the PBE results, V_2CO_2(HH) is predicted as a metal and its phonon dispersion has instabilities at M and K points. While PBE functional only gives nonmagnetic phase due to self-interaction error, PBE+U, SCAN, and HSE06 predict magnetic phases of V_2CO_2. This indicates that meta-GGA (SCAN) and hybrid functionals (HSE06), and $+U$ corrections need to examine for predicting the magnetic phases of MXenes. In Figure 3.7, phonon dispersions and density of states of AFM1 phases are presented. The AFM1 phase has been predicted as the most energetically stable AFM phase among considered four AFM phases. The prediction of the ground state are affected by the choice of the functional. AFM1 phase is predicted as the ground state with SCAN, HSE06, and PBE+U (U= 5 eV) funcitonals, while FM phase is being as the ground state with PBE+U (U= 3 eV). Because the relatively small total energy difference between AFM1 and FM phases obtained with SCAN, HSE06, and PBE+U (less than 40 meV/cell), the ground state configuration of V_2CO_2 is affected sensitively by changing the functionals or $+U$ parameter. It is further noted that the CDW structure of V_2CO_2(HH) (Cm symmetry, nonmagnetic) has been also optimized with PBE+U, SCAN, and HSE06 functionals and its total energies are higher than the total energies of magnetic phases. While the net magnetic moment of the V_2CO_2 for the FM phase is expected to be 2.0 μ_B/cell from the d^1 configuration of vanadium, the obtained total magnetic moments of the FM phase were 1.78 μ_B/cell (SCAN) and 2.0 μ_B/cell (PBE+U and HSE06), which reflect moderate d electron localization of SCAN functional compared to HSE06. As shown in 3.7 (b), the magnetic phases of V_2CO_2 are dynamically stable in contrast to the nonmagnetic phase of PBE (HH, symmetric). This supports the fact that the CDW behavior and magnetic ordering are competing with each other and magnetic ordering (antiferromagnetic and ferromagnetic phase) is dominant with SCAN, HSE06 and PBE+U functionals for V_2CO_2 [106, 107, 112, 113]. This suggests that electron correlation effects of different functional not only affect the electronic and magnetic properties of MXenes but also the dynamical stability therefore affecting the *vibrionic properties* of carbide MXenes.

V_2CF_2 : magnetic property and dynamical stability

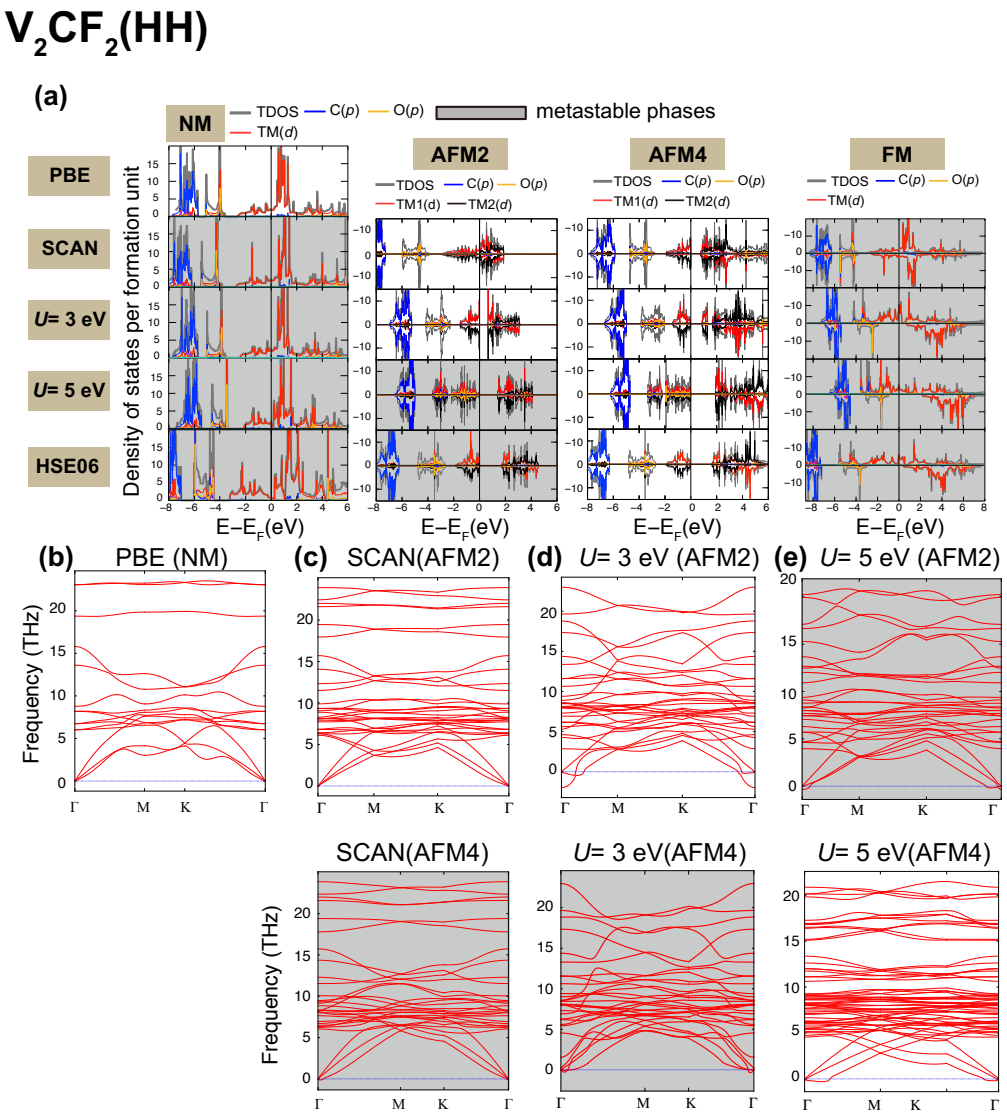

FIGURE 3.8: [From Fig. 7 of Publication I] (reprinted with permission by Elsevier) The density of states and phonon dispersions of magnetic and nonmagnetic phases of V_2CF_2. (a) Density of states of V_2CF_2 in nonmagnetic (NM) and magnetic phases (AFM1 and FM) obtained with PBE, SCAN, PBE+U (U= 3 eV, 5 eV), and HSE06 functionals. (b), (c), (d), and (e) are phonon dispersions of magnetic (SCAN, PBE+U) and nonmagnetic (PBE) phases. The density of states and phonon dispersions of metastable states are highlighted with gray shading.

The electronic structures, magnetic properties, and phonon dispersion of V_2CF_2 (HH) are presented in Figure 3.8. In analogy to V_2CO_2, it has been observed that the phonon dispersions of nonmagnetic V_2CF_2(HH) of PBE functional does not show any dynamical instability or CDW distortions in contrast to the V_2CO_2 (HH). The predicted ground state magnetic phase of V_2CF_2 also depends on the type of applied functional; PBE functional predicts the nonmagnetic phase, while SCAN and PBE+U (U= 3 eV) predict the AFM2 phase and HSE06 and PBE+U (U= 5 eV) predict the AFM4 as the ground state configuration. The energy difference between the AFM2 and AFM4 phases observed with SCAN, HSE06, and PBE+U (U = 3 eV) is relatively small (10 meV/cell), but PBE+U (U = 5 eV) is found to significantly stabilize the AFM4 phase by 70 meV/cell when compared to the AFM2 phase. The insulating/metallic behavior of V_2CF_2 also depends on type of functionals and its magnetic phases. The nonmagnetic phase is metallic for all functionals and the AFM4 phase is as an insulator with SCAN, PBE+U, and HSE06. While PBE+U and HSE06 predict a finite band gap for AFM4 phase, SCAN close the band gap and predict the metallic state of the AFM2 phase. The difference can be observed in electronic structures between the AFM2 and AFM4 phases at the location of C-p states. For SCAN results, the AFM2 phase has deeper C-p states (at -8 eV) compared to that of the AFM4 phase (at -6 eV). The lower energy level of the C-p states of the AFM2 phase may induce stronger hybridization between the C-p and TM-d states. The metallic behavior observed in AFM2 phase using SCAN functional may be caused by the delocalization of the d states originating from its strong $p - d$ hybridization. On the contrary, HSE06 gives a finite band gap for AFM2 and AFM4 phases, which again shows that SCAN functional would have a residual self-interaction error on localized transition metal d states.

For the FM phase, the half-metallic behavior is obtained from PBE+U and HSE06 while SCAN gives the FM phase as a trivial metal. This half-metallic behavior would be induced by the gap in the down spin channel of d states. On the contrary, SCAN closes the gap in the down spin due to its residual self-interaction error. The total energy difference between the AFM and FM phases obtained with PBE+U, SCAN, and HSE06 is more than 400 meV/cell. Therefore, it is anticipated that the FM phase is hardly realized in the usual experimental environments.

Mo_2CF_2 : magnetic property and dynamical stability

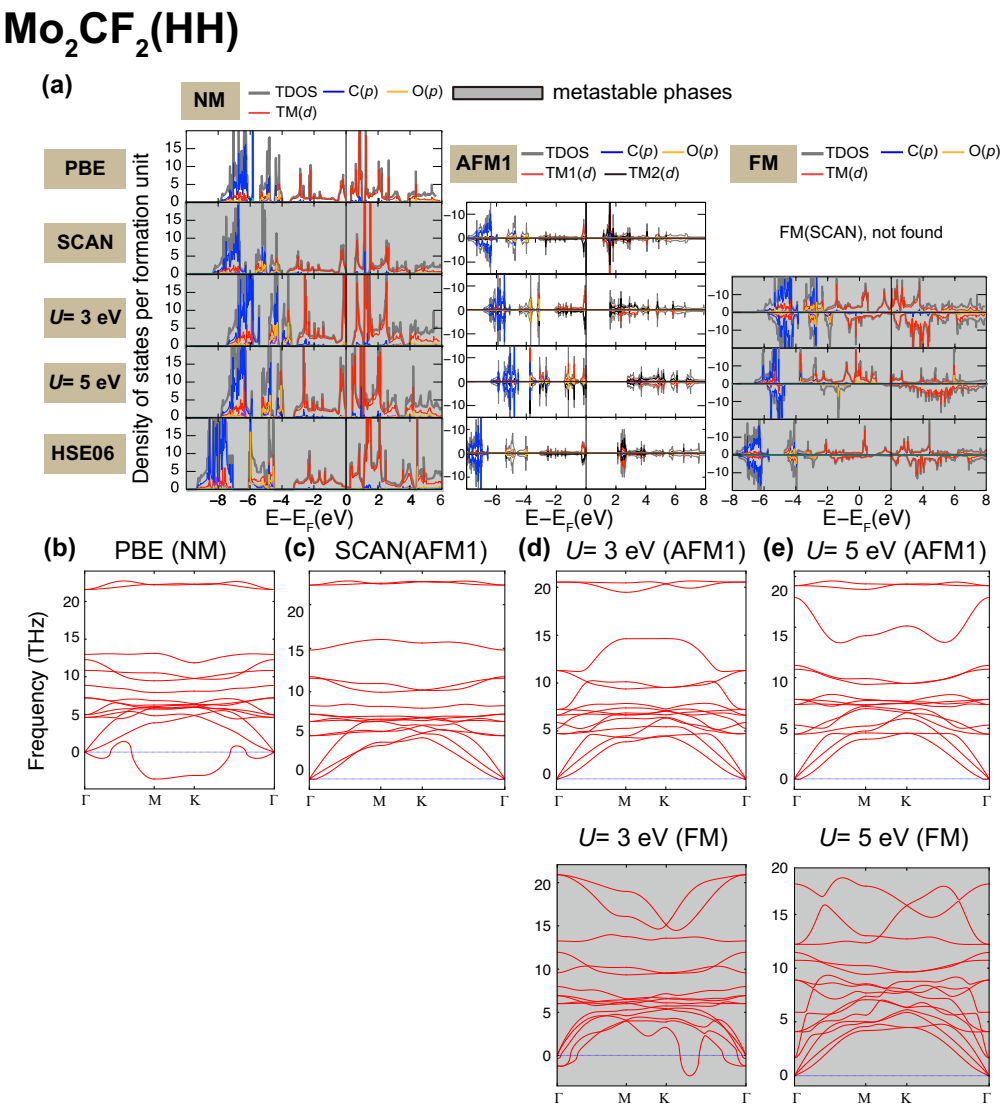

FIGURE 3.9: [From Fig. 8 of Publication I] (reprinted with permission by Elsevier) The density of states and phonon dispersions of magnetic and nonmagnetic phases of $MoCF_2$. (a) Density of states of $MoCF_2$ in nonmagnetic (NM) and magnetic phases (AFM1 and FM) obtained with PBE, SCAN, PBE+U (U= 3 eV, 5 eV), and HSE06 functionals. (b), (c), (d), and (e) are phonon dispersions of magnetic (SCAN, PBE+U) and nonmagnetic (PBE) phases. The density of states and phonon dispersions of metastable states are highlighted with gray shading.

Finally, the density of states and phonon dispersions of Mo_2CF_2(HH) in various magnetic phases are shown in Fig. 3.9. First of all, the HH structure of Mo_2CF_2 has been predicted to have the most structure among the five configurations in PBE, SCAN and PBE+U (U= 3 eV) calculations, as shown in Table 3.1. Khazaei *et al.* reported that Mo_2CF_2 can be a promising thermoelectric material due to its large Seebeck coefficient which originated from the insulating property [115]. The calculated results show that Mo_2CF_2 has a finite band gap in both the NM and AFM phases, but the band gap of the AFM phase is approximately two times larger than that of the NM phase as predicted with SCAN, PBE+U, and HSE06 functionals. The total energy of the AFM1 phase is much lower than the NM phase by 200 meV per/cell. Moreover, the phonon dispersions of the AFM1 phase of Mo_2CF_2 with PBE+U and SCAN are also shown to be dynamically stable in contrast to the dynamically unstable nonmagnetic V_2CF_2.

The calculated results in this section again demonstrate that many of previous studies using PBE functional predicted the NM phase of Mo_2CF_2 with a significantly underestimated band gap and incorrect dynamical stability. According to the predictions in this work, Mo_2CF_2 has a larger band gap and dynamical stability with the AFM1 phase. Generally, the larger insulating gap results in a higher Seebeck coefficient, and therefore a higher thermoelectric efficiency [115].

3.6 Chapter summary

In this chapter, a comprehensive DFT study for 22 carbide MXenes using PBE, PBE+U, the meta-GGA (SCAN), and the hybrid functional (HSE06) has been carried out for demonstrating how the choice of functionals affect the predictions of electronic, magnetic, and structural properties of MXenes. In the obtained results, for 17 out of the 22 systems, all functionals employed in this work (PBE, PBE+U, SCAN, and HSE06) have been shown to give qualitatively similar results in predicting the same ground state structure, and similar electronic and magnetic properties. However, for 5 remarkable exceptional cases, PBE+U, SCAN, and HSE06 give significantly contrasting electronic structures, and sometime leading to different ground state structures and different magnetic configurations.

The obtained results indicate that the different functionals would bring different predictions on electronic structure, magnetic phases and dynamical stability of carbide MXenes. This would suggest that PBE-GGA can be used at the starting point of the research of MXenes while it may lead to qualitatively wrong results. PBE+U (PBE+ Hubbard type U correciton) offers a simple correction with a little computational cost despite of its limited correction only exerted to the orbitals the where $+U$ corrections are applied (mostly $3d$ states).

SCAN (a meta-GGA funcitonal) has shown to be a more balanced that also affect electronic states of $2p$ states, while the computational cost increase with a factor of $2 \sim 3$ from the PBE calculations. It was observed that SCAN functional does not always opens up $d - d$ gaps, which are opened in HSE06 or PBE+U calculations. This suggests that self-interaction error is partially corrected with SCAN funcitonal. HSE06 likely offers a balanced description of p and d states in carbide MXenes, but the computational cost is significantly increased from the PBE calculations (approximately $20 \sim 50$ times). I expect that this work provides a practical guideline for the choice of exchange-correlation functional of density-functional calculations for presenting convincible predictions for future MXene studies.

Chapter 4

Discovery of C_3 MXene electride family

This chapter overviews **Publication-2:** MXene Phase with C_3 Structure Unit: A Family of 2D Electrides, **Soungmin Bae** *et al.*, Advanced Functional Materials (2021): **31**, 2100009.

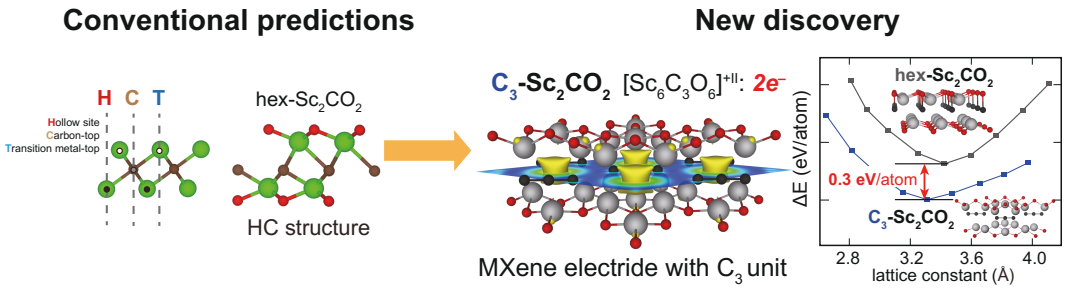

As discussed in the previous chapter, carbide MXenes with transition metal elements in the first column (Sc, Y, and La) have been predicted to have a HC structure whose spatial pattern of termination groups is unsymmetric on the upside and down side [15]. This broken symmetry is thought to result in massive ferroelectricity for Sc_2CO_2 [116].

While Sc_2CO_2 previously predicted as a ferroelectric material with its gigantic out-of-plane polarization, this work shows that the *true ground state phase* of Sc_2CO_2 is a centrosymmetric structure with C_3 carbon trimer which has been found to be two-dimensional electride. The C_3 MXene electrides have been also found for M_2CO_2 with M= Sc, Y, La, Lu, Tm, and Ho, this work reports a *family* of C_3 MXene electride. This chapter outlines the discovery of C_3 MXene electrides and discusses their electronic and vibrational properties that are able to be applied to several practical applications, such as cold electron emitters and anode materials for Li-ion batteries.

4.1 Research backgroud

4.1.1 Previous predictions of ferroelectric Sc_2CO_2

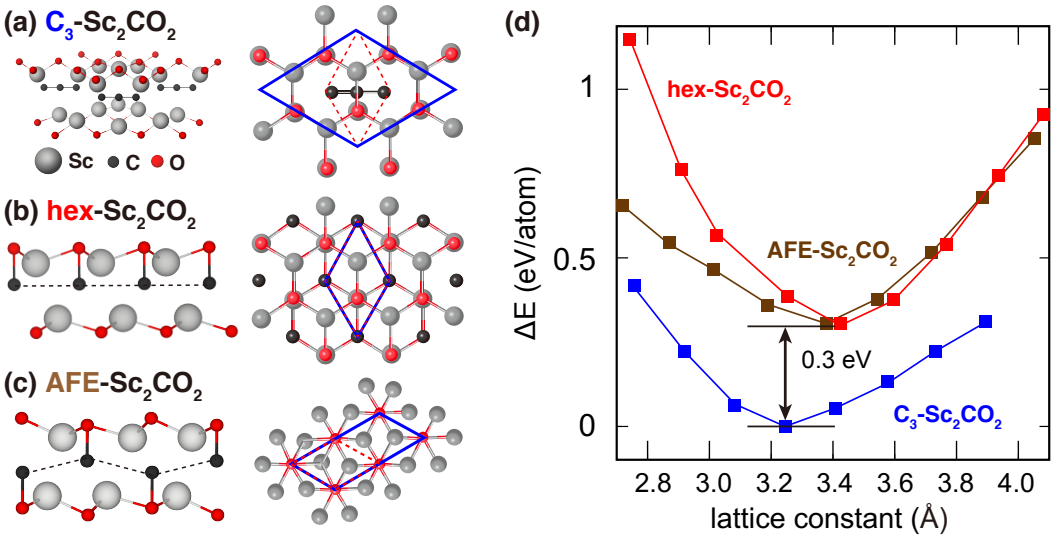

FIGURE 4.1: [From Fig. 1 of Publication II] (permitted by John Wiley & Sons) Structure and energetic stability of $C_3 - Sc_2CO_2$, hex $- Sc_2CO_2$ and AFE$-Sc_2CO_2$. Perspective and side views of (a) $C_3 - Sc_2CO_2$, (b) hex $- Sc_2CO_2$ and (c) AFE $- Sc_2CO_2$ (AFE: antiferroelectric). The blue lines delineate the primitive cell and the commensurate cell of $C_3 - Sc_2CO_2$, hex$-Sc_2CO_2$ and AFE $- Sc_2CO_2$ (2×1 and $\sqrt{3} \times \sqrt{3}$ of the hex $- Sc_2CO_2$ primitive cell, respectively) and the dashed lines depict the primitive cell of hex $- Sc_2CO_2$. (d) Relative total energy of $C_3 - Sc_2CO_2$, hex $- Sc_2CO_2$ and AFE $- Sc_2CO_2$ per atom as a function of lattice constant of the lattice constant (the lattice constant of $C_3 - Sc_2CO_2$ and AFE $- Sc_2CO_2$ scaled by $1/\sqrt{3}$ and $1/2$ for commensurability).

MXenes are class of two-dimensional (2D) systems composed of graphite like monolayers or multilayers of carbon or nitrogen (X) sandwiched between metal (M) layers, usually terminated by oxygen or fluorine and hydroxyl groups [117, 118, 119, 120, 23, 16, 121, 122]. Within many of MXene systems, the oxygen terminated scandium carbide MXene Sc_2CO_2 has received much attention due to its exotic giant polarization in the perpendicular direction to the basal plane, which brings strong piezoelectric effects and ferroelecticity [116, 123]. The extreme polarization of Sc_2CO_2 origintaes from its non-centrosymmetrical structure (the HC structure) with different bondings on either side of the carbon plane [15, 124, 125], which indicates that the system is violating the octet rule. The structures of Sc_2CO_2 in various phases are shown in Figure 4.1. Despite fascinating predictions of ferroelectric or anti-ferroelectric hexagonal phases of Sc_2CO_2 (AFE $- Sc_2CO_2$ or hex $- Sc_2CO_2$, respectively, henceforth), successful fabrications of them have not been reported yet [126, 127, 128].

4.1.2 Searching for the $C_3-Sc_2CO_2$ ground state structure within $\sqrt{3} \times \sqrt{3}$ commensurate unit

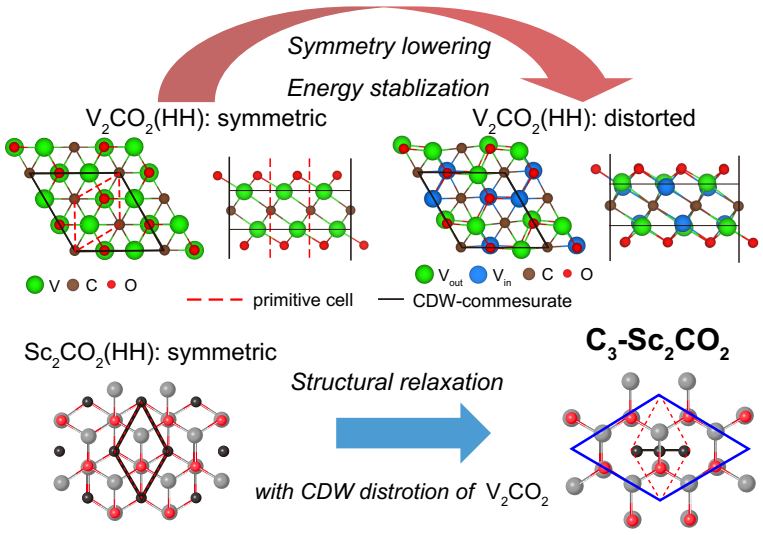

FIGURE 4.2: A concept art describing the optimization procedure of $C_3-Sc_2CO_2$. Adopting the distorted nonmagnetic V_2CO_2 to Sc_2CO_2(cf. Fig. 3.6 in chapter 3), the $C_3-Sc_2CO_2$ structure was obtained in the $\sqrt{3} \times \sqrt{3}$ commensurate unit through the structure optimization modifying the cell shape and atomic positions.

In chapter 3, a distorted centrosymmetric structure of V_2CO_2 was obtained for its non-magnetic phase accompanying a charge density wave and atomic distortions. This distortion refines the unit of simulation cell with a $\sqrt{3} \times \sqrt{3}$ unit of the primitive unit, as illustrated in Fig. 4.2. Including wider commensurate units and structural optimization with initial atomic distortions would present more stable configurations if the starting point is a metastable structure. For Sc_2CO_2, starting from the centrosymmetric structure, full structural optimization was performed with giving initial atomic distortions as same as the distortion of $\sqrt{3} \times \sqrt{3}$ V_2CO_2.

After the full optimization including the cell shape and atomic positions, the $C_3-Sc_2CO_2$ structure was achieved. The structure of $C_3-Sc_2CO_2$ is illustrated in Fig. 4.1 (c). The structure contains a C_3 carbon trimer at the middle of the cell instead of a hexagonal carbon network. As shown in Fig. 4.1 (d), $C_3-Sc_2CO_2$ is energetically stable compared to other metastable phases (hex-Sc_2CO_2 and AFE-Sc_2CO_2), therefore the discovered $C_3-Sc_2CO_2$ is the *true ground state*.

4.1.3 Polymorph of scandium carbides with various carbon guises

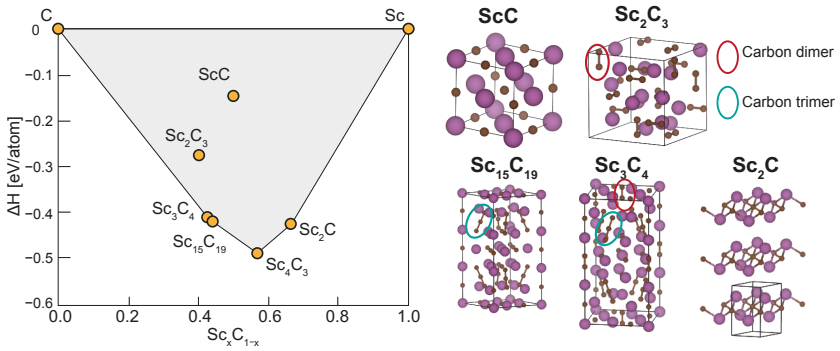

FIGURE 4.3: The convex hull of scandium carbides (left) and atomic structure of several phases (right). The convex hull was with OQMD database [129, 130] and atom structures were acquired from Materials Project [131]. The carbon dimers and trimers are highlighted with colored circles. Atomic structures are displayed using VESTA software [132].

Carbon is a core element that forms various organic materials and many carbides. The enormous number of carbon compounds appear to have originated from carbon's unique electronic structure, which manifests the diverse nature of its bonding nature [133]. Remarkably, scandium carbides have various forms such as ScC, ScC_2, Sc_2C_3, Sc_3C_4, $Sc_{13}C_{10}$, Sc_2C_C, and Sc_3C_{10} [134, 135, 136, 137, 138, 139, 140, 141, 142]. Carbon in these compounds exhibits diverse guises, including C_2 dimer (Sc_2C_3 and Sc_3C_4), C_3 trimer (Sc_3C_4), C_5 pentagon (Sc_3C_{10}), and $Sc_{20}C_{60}$ volleyballene [136, 143]), as well as hexagonal graphene 2D layers (ScC_2). The convex hull and atomic structure of several scandium carbides are presented in Fig. 4.3. While many of the scandium carbides are metals, Sc_4C_3 is an insulator, $Sc_{13}C_{10}$ is a superconductor, and Sc_2C is a topological electride [144, 145, 128]). It is noted that Sc_2C has a isomorphic structure with the M_2C M-X layer in hexagonal MXenes or MAX phases (for instance, Sc_2InC or Sc_2SnC the corresponding Sc_2CO_2 MXene of the new ground state with the hexagonal carbon plane broken into C_3 trimers is likely found. Indeed, carbon has the propensity to alter its structural unit to offer a variety of stable compounds, [146, 133]. Moreover, it has been found that the gapped compounds Sc_3C_4 and Sc_2C also have many isotypic compounds i.e., M_3C_4 (with M=Y, La, Lu, Tm, Ho [147, 148, 149]) and M_2C (with M = Y, La [138, 139, 140, 141, 142]). As similar to these isotypic compounds substituting scandium with other rare metals, it has been confirmed the isotypic MXene systems M_2CO_2 (with M=Y, La, Lu, Tm, Ho) can be obtained with the same C_3 structure as Sc_2CO_2.

4.2 Computational details

The electronic and vibrational properties of isotypic $C_3-M_2CO_2$ (M=Sc, Y, La, Lu, Tm, and Ho), as well as hex- and AFE-(antiferroelectric) Sc_2CO_2, were calculated using density functional theory (DFT). The kinetic energy cut-off was set to 520 eV for all systems, and Γ-centered $6 \times 6 \times 1$, $12 \times 6 \times 1$ and $12 \times 12 \times 1$ k-points grids were empolyed for $C_3 - M_2CO_2$, $AFE - Sc_2CO_2$ and $hex - Sc_2CO_2$. The length of the c axis of slab models was set to 15 Å for all structures to circumvent artificial interaction between their periodic images. All structures were optimized using the GGA-PBE functional [29] with force criteria of 0.001 eV/Å and the electronic structures of optimized structures were calculated using HSE06 hybrid functional [150].

Vibrational properties (dispersion and phonon density of states) of $C_3 - Sc_2CO_2$ and $hex - Sc_2CO_2$ were obtained with Phonopy package [75] and force constants were obtained with the finite displacement method using displaced $2\times2\times1$, $4\times4\times1$ and $4\times2\times1$ supercells for $C_3 - M_2CO_2$, $hex - Sc_2CO_2$ and $AFE - Sc_2CO_2$. The IR and Raman spectra of Sc_2CO_2 (*C2/m* and *P31m* phase) were extracted from the post-processing using VASP-infrared-intensity script [151] and VASP-ramanrc script [152]. The born effective charges and polarizability for the IR and Raman spectra were obtained with calculation routines of VASP package [153]. From first principles molecular dynamics results, the Dynaphopy package was used to evaluate the phonon density of states of $C_3-Sc_2CO_2$ and its $C_3-M_2CO_2$ isotypic compounds [154]. The time step of the molecular dynamics simulations was set to 3 fs using the standard Nose-Hoover thermostats [155, 156] of 300K and 3000 ionic steps for the extraction of phonon density of states via Fourier transformation of velocity auto-correlation function. A energy transformation path of Sc_2CO_2 from C_3 phase to hex and AFE phase were obtained with the solid-state NEB method implemented in atomic simulation environment [157] and the TSASE code [158, 159, 160] using 61 and 30 images on the path from C_3 phase connecting hex and AFE phase, respectively. The migration path of Li ion on $C_3 - Sc_2CO_2$ surface was obtained using the climbing-image nudge elastic (cNEB) method [161, 162] with the force criterion 0.015 eV/Å and 10 images on the path. The real space distribution of wavefunctions of C_3 trimer and $C_3 - Sc_2CO_2$ were extracted with VaspBandUnfolding code [163]. Atomic structures, partial charge densities, and wavefuncitons were illustrated with VESTA software [132].

4.3 Atomic structure of $C_3-M_2CO_2$

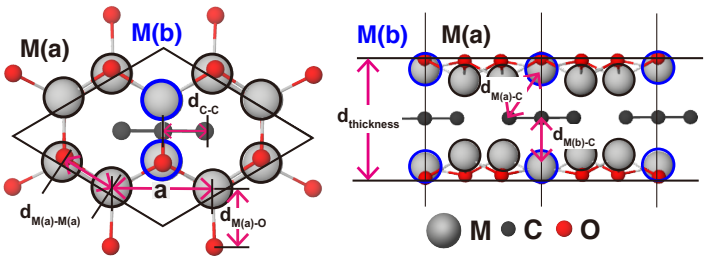

FIGURE 4.4: [From Fig. S1 of Publication II] (permitted by John Wiley & Sons) The structure of C_3-M_2CO_2 (M= Sc, Y, La, Lu, Tm, and Ho) structure (top view and side view) with lattice parameters.

System	XC functional	a	d_{C-C}	$d_{thickness}$	$d_{M(a)-M(a)}$	$d_{M(a)-O}$	$d_{M(a)-C}$	$d_{M(b)-C}$
Sc_2CO_2	PBE	3.23	1.34	4.82	3.60	2.04	2.63	2.26
Sc_2CO_2	SCAN	3.23	1.33	4.76	3.58	2.04	2.61	2.25
Sc_2CO_2	optB88	3.23	1.33	4.80	3.59	2.04	2.63	2.26
Sc_2CO_2	HSE06	3.20	1.32	4.79	3.59	2.03	2.61	2.25
Y_2CO_2	PBE	3.47	1.34	5.06	3.86	2.20	2.77	2.42
La_2CO_2	PBE	3.72	1.34	5.39	4.11	2.36	2.92	2.59
Lu_2CO_2	PBE	3.37	1.35	5.09	3.75	2.14	2.71	2.35
Tm_2CO_2	PBE	3.41	1.35	5.02	3.79	2.17	2.73	2.38
Ho_2CO_2	PBE	3.45	1.35	5.08	3.83	2.19	2.76	2.40

TABLE 4.1: [From Table. 1 of Publication II] (permitted by John Wiley & Sons) The lattice parameters of $C_3 - M_2CO_2$ (in Å) of figure 4.4 optimized with PBE [29] and HSE06 [150] exchange-correlation (XC) functional.

The previously reported hex $- Sc_2CO_2$ [15, 125, 122] and AFE $- Sc_2CO_2$ have trigonal and oblique structures which are highly symmetric in the 2D plane, the hex$-Sc_2CO_2$ is highly asymmetric in the direction perpendicular to the plane which yields a huge out-of-plane ferroelectricity. [125] The atomic structure and lattice parameters of $C_3-M_2CO_2$ are presented in Fig. 4.4 and Table 4.1. The $C_3-M_2CO_2$ structure contains a C_3 trimer at the core and arrange of oxygen terminations are centrosymmetric. This centrosymmetry yields zero polarization, which would stabilize the $C_3-M_2CO_2$ structure significantly compared to hex-M_2CO_2 [164, 165]. The bond length of the C_3 unit between carbon atoms in $C_3-M_2CO_2$ structures is about 1.34 Å, which is close to the typical bond length of carbon double bonds C = C [146]. The double bond character of C_3 trimer in $C_3-M_2CO_2$ is intimately correlated with their electronic properties, behaving as electrides. The chemical mechanism of electride formation with the M_2CO_2 structure is discussed in the following sections.

4.4 Energy profile of transformation path of hex- and AFE-Sc_2CO_2 → C_3-Sc_2CO_2

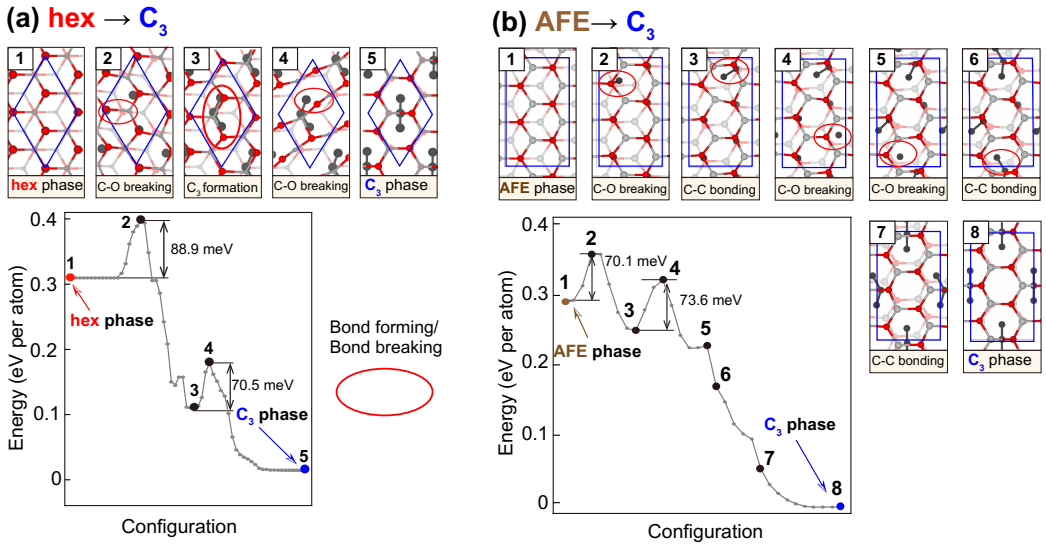

FIGURE 4.5: [From Fig. 2 of Publication II] (permitted by John Wiley & Sons) Adiabatic potential energy surface for transformation for (a) hex → C_3 and (b) AFE → C_3 of Sc_2CO_2 calculated by solid state NEB (ssNEB). The atomic structure of the snapshot of each step is illustrated and barrier heights are denoted in meV. In the snapshots, the blue line delineates the boundary cell, and the red line illustrates the bond forming or breaking between atoms.

Fig. 4.5 presents the energy path along the structural transformation of Sc_2CO_2 from hex to C_3 phase and from AFE to C_3 phase, obtained with the solid state NEB calculation [158, 159, 160]. Both transformation paths shown in Figures 4.5 (a) and (b). The low transformation barriers of around 70 meV is attributed to the breaking of $C-O$ bondings marked in the Fig. 4.5. The further energy stabilizations are induced by displacement of oxygen atoms in order to preserve the centrosymmetry of the C_3 phase that derives zero polarization of $C_3-Sc_2CO_2$. The transformation barrier presented here is comparable to the barriers of transformation from 1T' to 2H of TMDCs (transition metal dichalcogenides) typically in range of 0.4 eV$\sim$ 0.8 eV per formula unit [166, 167, 168]. This suggests that phase engineering between $C_3 - Sc_2CO_2$ and hex $- Sc_2CO_2$ orAFE $- Sc_2CO_2$ phases can be realistic.

4.5 Electronic structure of C_3-M_2CO_2 electrides

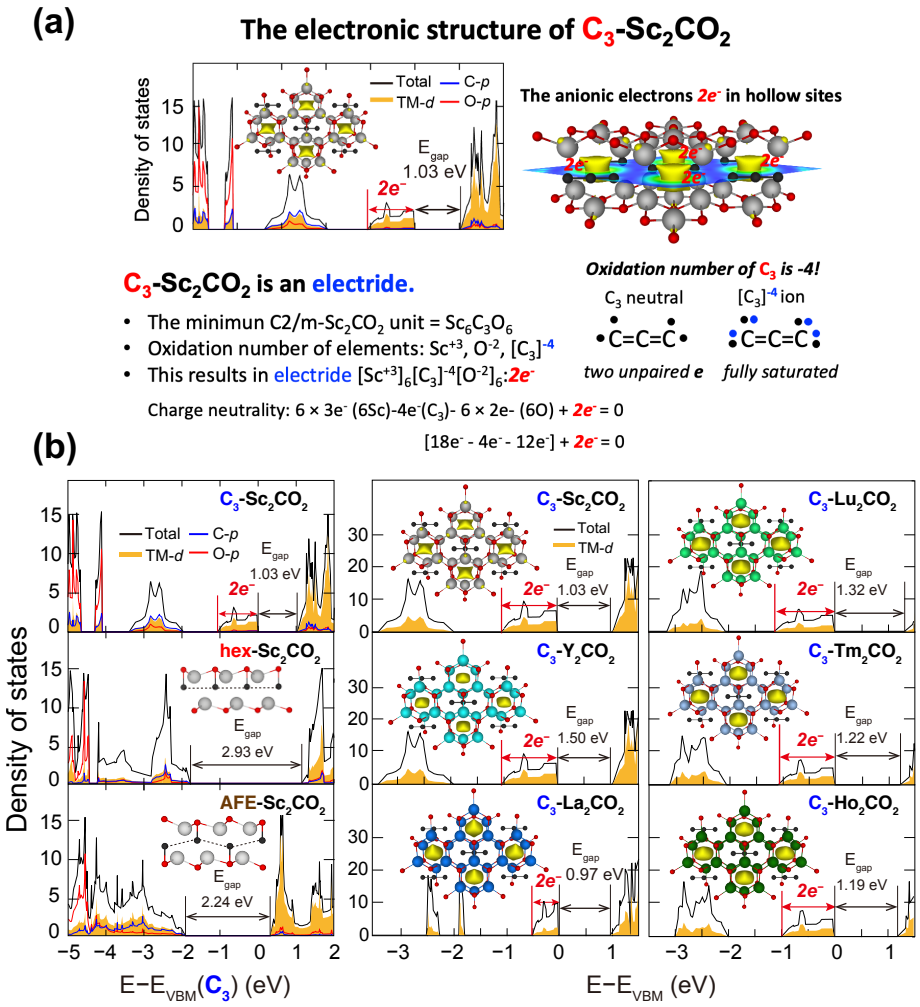

FIGURE 4.6: (a) A schematic illustration and interpretation of the oxidation numbers and electronic structure of Sc_2CO_2 when it behaves as an electride with anionic two electrons.(b) [From Fig. 3 of Publication II] (permitted by John Wiley & Sons) Density of C3 M_2CO_2 (M = Sc, Y, La, Lu, Tm, and Ho) states and Sc_2CO_2 in hex and AFE phases, as well as partial charge density of in-gap states. The band gap resulting from the Fermi energy is denoted by arrows.The zero of energy is set to the valance band maximum (VBM) of $C_3 - M_2CO_2$. The isosurface of the partial charge density plots are set to $0.01e/\text{bohr}^3$.

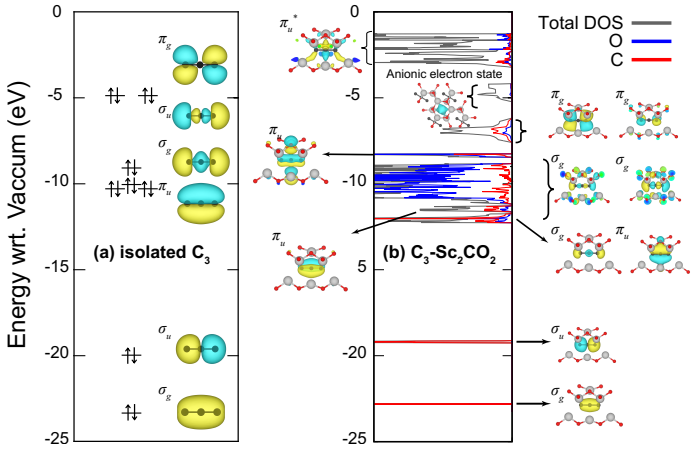

FIGURE 4.7: [From Fig. S6 of Publication II] (permitted by John Wiley & Sons) Molecular orbital diagrams of C_3 originated states. (a) The isolated C_3 trimer and (b) C_3 originated states in $C_3 - Sc_2CO_2$.

The electronic structure of $C_3 - Sc_2CO_2$ and $C_3 - M_2CO_2$ isotypic structures with Sc_2CO_2 in hex and AFE phases are shown in Figure 4.6. The zero point of the energy axis is set to the VBM (valence band maximum) of $C_3 - M_2CO_2$. $hex - Sc_2CO_2$ and $AFE - Sc_2CO_2$ show similar electronic structure in the conduction and valence bands compared to typical MXenes (cf. chapter 3). In contrast to the conventional MXenes, $C_3 - Sc_2CO_2$ and its isotypic structures ($C_3 - M_2CO_2$, M = Y, La, Lu, Tm, and Ho) have characteristic valence band states delivered from a narrow detached band from the valence continuum of states about 1 eV, in contrast to conventional MXenes.

This detached valence state corresponds to two electrons for the $Sc_6C_3O_6$ unit that are trapped at quasi 0D hollows in-between the C_3 units, as shown in the Figure 4.6. By assigning the typical oxidation numbers to the $Sc_6C_3O_6$ unit, the electride behavior of $C_3 - M_2CO_2$ can be figured out; giving M^{III}, O^{-II}, and C_3^{-IV} [169] (assuming C=C double bond), we would write the system with a chemical formula $M_6^{III}[C_3]^{-IV}O_6^{-II}{:}2e^-$, or $[M_6C_3O_6]^{+II}{:}2e^-$, indicating that the two extra electrons are behaving as an anion of electrides [149, 170, 171, 172, 173, 174, 175]. To summarize, a violation of the Octet rule inM_2CO_2 (M= Sc, Y, La, Lu, Tm, and Ho) results in an electride in which the part of $[M_6C_3O_6]^{+II}$ is stabilized by forming a C_3 trimer and trapping $2e^-$ at its hollow space.

The C_3 trimer has a strong bonding character in the electronic structures of C_3-M_2CO_2. The electronic states of the C_3 trimer and their related states in C_3-M_2CO_2 are extracted and visualized in Fig. 4.7. The isolated C_3 trimer and C_3-Sc_2CO_2 are calculated with the HSE06 functional [150]. VaspBandUnfolding code [163] was employed to extract wavefunctions of the C_3 trimer and C_3-Sc_2CO_2. Based on the obatined results, the molecular orbital (MO) diagram of the isolated C_3 and the density of states of C_3-Sc_2CO_2 are presented with several

C_3 related states in figure 4.7. This results show that carbons strongly interacts with neighboring carbons in the C_3 trimer and create relatively weak bonding between surrounding oxygen and transition metal atoms. It is noted that doubly degenerated π_g states in C_3-Sc_2CO_2 are fully occupied, which corresponds to the anionic electride states of two electrons. This again supports the fact that the oxidation state of the C_3 trimer in C_3-M_2CO_2 is -IV.

4.6 Ionization mechanism of C_3-M_2CO_2 electrides

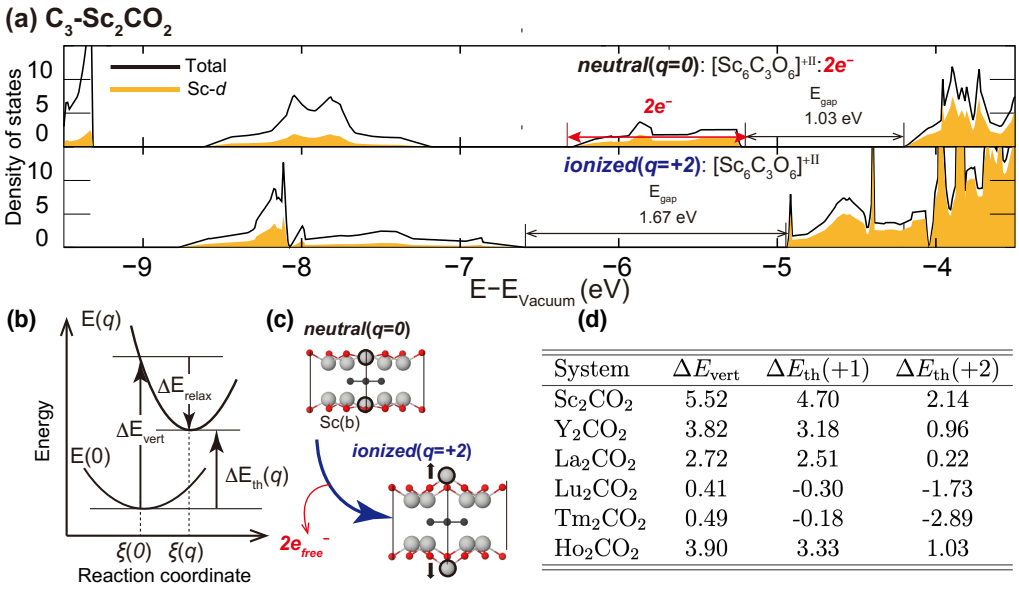

System	ΔE_{vert}	$\Delta E_{\mathrm{th}}(+1)$	$\Delta E_{\mathrm{th}}(+2)$
Sc_2CO_2	5.52	4.70	2.14
Y_2CO_2	3.82	3.18	0.96
La_2CO_2	2.72	2.51	0.22
Lu_2CO_2	0.41	-0.30	-1.73
Tm_2CO_2	0.49	-0.18	-2.89
Ho_2CO_2	3.90	3.33	1.03

FIGURE 4.8: [From Fig. 4 and Table 1 of Publication II] (permitted by John Wiley & Sons) The ionization of $C_3 - Sc_2CO_2$. (a) Density of states of $C_3 - Sc_2CO_2$ in charge the neutral state and ionized state ($q = +2$) . The zero of the energy axis is set to the vacuum level. (b) A schematic of the vertical and thermal ionization of $C_3 - Sc_2CO_2$. The vertical, thermal ionization energy and relaxation energy are denoted as ΔE_{vert}, ΔE_{th} and $\Delta E_{\mathrm{relax}}$, respectively. (c) The structure deformation of $C_3 - Sc_2CO_2$ accompanied with double ionization ($q = +2$). (d) The vertical and thermal ionization energy of $C_3 - M_2CO_2$. ΔE_{vert} is the vertical ionization energy and $\Delta E_{\mathrm{th}}(q)$ is the thermal ionization energy with $q = +1, +2$ for the single and double ionization process. Here the thermal ionization energy for the double ionization process defines the work function.

The anionic electrons in an electride are typically loosely bound, therefore they are expected to be easily ionized. [171, 172, 173, 174, 175]. For instance, such reactivity for the electride $[12CaO \cdot 7Al_2O_3]^{+IV}{:}4e^-$ is evidenced by a work function as low as 2.4 eV, accompanied with high electron field emission efficiency, as previously reported by Toda *et al.* [171, 172].

To investigate the mechanism of ionization of $C_3 - M_2CO_2$ ($[M_6C_3O_6]^{+II}{:}2e-$), doubly ionized ($q = +2$) $C_3{-}M_2CO_2$ are calculated. The vertical ionization energies ΔE_{vert} were evaluated with the eigenvalue (weighted average over 1st Brillouin zone) of the detached valence band (vertical ionizaiton) [176, 177, 178, 88] and the thermal ionization energies $\Delta E_{\text{th}}(q)$ were estimated as

$$\Delta E_{\text{th}}(q) = \Delta E_{\text{vert}} - \Delta E_{\text{relax}}(q)/q. \tag{4.1}$$

Here, $q = +1$ and $q = +2$ represent the single and double ionization processes. In the results, thermal ionization energies of double ionization $\Delta E_{\text{th}}(+2)$ are relateively lower than the vertical and single ionization energy ΔE_{vert} and $\Delta E_{\text{th}}(+1)$ because structure relaxation energy of the double ionization are large accompanied with large ($\sim$ 6 eV per formula unit). The structure deformation involved from the $q = 0 \rightarrow q = +2$ ionization process as illustrated in Figure 4.8 (b) and (c). As two electrons are removed, the transition metal atoms at the center of the structure are shifted outward. Interestingly, it is preferable to empty the detached valence band at once ($q = +2$), rather than the half-filled state ($q = +1$), therefore the systems exhibits a 'negative U' behavior.

The double ionization energies of $C_3{-}M_2CO_2$ are lower than the measured work function of $[Ca_{24}Al_{28}O_{64}]^{+IV}{:}4e^-$ (2.4 eV). [171] Meanwhile, the thermal ionization energies are negative for Lu_2CO_2 and Tm_2CO_2, which indicates that these systems are not electronically stable even in their charge neutral state. The other systems exhibit low thermal ionization energies ($\sim$ 2 eV or less), which suggests that these systems would be good candidates for thermal field emission materials.

4.7 Vibrational properties of C_3-M_2CO_2

4.7.1 Harmonic phonon dispersion and dynamical stability

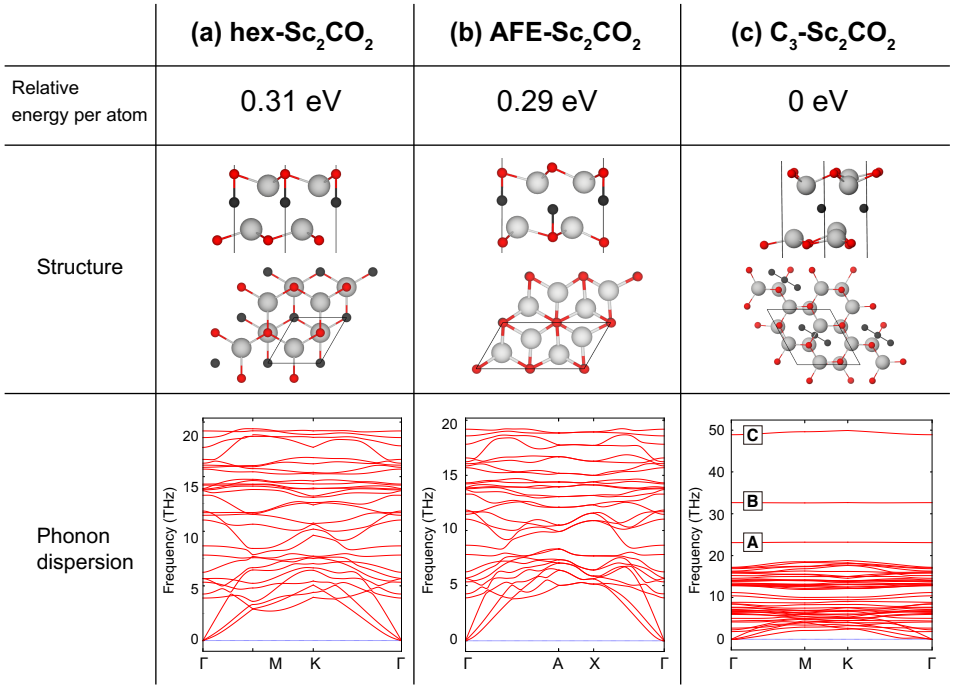

FIGURE 4.9: [From Fig. S4 of Publication II] (permitted by John Wiley & Sons) The phonon dispersion of (a) hex-Sc_2CO_2, (b) AFE-Sc_2CO_2 and (c) $C_3 - Sc_2CO_2$ is dynamically stable in hex, AFE and C_3 phase.

To verify dynamical stability of hex-, AFE-, and C_3–Sc_2CO_2, phonon dispersions are presented in Fig. 4.9. The phonon dispersions show that the three phases of Sc_2CO_2 are dynamically stable. In contrast to hex- and AFE-Sc_2CO_2, specific carbon vibrations in a high frequency range (from 20 THz to 50 THz) are observed for C_3–Sc_2CO_2, which are labeled with A, B, and C in 4.9. The specific carbon vibrations reflect the C_3 trimer formation.

4.7.2 Phonon density of states and IR and Raman activities

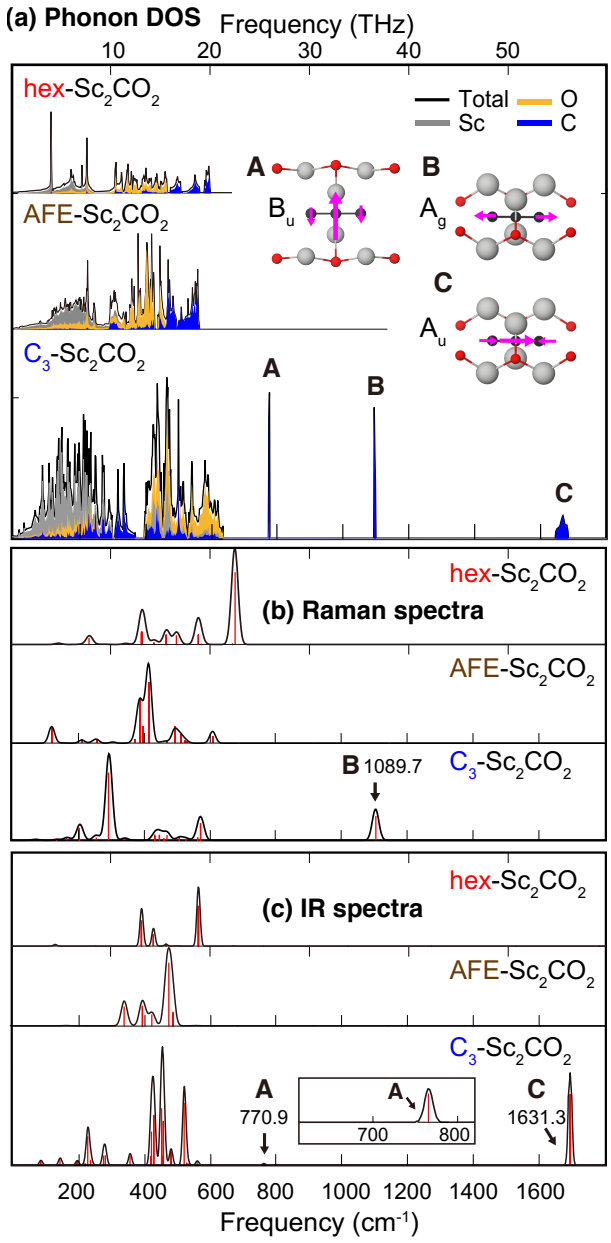

FIGURE 4.10: [From Fig. 6 of Publication II] (permitted by John Wiley & Sons) Calculated IR and Raman sepctra of hex, AFE and C_3 phase of Sc_2CO_2 and displacement patterns of the typical vibrations of the C_3 unit. (a) Three localized carbon vibrations A, B, and C with their frequency, symmetry label and activities of IR and Raman spectra. The mode B is Raman active, and modes A and C are IR active. Calculated (b) IR intensity and (c) Raman intensity of hex, AFE and C_3 phase of Sc_2CO_2.

We now turn our attention to vibrational spectra (IR and Raman) for experimental verification. The phonon DOS and calculated vibrational spectra of Sc_2CO_2 in hex, AFE and C_3 phases are shown in Figure 4.10. As mentioned above, $C_3 - Sc_2CO_2$ exhibits three localized carbon vibrations in a high frequency range (700 cm^{-1} ~1700 cm^{-1}). From the atomic displacements of these three modes, the modes are attributed to mode-A: B_u, (bending), mode-B: A_g (symmetric stretching), and mode-C: A_u (asymmetric bending).]

The symmetry symbols of three carbon vibrations belong to the point group $2/m(C_{2h})$, which results in modes-A (B_u) and mode-C (A_u) being IR active (Raman inactive) and mode-B (A_g) being IR active (Raman inactive).In the calculated IR and Raman spectra (cf. Figure 4.10 (b)), the mode-B and mode-C show strong signal IR and Raman spectra, which are expected to be confirmed by experiment.

4.7.3 Molecular vibrations of the isolated C_3 and embedded C_3 in C_3-Sc_2CO_2

TABLE 4.2: [From Table 2 of Publication II] (permitted by John Wiley & Sons) The C-C bond length (in Å) and vibration modes with frequencies (in cm^{-1}) of three localized carbon vibrations for the isolated C_3 trimer (C_3 and C_3^{-IV}) and $C_3 - M_2CO_2$.

		exp. [179]	MRCI [180]	This work		
		C_3	C_3	C_3	C_3^{-IV}	$C_3 - Sc_2CO_2$
	C-C bond length (Å)	–	1.28	1.29	1.32	1.32
A	Bending, B_u (cm^{-1})	63.4	52	20.5	414.1	770.9
B	Sym. stretch., A_g (cm^{-1})	1226.6	1293	1240.0	1144.7	1089.7
C	Asym. stretch., A_u (cm^{-1})	2040.0	2217	2147.6	1527.5	1631.3

The carbon vibrations in the high frequency regime of $C_3 - Sc_2CO_2$ are originated from the carbon bonding of C_3 trimer. The vibration frequencies of C_3 vibrations evaluated by density functional theory with HSE06 functional and the values from experiment [179] are summarized in Table 4.2, confirming excellent agreement between the calculated values in this work and the values from experiment and a previous quantum chemical calculation [180].The C_3 unit in $C_3 - Sc_2CO_2$ is more like C_3^{-IV} than the neutral C_3, according to Table 4.2. Remarkably, the frequency of the bending motion of $C_3 - Sc_2CO_2$ is much higher (770.9 cm^{-1}) than that of neutral C_3 (63.4 cm^{-1}).When four electrons are added toC_3, the C-C bond length changes from 1.29 Å to 1.32 Å, which is also observed in $C_3 - Sc_2CO_2$. This indeed supports that the formal oxidation number of C_3 is -IV where the C3 trimer extracts four electrons from surrounding atoms; therefore, the chemical formula $M_6^{III}[C_3]^{-IV}O_6^{-II}$:$2e^-$ holds.

4.7.4 Molecular dynamics of M_2CO_2 in 300K

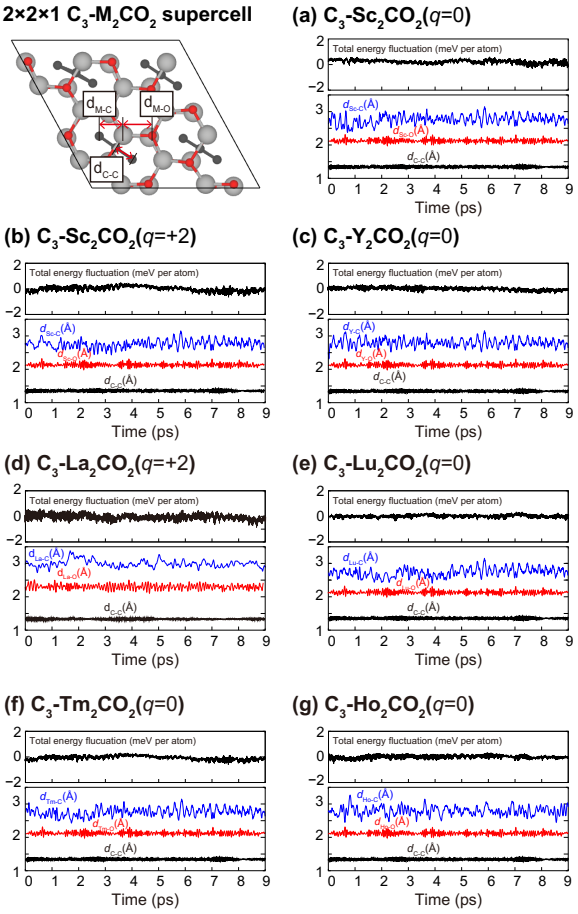

FIGURE 4.11: [From Fig. S4 of Publication II] (permitted by John Wiley & Sons) Time variation of total energy fluctuations (per atom in meV) and bond lengths (d_{M-C}, d_{M-O}, and d_{C-C} in Å) of $C_3 - M_2CO_2$ (M=Sc, Y, La, Lu, Tm, and Ho) in MD simulations at room temperature (300K).

The dynamical stability of C_3-M_2CO_2 (M=Sc, Y, La, Lu, Tm,and Ho) were verified with *Ab initio* molecular dynamics (MD) simulations at room temperature (300K) within a Nosé-Hoover thermostat [181, 182]. The $2\times2\times1$ supercell C_3-M_2CO_2 were empolyed and and the trajectories were integrated untill 9 ps (3000 steps) with the time step 3 fs. For Sc-M_2CO_2, both neutral (q=0) and ionized (q=+2) states were calculated. Results of MD simulations presenting the time variation of energy fluctuation (per atom in meV) and the bond lengths i.e., d_{M-C}, d_{M-O}, and d_{C-C} shown in the Fig. 4.11. The energy fluctuation of all systems were less than 1 meV/atom that ensures the thermal stability of $C_3-M_2CO_2$. The thermal stability is also evidenced by the fact that the bond lengths are oscillating around their average values for all C_3-M_2CO_2 (q=0) and ionized Sc-M_2CO_2 (q=+2).

4.8 $C_3-Sc_2CO_2$ as an anode material of litihum-ion battery

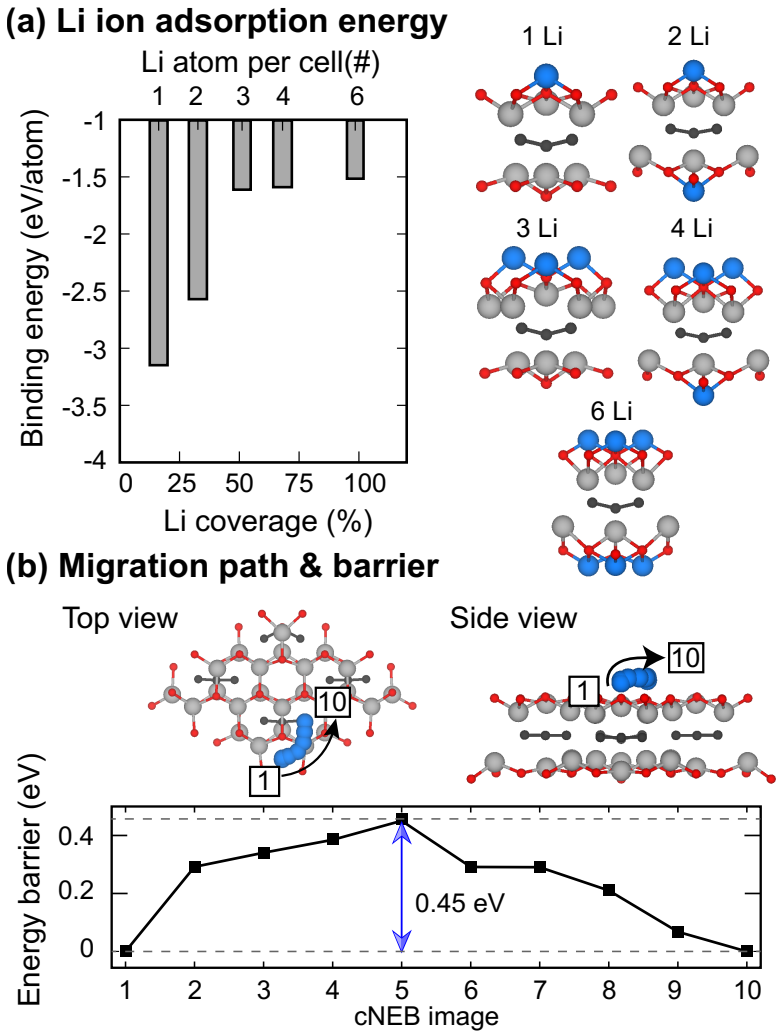

FIGURE 4.12: [From Fig. 5 of Publication II] (permitted by John Wiley & Sons) (a) The binding energy of Li atoms as a function of Li concentration. (b) Top and side views of the lowest energy diffusion path of Li in $C_3 - Sc_2CO_2$. (c) Energy profiles for Li diffusion between adjacent favorable adsorption site on $C_3 - Sc_2CO_2$.

While applicability of MXenes for the Li-ion battery have been intensively investigated [183, 79, 184, 185]. Aierken *et al.* reported that hex $-$ Sc_2CO_2 is highly unstable with Li atom adsorption [184], which may reflect the intrinsic instability of hex-Sc_2CO_2. The calculated results show that $C_3 - Sc_2CO_2$ ($[Sc_6C_3O_6]^{+II}$:$2e^-$) is highly stable upon Li adsorption even with 100% Li coverage. The binding energies of Li atom on $C_3 - Sc_2CO_2$ were estimated as

$$E_b = \frac{1}{x}\left[E(Sc_6C_3O_6 : xLi) - E(Sc_6C_3O_6) - xE(Li; bulk)\right] , \qquad (4.2)$$

where $E(Sc_6C_3O_6 : xLi)$ and $E(Sc_6C_3O_6)$ are the total energy of $C_3 - Sc_2CO_2$ with and without xLi atoms on the surface, E(Li;bulk) is total energy of single Li atom of bulk bcc phase. The relaxed structures of $C_3 - Sc_2CO_2$ with various Li coverage and the binding energies are summarized in Fig. 4.12 (a). The Li binding energies are negative and sufficiently large at overall concentrations, which can be comparable to other MXenes (for instance, E_b is 3.57 eV of V_2CO_2) [183, 79, 184]. Li migration barrier on $C_3 - Sc_2CO_2$ was calculated by the cNEB (nudged elastic band with climbing images)[161] method; the calculated value of 0.45 eV is comparable to that of graphite[186, 185]. Therefore, it is expected that C_3–Sc_2CO_2 can be used as an anode material in Li-ion batteries.

4.9 Chapter summary

In this work, discovery of a family of 2D MXene electride materials M_2CO_2 (M=Sc, Y, La, Lu, Tm, and Ho) was presented. The discovered structure is derived from the trigonal MXene phase of Sc_2CO_2 through the formation of C_3 trimer, which imposes centrosymmetry that eliminates electric polarization and enhance thermostability of M_2CO_2. The C_3 formation observed in this work occurs in a $\sqrt{3} \times \sqrt{3}$ commensurate unit of the primitive hexagonal MXene. This shows that discovery of new structures in material science would involve more larger commensurate units that are usually not considered in primary studies of material search.

The chemical formula for the electride phase is expressed by $[M_6C_3O_6]^{+II}$:$2e-$, where two electrons are adhered at the voids between the two trimers, behaving as anions.Low ionization energies of $\sim$ 2 eV or less per electron for the removal were estimated for C_3–M_2CO_2. It was also demonstrated that Sc_2CO_2 binds Li atoms with low migration barriers and can thus be used as an anode material in a Li-ion battery. Due to their very low ionization energies, these materials might be applied as cold electron emitters, charge storage, and catalysis.

Chapter 5

Strain engineering of hole carriers in p-type haeckelite GaN

This chapter overviews **Publication-3:** Strain engineering to release trapped hole carriers in p-type haeckelite GaN, **Soungmin Bae** *et al.*, ACS applied electronic materials (accepted November 8th, 2021).

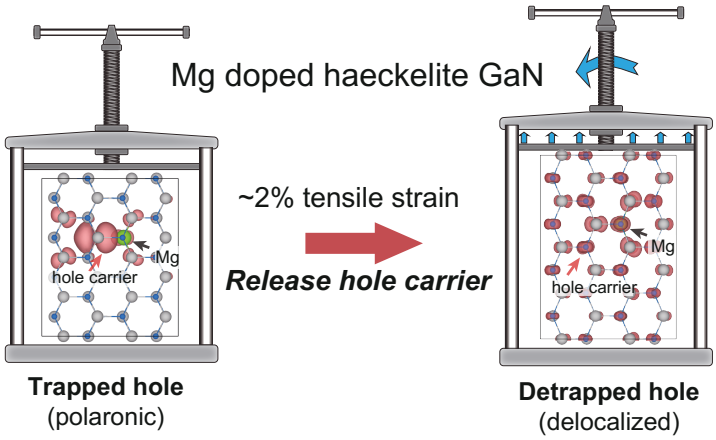

The gallium nitride haeckelite (4|8-GaN) phase is an attractive material for two-dimensional (2D) light-emitting diodes (LED), but its p-type doping is challenging due to hole carrier trapping. In this work, strain engineering as a route to release trapped hole carriers of Mg doped 4|8-GaN is presented based on *ab inito* calculation using density-functional theory. It has been shown that Mg and Be impurities in 4|8-GaN exhibit multifarious hole states, including localized (trapped) and delocalized (extended) states. While Mg and Be impurities prefer trapped hole states, the trapped hole state of Mg impurity is shown to be spontaneously detrapped with a moderate tensile strain of around 2% perpendicular to the basal plane. This chapter suggest a concept of strain engineering to enhance carrier dopability of atomically thin two-dimensional materials.

5.1 Research backgroud

III-V semiconductors composed of elements group III and V of the periodic table are fundamental materials for many optoelectronics and power devices [187, 188, 189, 190]. In particular, gallium nitride (GaN) had a huge influence on human society through the realization of blue light-emitting diodes (LED) [35, 36, 191, 192, 193]. Despite remaining drawbacks such as low hole concentration [194, 195, 196, 197, 198, 37], GaN is an irreplaceable key material for blue LEDs owing to its direct band gap.

The bulk-GaN ground state is wurtzite phase (w-GaN), which has a large built-in polarization in the $[000\bar{1}]$ direction, which reduces the light-emitting efficiency of GaN blue LEDs [30, 199, 200, 201, 202]. While several non-polar phases of GaN were examined to overcome such obstacles [203, 30, 28, 204, 205, 206, 207, 208], haeckelite GaN (4|8-GaN) has emerged as a promising candidate for optoelectronics applications. When the material is atomically thin (2∼47 GaN atomic layers), 4|8-GaN is non-polar and acts as the thermal ground state phase [28, 205]. Furthermore, 4|8-GaN is known to be fabricated using epitaxial growth on a graphene buffer layer under strain free conditions [209, 210, 211, 212, 170].

It has long been known that the hole dopability (hole carrier concentration contributing to the conductivity) of p-type GaN is typically low, which significantly degrades the efficient operation of GaN based blue LED [35, 36, 195, 37]. Mg is dominantly doped into GaN for p-type doping, however the hole carriers in GaN are shown to be trapped in localized polaronic states [38, 32, 39, 40, 41]. Moreover, Mg acceptors can exhibit a *bistability*, i.e., the hole states have both trapped (polaronic) and extended (delocalized) states, with the polaronic states lower in energy by $\sim$ 30 meV [34, 32, 213, 214, 215, 216, 217]. On the other hand, a strain control of the trapping and detrapping of hole carriers was demonstrated for transition metal (TM) doped in w-GaN, which can switch on and off the carrier mediated magnetism between the TM impurities [34, 217]. This implies that a strain control of 4|8-GaN would control the hole states between trapped and detrapped state and provides a practical route to acquire sufficient hole carrier mobility and concentration for optoelectronic applications.

5.2 Purpose of this work

In this chapter, the quantum details of the hole states induced by Mg and Be impurities doped in 4|8-GaN were explored using self-interaction corrected density-functional calculations. The results show that Mg and Be impurities have a variety of hole states in 4|8-GaN, including the polaronic (trapped) ground state and the metastable delocalized (extended) state. While Mg and Be impurity hole carriers prefer trapped states as their ground state over metastable delocalized hole states, a strain control was examined to de-trap the trapped hole carrier by applying a moderate tensile strain to 4|8-GaN. The photoluminescence spectra of polaronic hole states of Mg impurity 4|8-GaN were calculated with various lattice strains, which can be a spectroscopical indicator of the degree of lattice strain. This work presents a simple strategy of strain control for efficient p-type doping and ideal light-emitting operation of 48-GaN-based blue LEDs for optoelectronics and nanophotonics, and therefore sheds some light on strain engineering of atomically thin two-dimensional materials.

5.3 Computational details

All calculations were performed using density functional theory (DFT) as implemented in the VASP package [71, 70, 72, 73]. The projector-augmented plane wave (PAW) method and the GGA-PBE functional [29] were employed. The HSE parameters $\alpha = 0.32, \omega = 0.20$ Å were employed for the band structure calculation of primitive GaN, which were previously validated for the electronic structure of wurtzite GaN [106, 218]. The plane-wave cutoff is 350 eV and Γ-centered $8 \times 8 \times 11$ and $11 \times 11 \times 8$ k-meshes [219] were used for k-point sampling of 4|8-GaN and w-GaN. The optimized lattice constants of 4|8-GaN are x= 5.53 Å and z= 5.25 Å. The band gaps of 3.36 eV (4|8-GaN) and 3.35 eV (w-GaN) obtained by HSE functional were used to account for the zero-phonon line (ZPL) energy of the Mg acceptor in 4|8-GaN. The Mg and Be substitutional impurities at the Ga site in 4|8-GaN are modeled with a $2 \times 2 \times 4$ supercell of the primitive 4|8-GaN including 128 atoms and a $4 \times 4 \times 4$ Monkhorst-Pack k-mesh was used for the supercell calculations. The total energy of negatively charged impurites in the periodic boundary condition were corrected by SCPC correction [220]. The dielectric constant of 4|8-GaN for the SCPC correction was set to 7.0 as obtained by DFT calculation based on density functional perturbation theory (DFPT) [221].

5.4 Primitive band structure of w-GaN and 4|8-GaN

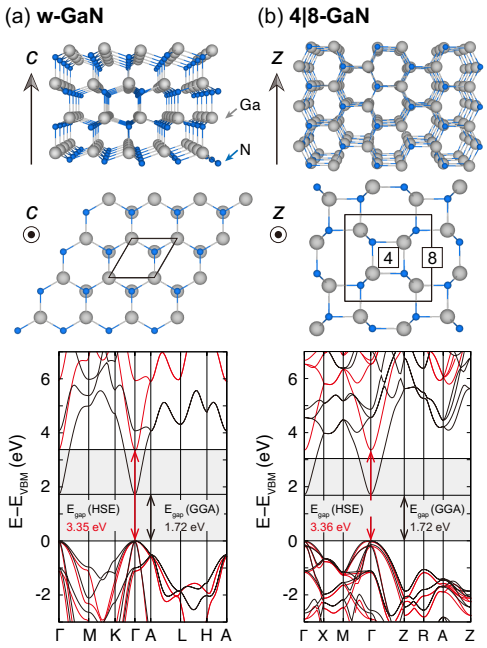

FIGURE 5.1: [From Fig. 1 of Publication III] Atomic structure and band structures of w-GaN (left) and 4|8-GaN (right). The band structure of w-GaN and 4|8-GaN were obtained by GGA-PBE and HSE functionals.

The primitive atomic and electronic structures of w-GaN and 4|8-GaN obtained by first principles calculations based on density-functional theory are shown in Figure 5.1. The atomic structures of pristine w-GaN and 4|8-GaN were optimized with PBE-GGA [29] functional and the band structures are calculated with PBE-GGA and HSE [150] functionals ($\alpha = 0.3$ and $\omega = 0.2$). Whereas w-GaN exhibits a built-in electric field along the c axis induced by strong polarity of $[000\bar{1}]$ surface, 4|8-GaN has rigorous zero polarization along the z axis which significantly stabilizes the 4|8-GaN phase compared to w-GaN with few-atom thickness (from 2 to 47 monolayers) [28, 205]. While PBE-GGA gravely underestimates the band gap of GaN, the band gap of w-GaN obtained with HSE functional is in good agreement with the experimental value (3.4 eV) [216], therefore the estimation of the direct band gap of 3.36 eV of 4|8-GaN predicted by HSE functional might be reliable. The direct band gap 4|8-GaN at Γ point implies that 4|8-GaN also exhibits a high radiative recombination rate of 4|8-GaN similar to w-GaN. Apart from the trivial band gap underestimation by GGA-PBE for w-GaN and 4|8-GaN, the band dispersions are very similar to those obtained by HSE functional, which verifies the reliability of the PBE-GGA functional for band dispersion and valence band hole doping properties.

5.5 Hole states induced by Mg and Be impurities in 4|8-GaN

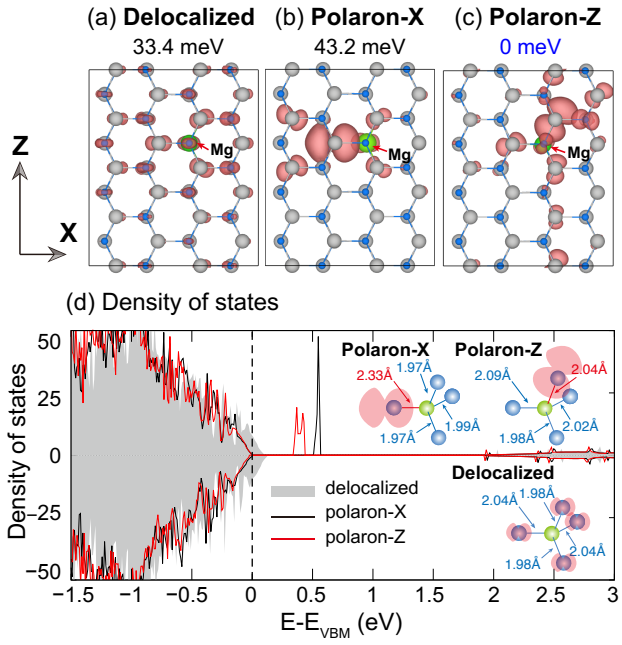

FIGURE 5.2: [From Fig. 2 of Publication III] Polaronic and delocalized hole states of Mg acceptor in 4|8-GaN and their densities of states and atomic structures. Three different hole states are shown: (a) delocalized state, (b) polaron in plane (Polaron-X) and (c) polaron along z direction (Polaron-Z). The iso-surface of partial charge density plots is set to 0.002 e/bohr^3. (d) The density of states and bond lengths between Mg acceptor and its first nearest neighbor nitrogen atoms are presented.

TABLE 5.1: Relative energies (E_{relative}) and acceptor transition levels [$\epsilon(0/-)$] of Mg and Be acceptors in 4|8-GaN calculated for polaron-X, polaron-Z and delocalized hole states.

	polaron-X (eV)	polaron-Z	delocalized
Mg acceptor			
E_{relative} (meV)	43.2	0	33.4
$\epsilon(0/-)$ (eV)	0.66	0.59	0.20
Be acceptor			
$E_{relative}$ (meV)	0	36.2	263.3
$\epsilon(0/-)$ (eV)	1.23	2.04	0.17

The atomic structures of localized hole states bound to magnesium (Mg) and beryllium (Be) impurities in 4|8-GaN were first calculated to explore the possible source of p-type doping in 4|8-GaN. Isolated Mg and Be impurities were embedded in a $2 \times 2 \times 4$ supercell of 4|8-GaN (11.06 Å$\times$ 11.06 Å$\times$ 12.9 Å, 128 atoms). To correct spurious delocalization bias of PBE-GGA functional [87, 88, 48], we employed a self-interaction correction using a hole state potential $V_{hs} = \lambda_{hs}(1 - n_{m,\sigma}/n_{host})$ applied on nitrogen p states [215, 88]. Here $n_{m,\sigma}$ denotes the partial occupation of spin orbital mσ and n_{host} denotes the reference occupancy of the defect-free host system. The strength parameter λ is uniquely determined as $\lambda_{hs} = 3.0$ eV when satisfying the generalized Koopmans condition for the localized in-gap state of Mg and Be impurities in 4|8-GaN.

From the results of self-interaction corrected calculations, multiple hole states including two polaronic states (polaron-X and polaron-Z) and one delocalized state were found. There spatial distribution are down Mg impurity in Fig. 5.2 (a), (b), and (c). It is noted that the polaron-X and polaron-Z hole states configurations are the ground states of Mg and Be impurities. The delocalized states behave as shallow acceptors without in-gap states, and the hole state charge distribution is delocalized over many atoms in contrast to the polaron-X and polaron-Z states. The two polaronic states (polaron-X and polaron-Z) induce deep in-gap states which behave as a deep acceptor. Their hole charge distribution are primary localized at a single nitrogen atom as small polarons accompanied by significant elongation of a single Mg-N or Be-N bond (cf. inset of Fig. 5.2 (d)).

The relative energies and acceptor transition levels of Mg and Be impurities are presented in Table 5.1. The optical transition levels (acceptor transition level) of Mg and Be impurities between $q = 0$ and $q = -1$ charge states were estimated as

$$\epsilon(0/-) = E(q = -1; q = 0) - E(q = 0), \tag{5.1}$$

where $E(q = 0)$ is the total energy for the charge state $q = 0$ and $E(q = -1; q = 0)$ refers to charge state $q = -1$ in the geometry of $q = 0$. The total energy difference between the delocalized state and polaronic ground state (trapped state) of Mg and Be impurities were 33.4 meV and 263.2 meV. This implies that Mg doping is much preferable to Be doping for practical p-type doping of 4|8-GaN.

5.6 Strain control of hole states for efficient p-type doping of 4|8-GaN

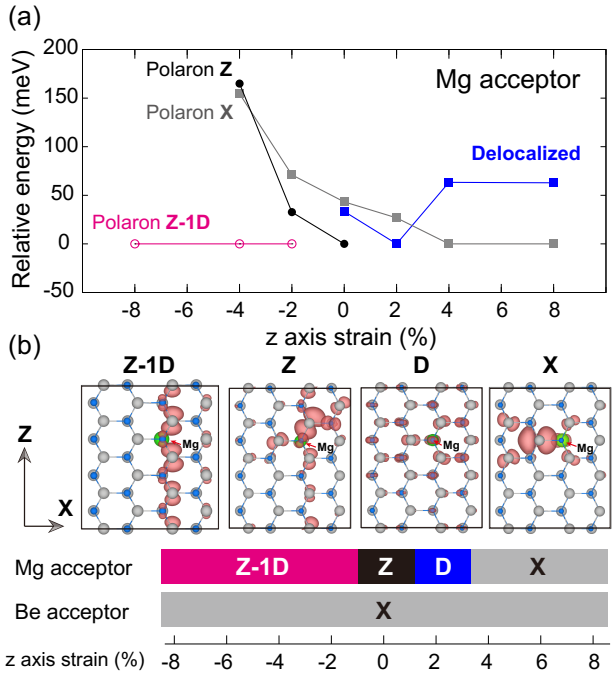

FIGURE 5.3: [From Fig. 3 of Publication III] Relative stability of multifarious hole states of Mg acceptor in 4|8 GaN under axial strain. (a) Relative energies of hole states with various strain of $-8\% \sim 8\%$ applied along z axis. (b) The partial charge density of three polaron states (Z-1D, Z and X) and delocalized state (d) and the ground state phase with respect to the c axis strain.

For ideal p-type doping, it is desirable that the extended (delocalized and mobile) states are the thermal ground state compared compared to the trapped (immobile) states. By the fact that small polarons are intimately influenced by the local bonding structure near by the impurities [33, 34, 87], it is expected that the muptiple hole states (polaron-X, polaron-Z and delocalized) of Mg and Be impurity in 4|8-GaN can be controlled by applying lattice strain. To verify this strain engineering concept, lattice strain is applied along z axis to 4|8-GaN.

Fig. 5.3 (a) depicts the relative energies and hole distributions of Mg impurity in 4|8-GaN under axial strain. It has been found that the ground state of Mg impurity is switched from polaron-Z-1D $\rightarrow$ polaron-Z $\rightarrow$ delocalized $\rightarrow$ polaron-X when the axial along z axis tensile is changed in the range of -8% $\sim$ 8%. It is noted that a new quasi-1D state called polaron-Z-1D appears under compressive strain, which reflects the change of local structure around the Mg impurity. In particular, the delocalized state is the thermal ground state at 2% tensile strain, this indicates that spontaneous detrapping of the hole carrier may occur with a moderate tensile strain. However, the polaron-X state for Be doping always remains as the ground state under the entire range of lattice

strain, which indicates that Be doping is not promising for p-type doping of 4|8-GaN.

In practical fabrication conditions, GaN layers are deposited on a solid substrate with a large lattice constant mismatch (∼17% in case of quartz) [195, 196, 197]. The strong lattice strain exerted on GaN layers usually degrades the blue LED performance. To reduce the lattice strain, epitaxial growth of GaN film on graphene layer deposited on solid substrates as buffer layer were suggested. It should be also plausible that 4|8-GaN might grow on rocksalt substrates that have the same lattice pattern and a sufficiently small lattice constant mismatch with 4|8-GaN, for instance, rectangular UO_2 (2.0%) and MgS (5.8%). Because the localized hole polarons are intimately coupled with the atomic structure around the acceptor [34, 87], it is convincible that the lattice strain would control the hole state of Mg and Be acceptor in 4|8-GaN among polaronic and delocalized state.

5.7 Photoluminescence from multiple polaronic hole states

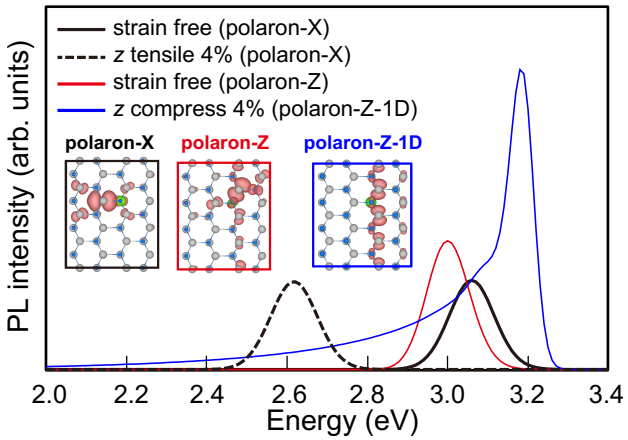

FIGURE 5.4: [From Fig. 4 of Publication III] Simulated photoluminescence line spectra of the (0/) transition of various polaronic hole states of Mg acceptor in 4|8-GaN. Polaron-Z-1D state of 4% compressive strain in z axis is delocalized, thus its geometry relaxation and Huang-Rhys factor $S = 2.2$ is small compared to other polaronic states (polaron-X and polaron-Z) resulting in its wide line shape compared to other polaronic states and large optical transition dipole moment almost 2 times larger than that of other polarons.

Finally, influence of strain control on photoluminescence (PL) of Mg doped 4|8-GaN associated from the change of multiple polaronic hole states were explored. Photoluminescence spectra from the $(0/-)$ acceptor transition of the Mg impurity were simulated, where (0) is the charge neutral state with the trapped hole state and a free electron, and $(-)$ is the singly negative state when the hole state is occupied by one electron. Here, polaron-X, polaron-Z and polaron-1D states of hole carrier trapped at Mg impurity were considered with strain-free, 4% compressive, and 4% tensile strain environment. The simulated PL spectra of Mg impurity for the $(0/-)$ transition were obtained using a one-dimensional approximation as [222, 223]

$$G(\hbar\omega) = C\mu^2\omega^3 \sum_{m,n} w_m(T) |\langle \chi_{em}(Q)| \chi_{gn}(Q)\rangle|^2 \delta(E_{ZPL} + \hbar\omega_{em} - \hbar\omega_{gn} - \hbar\omega), \tag{5.2}$$

where μ is the optical transition dipole moment, C is a normalization factor, ω is the frequency of photon, $w(T)$ is thermal occupation of phonon, $\chi_{g,e}$ is the ionic wave function of the ground and trapped exciton states, and E_{ZPL} is the zero-phonon line (ZPL) energy. Q is an effective one-dimensional displacement determined with $Q^2 = \Sigma m_i d_i^2$ where m_i and d_i are the atomic mass and displacement of i-th atom. In Table 5.2, effective one-dimensional parameters of PL spectra simulation are summarized.

The simulated PL spectra in Figure 5.4 show that both peak position and line shape are dynamically affected by lattice strain. At a first glance, tensile strain along z axis drags down the PL peak in lower energy region with little change of shape. This implies that the tensile strain make the polaron-X state more deeper while its electronic structure has remained unchanged. On the other hand, compressive strain makes PL peak more stronger and sharper. It should be noted that the polaron-Z-1D state is spatially less localized compared to the polaron-X or polaron-Z states that results in small lattice distortions. This induces a sharp PL shape and two times larger transition dipole moment compared with the polaron-X or polaron-Z states. The presented PL spectra implies that impurity luminescence of Mg doped 4|8-GaN can be a spectroscopical barometer of the degree of the lattice strain, which is important for experimental fabrication of 4|8-GaN for optoelectronics.

TABLE 5.2: Effective one-dimensional parameters of $(0/-)$ transition of Mg impurity in 4|8-GaN calculated for polaron-X, polaron-Z and polaron-Z-1D under strain and strain-free conditions. ΔQ is the effective one-dimensional displacement, $\hbar\Omega_{\{g,e\}}$ is the effective phonon energy of the initial (q=-1 with a free electron at the conduction band edge) and final state (q=0).

	ΔQ(amu$^{1/2}$bohr)	$\hbar\Omega_g$ (meV)	$\hbar\Omega_e$ (meV)
polaron-X (strain free)	3.72	22.2	24.0
polaron-Z (strain free)	4.90	16.5	18.0
polaron-Z-1D (z strain -4%, compressive)	1.35	35.3	5.8
polaron-X (z strain 4%, tensile)	5.32	15.9	16.5

	S_g	S_e	μ (eÅ)	E_{ZPL} (eV)
polaron-X (strain free)	10.3	11.1	10.2	3.12
polaron-Z (strain free)	13.2	14.4	10.2	3.06
polaron-Z-1D (z strain -4%, compressive)	2.2	0.4	21.0	3.19
polaron-X (z strain 4%, tensile)	15.1	15.6	10.3	2.68

5.8 Chapter summary

The multiple polaronic and delocalized hole states for Mg and Be impurities in 4|8-GaN were reported from the results of self-interaction corrected density-functional calculations. For the strain-free environment, both Mg and Be impurities have polaronic ground states, where the delocalized states of Mg and Be acceptors are higher in energy by 33.4 meV and 263.2 meV compared with their trapped hole states. A strain control of the Mg impurity hole state in 4|8-GaN was demonstrated, which would offer efficient hole doping engineering of atomically thin 4|8-GaN. Most remarkably, a tensile strain of 2% leads to spontaneous detrapping of the hole state of the Mg impurity, which enables efficient p-type doping of 4|8-GaN. The strain-dependent photoluminescence spectra of Mg impurity in 4|8-GaN provide a spectroscopical barometer of the lattice strain which should be useful for experimental fabrication of optoelectronic devices.

Chapter 6

Concluding remarks

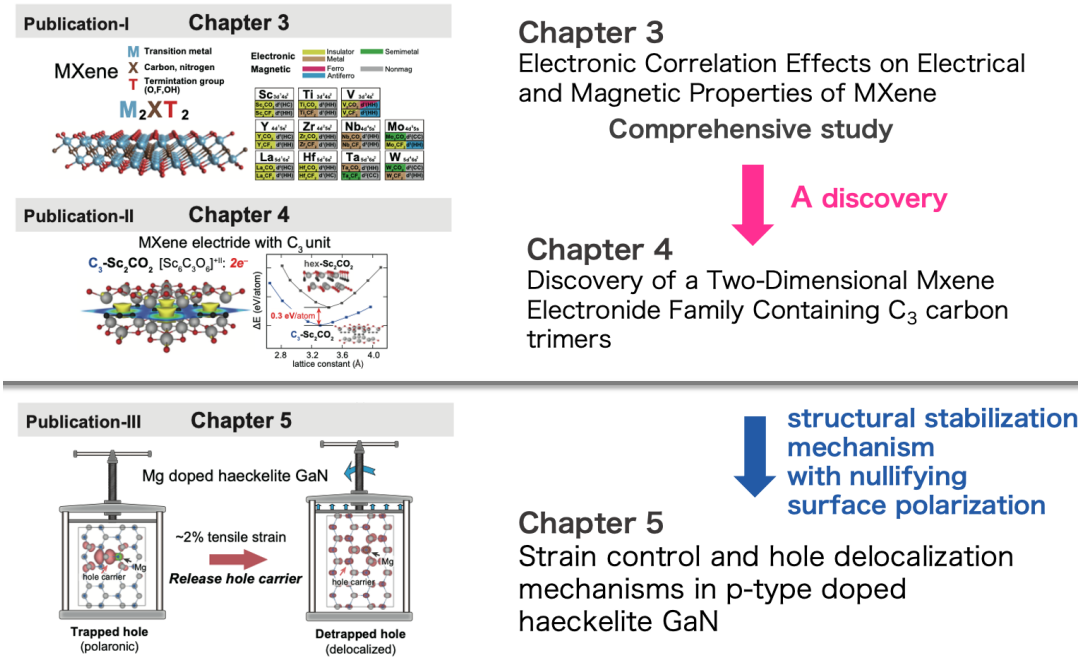

FIGURE 6.1: The main topics of this dissertation with their motifs and connections.

This dissertation has presented a series of *ab initio* calculations of carbide MXenes, MXene electrides, and atomically thin GaN. For practical calculations, density-functional theory (DFT) was employed with its approximate exchange-corrleation functionals. The current work includes a comprehensive description of carbide MXenes in chapter 3, a novel discovery of MXene electrides in chapter 4 and a proof of concept for strain engineering of haeckelite GaN in chapter 5. Chapter 3 presents a systematic study of MXenes containing several physical insights such as correlation between magnetic property and mechanical stability and structural anisotropy associated with charge imbalance of Sc_2CO_2 in its HC structure. Chapter 4 developed the idea of structural stabilization via alternation of electronic property such as electronic polarization and charge balance achieved with Sc_2CO_2 by deforming the structure into the non-polar C_3 structure. Chapter 5 adopts the concept of the structural stabilization by reducing surface polarization to the conventional III-V GaN structure. The polarized bulk GaN in wurtzite phase is further stabilized into its haeckelite structure

when the thickness of GaN is atomically thin. As carrier doping into such semiconductors is a key technology for optoelectronic applications, the hole carrier doping into haeckelite GaN with Mg and Be dopant was examined.

The expected outcomes and contributions of each work are summarized below.

1. In chapter 3, a comprehensive first-principles study of carbide MXenes various theoretical approaches was presented. While strong electron correlation effect of transition metal $3d$ states is not properly considered in a large number of current MXene studies, this work advocates the usage of proper corrections to resort erroneous results affecting the electronic, magnetic, and vibronic properties of MXenes. From novel findings of this work, the strongly coupled features of magnetic phase and dynamical stability of magnetic MXenes were revealed. I expect that these findings should have significant impact on many future DFT calculations for providing reliable predictions that are essential for the material design of MXenes.

2. In chapter 4, a novel discovery of a family of 2D MXene elctrides with C_3 trimer unit was reported. In the MXene field, Sc_2CO_2 has been known as a promising candidate as a ferroelectric material with a world-record strength of ferroelectricity. However, this work clearly reveals that such unrealistically huge ferroelectricity is hardly realized and that such huge charge accumulation in two-dimensional materials would be readily wiped out by deforming or transforming the two-dimensional atomic structure because 2D materials are highly flexible compared to conventional three-dimensional materials. The deformation pattern that nullifies the abnormally huge ferroelectricity was to form the C_3 trimer structure in a $\sqrt{3} \times \sqrt{3}$ commensurate unit in Sc_2CO_2. Astonishingly, the highly stable C_3–Sc_2CO_2 structure acquires an exotic electronic property as an *electride*. This work contributes to the MXene society not only with the novel discovery of C_3 MXene electrides but also by presenting a new principle of material design.

3. In chapter 5, practical predictions of p-type doping of atomically thin haeckelite GaN and its strain control were provided. In fabrication processes of 2D materials, 2D materials are loaded on substrates where various degree of lattice strain with exerted on the 2D materials. Moreover, strain control of 2D material is highly feasible with deformable substrates made of polymers or plastics. Additionally, because carrier trapping in 2D material is typically much easier than that of 3D materials due to the weak screening effect (i.e. low dielectric constant) in the vertical direction. Therefore, localization and trapping of carriers should be extensively controlled by strain engineering.

Bibliography

[1] K. S. Novoselov, A. K. Geim, S. V. Morozov, D. Jiang, Y. Zhang, S. V. Dubonos, I. V. Grigorieva, and A. A. Firsov. "Electric Field Effect in Atomically Thin Carbon Films". In: *Science* 306 (2004), pp. 666–669. DOI: 10.1126/science.1102896.

[2] N. Sethulakshmi, Avanish Mishra, P. M. Ajayan, Yoshiyuki Kawazoe, Ajit K. Roy, Abhishek K. Singh, and Chandra Sekhar Tiwary. "Magnetism in two-dimensional materials beyond graphene". In: *Mater. Today* 27 (2019), pp. 107–122. DOI: 10.1016/j.mattod.2019.03.015.

[3] Tianyu Wang, Quanfeng He, Jingyang Zhang, Zhaoyi Ding, Fucheng Li, and Yong Yang. "The controlled large-area synthesis of two dimensional metals". In: *Mater. Today* 36 (2020), pp. 30–39. DOI: 10.1016/j.mattod.2020.02.003. eprint: 1912.06826.

[4] Sajedeh Manzeli, Dmitry Ovchinnikov, Diego Pasquier, Oleg V. Yazyev, and Andras Kis. "2D transition metal dichalcogenides". In: *Nat. Rev. Mater.* 2 (2017). DOI: 10.1038/natrevmats.2017.33.

[5] Haibin Sun, Jichen Dong, Fengning Liu, and Feng Ding. "Etching of two-dimensional materials". In: *Mater. Today* 42 (2021), pp. 192–213. DOI: 10.1016/j.mattod.2020.09.031.

[6] Mingsheng Xu, Tao Liang, Minmin Shi, and Hongzheng Chen. "Graphene-Like Two-Dimensional Materials". In: *Chem. Rev.* 113 (2013), pp. 3766–3798. DOI: 10.1021/cr300263a.

[7] Ye Chen, Zhanxi Fan, Zhicheng Zhang, Wenxin Niu, Cuiling Li, Nailiang Yang, Bo Chen, and Hua Zhang. "Two-Dimensional Metal Nanomaterials: Synthesis, Properties, and Applications". In: *Chem. Rev.* 118 (2018), pp. 6409–6455. DOI: 10.1021/acs.chemrev.7b00727.

[8] Huanyu Jin, Chunxian Guo, Xin Liu, Jinlong Liu, Anthony Vasileff, Yan Jiao, Yao Zheng, and Shi Zhang Qiao. "Emerging Two-Dimensional Nanomaterials for Electrocatalysis". In: *Chem. Rev.* 118 (2018), pp. 6337–6408. DOI: 10.1021/acs.chemrev.7b00689.

[9] Hadallia Bergeron, Dmitry Lebedev, and Mark C. Hersam. "Polymorphism in post-dichalcogenide two-dimensional materials". In: *Chem. Rev.* 121 (2021), pp. 2713–2775. DOI: 10.1021/acs.chemrev.0c00933.

[10] Babak Anasori and Yury Gogotsi. *2D Metal Carbides and Nitrides (MXenes)*. 2019. ISBN: 9783030190255. DOI: 10.1007/978-3-030-19026-2.

[11] Michael Naguib, Murat Kurtoglu, Volker Presser, Jun Lu, Junjie Niu, Min Heon, Lars Hultman, Yury Gogotsi, and Michel W. Barsoum. "Two-dimensional nanocrystals produced by exfoliation of Ti_3AlC_2". In: *Adv. Mater.* 23 (2011), pp. 4248–4253. DOI: 10.1002/adma.201102306.

[12] Babak Anasori, Yu Xie, Majid Beidaghi, Jun Lu, Brian C. Hosler, Lars Hultman, Paul R.C. Kent, Yury Gogotsi, and Michel W. Barsoum. "Two-Dimensional, Ordered, Double Transition Metals Carbides (MXenes)". In: *ACS Nano* 9 (2015), pp. 9507–9516. DOI: 10.1021/acsnano.5b03591.

[13] Pooja Srivastava, Avanish Mishra, Hiroshi Mizuseki, Kwang-Ryeol Lee, and Abhishek K. Singh. "Mechanistic Insight into the Chemical Exfoliation and Functionalization of Ti_3C_2 MXene". In: *ACS Appl. Mater. Interfaces* 8 (2016), pp. 24256–24264. DOI: 10.1021/acsami.6b08413.

[14] Lu Guo, Xianfen Wang, Zhi Yi Leong, Runwei Mo, Linfeng Sun, and Hui Ying Yang. "Ar plasma modification of 2D MXene $Ti_3C_2T_x$ nanosheets for efficient capacitive desalination". In: *FlatChem* 8 (2018), pp. 17–24. DOI: https://doi.org/10.1016/j.flatc.2018.01.001.

[15] Mohammad Khazaei, Masao Arai, Taizo Sasaki, Chan Yeup Chung, Natarajan S. Venkataramanan, Mehdi Estili, Yoshio Sakka, and Yoshiyuki Kawazoe. "Novel electronic and magnetic properties of two-dimensional transition metal carbides and nitrides". In: *Adv. Func. Mater.* 23 (2013), pp. 2185–2192. DOI: 10.1002/adfm.201202502.

[16] Mohammad Khazaei, Ahmad Ranjbar, Masao Arai, Taizo Sasaki, and Seiji Yunoki. "Electronic properties and applications of MXenes: a theoretical review". In: *J. Mater. Chem. C* 5 (10 2017), pp. 2488–2503. DOI: 10.1039/C7TC00140A. URL: http://dx.doi.org/10.1039/C7TC00140A.

[17] Mohammad Khazaei, Avanish Mishra, Natarajan S. Venkataramanan, Abhishek K. Singh, and Seiji Yunoki. "Recent advances in MXenes: From fundamentals to applications". In: *Curr. Opin. Solid State Mater. Sci.* 23 (2019), pp. 164–178. DOI: 10.1016/j.cossms.2019.01.002.

[18] Sina Abdolhosseinzadeh, Xiantao Jiang, Han Zhang, Jieshan Qiu, and Chuanfang (John) Zhang. "Perspectives on solution processing of two-dimensional MXenes". In: *Mater. Today* 48 (2021), pp. 214–240. DOI: https://doi.org/10.1016/j.mattod.2021.02.010.

[19] Xiaoxue Zhan, Chen Si, Jian Zhou, and Zhimei Sun. "MXene and MXene-based composites: synthesis, properties and environment-related applications". In: *Nanoscale Horiz.* 5 (2020), pp. 235–258. DOI: 10.1039/C9NH00571D.

[20] Chuanfang (John) Zhang, Lorcan McKeon, Matthias P. Kremer, Sang Hoon Park, Oskar Ronan, Andrés Seral Ascaso, Sebastian Barwich, Cormac Coileáin, Niall McEvoy, Hannah C. Nerl, Babak Anasori, Jonathan N. Coleman, Yury Gogotsi, and Valeria Nicolosi. "Additive-free MXene inks and direct printing of micro-supercapacitors". In: *Nat. Commun.* 10 (2019), pp. 1–9. DOI: 10.1038/s41467-019-09398-1.

[21] Ning Zhang, Yu Hong, Sanaz Yazdanparast, and Mohsen Asle Zaeem. "Superior structural, elastic and electronic properties of 2D titanium nitride MXenes over carbide MXenes: a comprehensive first principles study". In: *2D Mater.* 5 (2018), p. 045004. DOI: 10.1088/2053-1583/aacfb3.

[22] Mohammad Khazaei, Masao Arai, Taizo Sasaki, Ahmad Ranjbar, Yunye Liang, and Seiji Yunoki. "OH-terminated two-dimensional transition metal carbides and nitrides as ultralow work function materials". In: *Phys. Rev. B* 92 (2015), p. 075411. DOI: 10.1103/PhysRevB.92.075411.

[23] Mohammad Khazaei, Ahmad Ranjbar, Masao Arai, and Seiji Yunoki. "Topological insulators in the ordered double transition metals $M_2^{'}M^{''}C_2$ MXenes ($M^{'}$ = Mo, W; $M^{''}$ = Ti, Zr, Hf)". In: *Phys. Rev. B* 94 (2016), p. 125152. DOI: 10.1103/PhysRevB.94.125152.

[24] Mohammad Khazaei, Vei Wang, Cem Sevik, Ahmad Ranjbar, Masao Arai, and Seiji Yunoki. "Electronic structures of iMAX phases and their two-dimensional derivatives: A family of piezoelectric materials". In: *Phys. Rev. Mater.* 2 (2018), p. 074002. DOI: 10.1103/PhysRevMaterials.2.074002.

[25] Zakaria Y. Al Balushi, Ke Wang, Ram Krishna Ghosh, Rafael A. Vilá, Sarah M. Eichfeld, Joshua D. Caldwell, Xiaoye Qin, Yu Chuan Lin, Paul A. Desario, Greg Stone, Shruti Subramanian, Dennis F. Paul, Robert M. Wallace, Suman Datta, Joan M. Redwing, and Joshua A. Robinson. "Two-dimensional gallium nitride realized via graphene encapsulation". In: *Nat. Mater.* 15 (2016), pp. 1166–1171. DOI: 10.1038/nmat4742.

[26] Nikhil A. Koratkar. "Materials synthesis: Two-dimensional gallium nitride". In: *Nat. Mater.* 15 (2016), pp. 1153–1154. DOI: 10.1038/nmat4740.

[27] D. Kecik, A. Onen, M. Konuk, E. Gürbüz, F. Ersan, S. Cahangirov, E. Aktürk, E. Durgun, and S. Ciraci. "Fundamentals, progress, and future directions of nitride-based semiconductors and their composites in two-dimensional limit: A first-principles perspective to recent synthesis". In: *Appl. Phys. Rev.* 5 (2018). DOI: 10.1063/1.4990377.

[28] Anan Sun, Shang Peng Gao, and Gong Gu. "Stability and electronic properties of GaN phases with inversion symmetry to inherently inhibit polarization". In: *Phys. Rev. Mater.* 3 (2019), p. 104604. DOI: 10.1103/PhysRevMaterials.3.104604.

[29] John P. Perdew, Kieron Burke, and Matthias Ernzerhof. "Generalized Gradient Approximation Made Simple". In: *Phys. Rev. Lett.* 77 (1996), pp. 3865–3868. DOI: 10.1103/PhysRevLett.77.3865.

[30] Yuping Jia, Zhiming Shi, Wantong Hou, Hang Zang, Ke Jiang, Yang Chen, Shanli Zhang, Zhanbin Qi, Tong Wu, Xiaojuan Sun, and Dabing Li. "Elimination of the internal electrostatic field in two-dimensional GaN-based semiconductors". In: *Npj 2D Mater. Appl.* 4 (2020), pp. 1–7. DOI: 10.1038/s41699-020-00165-1.

[31] John L. Lyons, Anderson Janotti, and Chris G. Van de Walle. "Shallow versus Deep Nature of Mg Acceptors in Nitride Semiconductors". In: *Phys. Rev. Lett.* 108 (2012), p. 156403. DOI: 10.1103/PhysRevLett.108.156403.

[32] Stephan Lany and Alex Zunger. "Dual nature of acceptors in GaN and ZnO: The curious case of the shallow MgGa deep state". In: *Appl. Phys. Lett.* 96 (2010), p. 142114. DOI: 10.1063/1.3383236.

[33] Y. Y. Sun, Tesfaye A. Abtew, Peihong Zhang, and S. B. Zhang. "Anisotropic polaron localization and spontaneous symmetry breaking: Comparison of cation-site acceptors in GaN and ZnO". In: *Phys. Rev. B* 90 (2014), p. 165301. DOI: 10.1103/PhysRevB.90.165301.

[34] Hannes Raebiger, Soungmin Bae, Carlos Echeverría-Arrondo, and Andrés Ayuela. "Control of hole localization in magnetic semiconductors by axial strain". In: *Phys. Rev. Mater.* 2 (2018), p. 024402. DOI: 10.1103/PhysRevMaterials.2.024402.

[35] Shuji Nakamura, Takashi Mukai, Masayuki Senoh, and Naruhito Iwasa. "Thermal Annealing Effects on p-Type Mg-Doped GaN Films". In: *Jpn. J. Appl. Phys.* 31 (1992), pp. L139–L142. DOI: 10.1143/JJAP.31.L139.

[36] Shuji Nakamura, Naruhito Iwasa, Masayuki Senoh, and Takashi Mukai. "Hole Compensation Mechanism of P-Type GaN Films". In: *Jpn. J. Appl. Phys.* 31 (1992), pp. 1258–1266. DOI: 10.1143/JJAP.31.1258.

[37] Ya Ting Shi, Fang Fang Ren, Wei Zong Xu, Xuanhu Chen, Jiandong Ye, Li Li, Dong Zhou, Rong Zhang, Youdou Zheng, Hark Hoe Tan, Chennupati Jagadish, and Hai Lu. "Realization of p-type gallium nitride by magnesium ion implantation for vertical power devices". In: *Sci. Rep.* 9 (2019), pp. 1–9. DOI: 10.1038/s41598-019-45177-0.

[38] J. Buckeridge, C. R.A. Catlow, D. O. Scanlon, T. W. Keal, P. Sherwood, M. Miskufova, A. Walsh, S. M. Woodley, and A. A. Sokol. "Determination of the nitrogen vacancy as a shallow compensating center in GaN doped with divalent metals". In: *Phys. Rev. Lett.* 114 (2015), pp. 1–5. DOI: 10.1103/PhysRevLett.114.016405.

[39] J. L. Lyons, A. Janotti, and C. G. Van De Walle. "Carbon impurities and the yellow luminescence in GaN". In: *Appl. Phys. Lett.* 97 (2010). DOI: 10.1063/1.3492841.

[40] John L. Lyons and Chris G. Van De Walle. "Computationally predicted energies and properties of defects in GaN". In: *Npj Comput. Mater.* 3 (2017), pp. 1–9. DOI: 10.1038/s41524-017-0014-2.

[41] Giacomo Miceli and Alfredo Pasquarello. "Self-compensation due to point defects in Mg-doped GaN". In: *Phys. Rev. B* 93 (2016), pp. 1–11. DOI: 10.1103/PhysRevB.93.165207.

[42] M. Born and R. Oppenheimer. "Zur Quantentheorie der Molekeln". In: *Annalen der Physik* 389 (1927), pp. 457–484. DOI: https://doi.org/10.1002/andp.19273892002.

[43] P. Hohenberg and W. Kohn. "Inhomogeneous Electron Gas". In: *Phys. Rev.* 136 (1964), B864–B871. DOI: 10.1103/PhysRev.136.B864.

[44] R. P. Feynman, N. Metropolis, and E. Teller. "Equations of State of Elements Based on the Generalized Fermi-Thomas Theory". In: *Phys. Rev.* 75 (1949), pp. 1561–1573. DOI: 10.1103/PhysRev.75.1561.

[45] W. Kohn and L. J. Sham. "Self-Consistent Equations Including Exchange and Correlation Effects". In: *Phys. Rev.* 140 (1965), A1133–A1138. DOI: 10.1103/PhysRev.140.A1133.

[46] P. A. M. Dirac. "Note on Exchange Phenomena in the Thomas Atom". In: *Math. Proc. Camb. Philos. Soc.* 26 (1930), pp. 376–385. DOI: 10.1017/S0305004100016108.

[47] D. M. Ceperley and B. J. Alder. "Ground State of the Electron Gas by a Stochastic Method". In: *Phys. Rev. Lett.* 45 (1980), pp. 566–569. DOI: 10.1103/PhysRevLett.45.566.

[48] J. P. Perdew and Alex Zunger. "Self-interaction correction to density-functional approximations for many-electron systems". In: *Phys. Rev. B* 23 (1981), pp. 5048–5079. DOI: 10.1103/PhysRevB.23.5048.

[49] Takao Tsuneda and Kimihiko Hirao. "Self-interaction corrections in density functional theory". In: *J. Chem. Phys.* 140 (2014), 18A513. DOI: 10.1063/1.4866996.

[50] Takao Tsuneda. "Exchange-Correlation Functionals". In: *Density Functional Theory in Quantum Chemistry*. Tokyo: Springer Japan, 2014, pp. 101–124. ISBN: 978-4-431-54825-6. DOI: 10.1007/978-4-431-54825-6_5.

[51] A. Seidl, A. Görling, P. Vogl, J. A. Majewski, and M. Levy. "Generalized Kohn-Sham schemes and the band-gap problem". In: *Phys. Rev. B* 53 (1996), pp. 3764–3774. DOI: 10.1103/PhysRevB.53.3764.

[52] Jianwei Sun, Adrienn Ruzsinszky, and John P. Perdew. "Strongly Constrained and Appropriately Normed Semilocal Density Functional". In: *Phys. Rev. Lett.* 115 (2015), p. 036402. DOI: 10.1103/PhysRevLett.115.036402.

[53] Abhirup Patra, Jefferson E. Bates, Jianwei Sun, and John P. Perdew. "Properties of real metallic surfaces: Effects of density functional semilocality and van der Waals nonlocality". In: *Proc. Natl. Acad. Sci. U.S.A.* 114 (2017), E9188–E9196. DOI: 10.1073/pnas.1713320114.

[54] Richard C. Remsing, Michael L. Klein, and Jianwei Sun. "Dependence of the structure and dynamics of liquid silicon on the choice of density functional approximation". In: *Phys. Rev. B* 96 (2017), p. 024203. DOI: 10.1103/PhysRevB.96.024203.

[55] Mohan Chen, Hsin-Yu Ko, Richard C. Remsing, Marcos F. Calegari Andrade, Biswajit Santra, Zhaoru Sun, Annabella Selloni, Roberto Car, Michael L. Klein, John P. Perdew, and Xifan Wu. "Ab initio theory and modeling of water". In: *Proc. Natl. Acad. Sci. U.S.A.* 114 (2017), pp. 10846–10851. DOI: 10.1073/pnas.1712499114.

[56] Niraj K. Nepal, Liping Yu, Qimin Yan, and Adrienn Ruzsinszky. "First-principles study of mechanical and electronic properties of bent monolayer transition metal dichalcogenides". In: *Phys. Rev. Mater.* 3 (2019), p. 073601. DOI: 10.1103/PhysRevMaterials.3.073601.

[57] Daniil A. Kitchaev, Haowei Peng, Yun Liu, Jianwei Sun, John P. Perdew, and Gerbrand Ceder. "Energetics of MnO_2 polymorphs in density functional theory". In: *Phys. Rev. B* 93 (2016), p. 045132. DOI: 10.1103/PhysRevB.93.045132.

[58] Christopher Lane, James W. Furness, Ioana Gianina Buda, Yubo Zhang, Robert S. Markiewicz, Bernardo Barbiellini, Jianwei Sun, and Arun Bansil. "Antiferromagnetic ground state of La_2CuO_4: A parameter-free ab initio description". In: *Phys. Rev. B* 98 (2018), p. 125140. DOI: 10.1103/PhysRevB.98.125140.

[59] M. Ekholm, D. Gambino, H. J. M. Jönsson, F. Tasnádi, B. Alling, and I. A. Abrikosov. "Assessing the SCAN functional for itinerant electron ferromagnets". In: *Phys. Rev. B* 98 (2018), p. 094413. DOI: 10.1103/PhysRevB.98.094413.

[60] Daniel Mejía-Rodríguez and S. B. Trickey. "Analysis of over-magnetization of elemental transition metal solids from the SCAN density functional". In: *Phys. Rev. B* 100 (2019), p. 041113. DOI: 10.1103/PhysRevB.100.041113.

[61] Gopalakrishnan Sai Gautam and Emily A. Carter. "Evaluating transition metal oxides within DFT-SCAN and SCAN+U frameworks for solar thermochemical applications". In: *Phys. Rev. Mater.* 2 (2018), pp. 1–14. DOI: 10.1103/PhysRevMaterials.2.095401.

[62] Olivia Y. Long, Gopalakrishnan Sai Gautam, and Emily A. Carter. "Evaluating optimal U for 3d transition-metal oxides within the SCAN+U framework". In: *Phys. Rev. Mater.* 4 (2020), pp. 1–15. DOI: 10.1103/PhysRevMaterials.4.045401.

[63] N. Egawa, S. Bae, and H. Raebigar. "Failure of the SCAN functional for systems containing copper with different valences". In: Unpublished manuscript (2021).

[64] Jochen Heyd, Gustavo E. Scuseria, and Matthias Ernzerhof. "Hybrid functionals based on a screened Coulomb potential". In: *J. Chem. Phys.* 118 (2003), pp. 8207–8215. DOI: 10.1063/1.1564060.

[65] J. Hubbard. "The description of collective motions in terms of many-body perturbation theory. II. The correlation energy of a free-electron gas". In: *Proc. Math. Phys. Eng. Sci.* 243 (1958), pp. 336–352. DOI: https://doi.org/10.1098/rspa.1958.0003.

[66] V. I. Anisimov, F. Aryasetiawan, and A. I. Lichtenstein. "First-principles calculations of the electronic structure and spectra of strongly correlated systems: LDA+U method". In: 9 (1997), pp. 767–808. DOI: 10.1088/0953-8984/9/4/002.

[67] Matteo Cococcioni. "Accurate and Efficient Calculations on Strongly Correlated Minerals with the LDA+U Method: Review and Perspectives". In: *Rev. Mineral. Geochem.* 71 (2010), pp. 147–167. DOI: 10.2138/rmg.2010.71.8.

[68] A. I. Liechtenstein, V. I. Anisimov, and J. Zaanen. "Density-functional theory and strong interactions: Orbital ordering in Mott-Hubbard insulators". In: *Phys. Rev. B* 52 (1995), R5467–R5470. DOI: 10.1103/PhysRevB.52.R5467.

[69] S. L. Dudarev, G. A. Botton, S. Y. Savrasov, C. J. Humphreys, and A. P. Sutton. "Electron-energy-loss spectra and the structural stability of nickel oxide: An LSDA+U study". In: *Phys. Rev. B* 57 (1998), pp. 1505–1509. DOI: 10.1103/PhysRevB.57.1505.

[70] P. E. Blöchl. "Projector augmented-wave method". In: *Phys. Rev. B* 50 (1994), pp. 17953–17979. DOI: 10.1103/PhysRevB.50.17953.

[71] G. Kresse and J. Hafner. "Ab initio molecular dynamics for liquid metals". In: *Phys. Rev. B* 47 (1993), pp. 558–561. DOI: 10.1103/PhysRevB.47.558.

[72] G. Kresse and J. Furthmüller. "Efficiency of ab-initio total energy calculations for metals and semiconductors using a plane-wave basis set". In: *Comput. Mater. Sci.* 6 (1996), pp. 15–50. DOI: https://doi.org/10.1016/0927-0256(96)00008-0.

[73] G. Kresse and J. Furthmüller. "Efficient iterative schemes for ab initio total-energy calculations using a plane-wave basis set". In: *Phys. Rev. B* 54 (1996), pp. 11169–11186. DOI: 10.1103/PhysRevB.54.11169.

[74] G. Kresse and D. Joubert. "From ultrasoft pseudopotentials to the projector augmented-wave method". In: *Phys. Rev. B* 59 (1999), pp. 1758–1775. DOI: 10.1103/PhysRevB.59.1758.

[75] A Togo and I Tanaka. "First principles phonon calculations in materials science". In: *Scr. Mater.* 108 (2015), pp. 1–5. DOI: https://doi.org/10.1016/j.scriptamat.2015.07.021.

[76] Abel Carreras, Atsushi Togo, and Isao Tanaka. "DynaPhoPy: A code for extracting phonon quasiparticles from molecular dynamics simulations". In: *Comput. Phys. Commun.* 221 (2017), pp. 221–234. DOI: https://doi.org/10.1016/j.cpc.2017.08.017.

[77] Jingwen Zhu, Ming Wang, Miaoqiang Lyu, Yalong Jiao, Aijun Du, Bin Luo, Ian Gentle, and Lianzhou Wang. "Two-Dimensional Titanium Carbonitride Mxene for High-Performance Sodium Ion Batteries". In: *ACS Appl. Nano Mater.* 1 (2018), pp. 6854–6863. DOI: 10.1021/acsanm.8b01330.

[78] Berna Akgenc. "Intriguing of two-dimensional Janus surface-functionalized MXenes: An ab initio calculation". In: *Comput. Mater. Sci.* 171 (2020), p. 109231. DOI: 10.1016/j.commatsci.2019.109231.

[79] Michael Ashton, Kiran Mathew, Richard G. Hennig, and Susan B. Sinnott. "Predicted Surface Composition and Thermodynamic Stability of MXenes in Solution". In: *J. Phys. Chem. C* 120 (2016), pp. 3550–3556. DOI: 10.1021/acs.jpcc.5b11887.

[80] Soungmin Bae, Natsuki Sugiyama, Takatoshi Matsuo, Hannes Raebiger, Ken Ichi Shudo, and Koichi Ohno. "Defect-Induced Vibration Modes of Ar^{+}-Irradiated MoS_2". In: *Phys. Rev. Appl.* 7 (2017), pp. 1–7. DOI: 10.1103/PhysRevApplied.7.024001.

[81] A Bafekry, B Akgenc, M Ghergherehchi, and F M Peeters. "Strain and electric field tuning of semi-metallic character $WCrCO_2$ MXenes with dual narrow band gap". In: *J. Phys. Condens. Matter* 32 (2020), p. 355504. DOI: 10.1088/1361-648X/ab8e88.

[82] Nuala M. Caffrey. "Effect of mixed surface terminations on the structural and electrochemical properties of two-dimensional $Ti_3C_2T_2$ and V_2CT_2 MXenes multilayers". In: *Nanoscale* 10 (2018), pp. 13520–13530. DOI: 10.1039/c8nr03221a.

[83] Mohammad Khazaei, Ahmad Ranjbar, Mahdi Ghorbani-Asl, Masao Arai, Taizo Sasaki, Yunye Liang, and Seiji Yunoki. "Nearly free electron states in MXenes". In: *Phys. Rev. B* 93 (2016), pp. 1–10. DOI: 10.1103/PhysRevB.93.205125.

[84] Kazuki Osada, Soungmin Bae, Masatoshi Tanaka, Hannes Raebiger, Kenichi Shudo, and Takanori Suzuki. "Phonon Properties of Few-Layer Crystals of Quasi-One-Dimensional ZrS_3 and $ZrSe_3$". In: *J. Phys. Chem. C* 120 (2016), pp. 4653–4659. DOI: 10.1021/acs.jpcc.5b12441.

[85] Uğur Yorulmaz, Ayberk Özden, Nihan K Perkgöz, Feridun Ay, and Cem Sevik. "Vibrational and mechanical properties of single layer MXene structures: A first-principles investigation". In: *Nanotechnology* 27 (2016). DOI: 10.1088/0957-4484/27/33/335702.

[86] Jiaqi Zhou, Mohammad Khazaei, Ahmad Ranjbar, Vei Wang, Thomas D. Kühne, Kaoru Ohno, Yoshiyuki Kawazoe, and Yunye Liang. "Modulation of nearly free electron states in hydroxyl-functionalized MXenes: A first-principles study". In: *J. Mater. Chem. C* 8 (2020), pp. 5211–5221. DOI: 10.1039/c9tc06837f.

[87] Soungmin Bae and Hannes Raebiger. "Critical metal-insulator transition due to nuclear quantum effects in Mn-doped GaAs". In: *Phys. Rev. B* 94 (24 2016), p. 241115. DOI: 10.1103/PhysRevB.94.241115.

[88] Elif Ertekin and Hannes Raebiger. "First-principles methods for defects: state-of-the-art and emerging approaches". In: *Characterisation and Control of Defects in Semiconductors*. Ed. by Filip Tuomisto. IET Publishing, 2019, pp. 289–344. ISBN: 9781785616556. DOI: 10.1049/pbcs045e.

[89] A.C.M. Padilha, H. Raebiger, A. R. Rocha, and G. M. Dalpian. "Charge storage in oxygen deficient phases of TiO2: Defect Physics without defects". In: *Sci. Rep.* 6 (2016), pp. 2–8. DOI: 10.1038/srep28871.

[90] Hannes Raebiger, Stephan Lany, and Alex Zunger. "Electronic structure, donor and acceptor transitions, and magnetism of 3d impurities in In_2O_3 and ZnO". In: *Phys. Rev. B* 79 (2009), pp. 1–7. DOI: 10.1103/PhysRevB.79.165202.

[91] Julien Varignon, Manuel Bibes, and Alex Zunger. "Origin of band gaps in 3*d* perovskite oxides". In: *Nat. Commun.* 10 (2019), pp. 1–11. DOI: 10.1038/s41467-019-09698-6.

[92] Julien Varignon, Manuel Bibes, and Alex Zunger. "Mott gapping in 3d AB O3 perovskites without Mott-Hubbard interelectronic repulsion energy U". In: *Phys. Rev. B* 100 (2019), pp. 1–8. DOI: 10.1103/PhysRevB.100.035119.

[93] Poulami Chakraborty, Tilak Das, Dhani Nafday, Lilia Boeri, and Tanusri Saha-Dasgupta. "Manipulating the mechanical properties of Ti2 C MXene: Effect of substitutional doping". In: *Phys. Rev. B* 95 (2017), pp. 1–9. DOI: 10.1103/PhysRevB.95.184106.

[94] Aurélie Champagne, Lu Shi, Thierry Ouisse, Benoît Hackens, and Jean Christophe Charlier. "Electronic and vibrational properties of V_2C - based MXenes: From experiments to first-principles modeling". In: *Phys. Rev. B* 97 (2018), p. 115439. DOI: 10.1103/PhysRevB.97.115439.

[95] Liang Dong, Hemant Kumar, Babak Anasori, Yury Gogotsi, and Vivek B. Shenoy. "Rational Design of Two-Dimensional Metallic and Semiconducting Spintronic Materials Based on Ordered Double-Transition-Metal MXenes". In: *Journal of Physical Chemistry Letters* 8 (2017), pp. 422–428. DOI: 10.1021/acs.jpclett.6b02751.

[96] Thorsten Schultz, Nathan C. Frey, Kanit Hantanasirisakul, Soohyung Park, Steven J. May, Vivek B. Shenoy, Yury Gogotsi, and Norbert Koch. "Surface Termination Dependent Work Function and Electronic Properties of Ti_3C_2Tx MXene". In: *Chem. Mater* 31 (2019), pp. 6590–6597. DOI: 10.1021/acs.chemmater.9b00414.

[97] Atsushi Togo and Isao Tanaka. "First principles phonon calculations in materials science". In: *Scr. Mater.* 108 (2015), pp. 1–5. DOI: 10.1016/j.scriptamat.2015.07.021.

[98] Yunye Liang, Mohammad Khazaei, Ahmad Ranjbar, Masao Arai, Seiji Yunoki, Yoshiyuki Kawazoe, Hongming Weng, and Zhong Fang. "Theoretical prediction of two-dimensional functionalized MXene nitrides as topological insulators". In: *Phys. Rev. B* 96 (2017), pp. 1–9. DOI: 10.1103/PhysRevB.96.195414.

[99] Hongming Weng, Ahmad Ranjbar, Yunye Liang, Zhida Song, Mohammad Khazaei, Seiji Yunoki, Masao Arai, Yoshiyuki Kawazoe, Zhong Fang, and Xi Dai. "Large-gap two-dimensional topological insulator in oxygen functionalized MXene". In: *Phys. Rev. B* 92 (2015), pp. 1–7. DOI: 10.1103/PhysRevB.92.075436.

[100] Zeng Hui Yang, Haowei Peng, Jianwei Sun, and John P. Perdew. "More realistic band gaps from meta-generalized gradient approximations: Only in a generalized Kohn-Sham scheme". In: *Phys. Rev. B* 93 (2016), pp. 1–9. DOI: 10.1103/PhysRevB.93.205205.

[101] Yoon-Gu Kang. "Ta_2CF_2: a two-dimensional MXene with gigantic giant topological insulator gap". In: Private communication (2021).

[102] Rajesh Kappera, Damien Voiry, Sibel Ebru Yalcin, Brittany Branch, Gautam Gupta, Aditya D. Mohite, and Manish Chhowalla. "Phase-engineered low-resistance contacts for ultrathin MoS2 transistors". In: *Nat. Mater.* 13 (2014), pp. 1128–1134. DOI: 10.1038/nmat4080.

[103] Jianwei Sun, Richard C Remsing, Yubo Zhang, Zhaoru Sun, Adrienn Ruzsinszky, Haowei Peng, Zenghui Yang, Arpita Paul, Umesh Waghmare, Xifan Wu, et al. "Accurate first-principles structures and energies of diversely bonded systems from an efficient density functional". In: *Nature chemistry* 8 (2016), pp. 831–836. DOI: 10.1038/nchem.2535.

[104] Uğur Yorulmaz, İlker Demiroğlu, Deniz Çakir, Oğuz Güseren, and Cem Sevik. "A systematical ab-initio review of promising 2D MXene monolayers towards Li-ion battery applications". In: *J. of Phys.: Energy* 2.3 (2020), p. 032006. DOI: 10.1088/2515-7655/ab9fe3.

[105] Rasoul Khaledialidusti, Babak Anasori, and Afrooz Barnoush. "Temperature-dependent mechanical properties of $Ti_{n+1}C_nO_2$ (n = 1, 2) MXene monolayers: A first-principles study". In: *Phys. Chem. Chem. Phys.* 22 (2020), pp. 3414–3424. DOI: 10.1039/c9cp06721c.

[106] Yoon Gu Kang, Sun Woo Kim, and Jun Hyung Cho. "Competing charge density wave and antiferromagnetism of metallic atom wires in GaN$(10\bar{1}0)$ and ZnO$(10\bar{1}0)$". In: *Phys. Rev. B* 96 (2017), pp. 1–7. DOI: 10.1103/PhysRevB.96.235416.

[107] Sun Woo Kim, Yoon Gu Kang, Hyun Jung Kim, and Jun Hyung Cho. "Comment on "quasi-One-Dimensional Metal-Insulator Transitions in Compound Semiconductor Surfaces"". In: *Phys. Rev. Lett.* 118 (2017), pp. 2016–2017. DOI: 10.1103/PhysRevLett.118.239601.

[108] R. E. Peierls and Louis D. Roberts. "Quantum Theory of Solids". In: *Physics Today* 9 (1956), pp. 29–29. DOI: 10.1063/1.3059963.

[109] Joseph M. Carpinelli, Hanno H. Weitering, E. Ward Plummer, and Roland Stumpf. *Direct observation of a surface charge density wave*. 1996. DOI: 10.1038/381398a0.

[110] George Grüner. "Density waves in solids". In: *Density Waves in Solids* (2018), pp. 1–259. DOI: 10.1201/9780429501012.

[111] Graeme Henkelman, Andri Arnaldsson, and Hannes Jónsson. "A fast and robust algorithm for Bader decomposition of charge density". In: *Comput. Mater. Sci.* 36 (2006), pp. 354–360. DOI: 10.1016/j.commatsci.2005.04.010.

[112] Jun Ho Lee and Jun Hyung Cho. "Instability of one-dimensional dangling-bond wires on H-passivated C(001), Si(001), and Ge(001) surfaces". In: *Surf. Sci.* 605 (2011), pp. L13–L15. DOI: 10.1016/j.susc.2011.01.011.

[113] E. A. Nowadnick, S. Johnston, B. Moritz, R. T. Scalettar, and T. P. Devereaux. "Competition between antiferromagnetic and charge-density-wave order in the half-filled Hubbard-Holstein model". In: *Phys. Rev. Lett.* 109 (2012). DOI: 10.1103/PhysRevLett.109.246404.

[114] Aron J. Cohen, Paula Mori-Sánchez, and Weitao Yang. "Insights into current limitations of density functional theory". In: *Science* 321 (2008), pp. 792–794. DOI: 10.1126/science.1158722.

[115] Mohammad Khazaei, Masao Arai, Taizo Sasaki, Mehdi Estili, and Yoshio Sakka. "Two-dimensional molybdenum carbides: Potential thermoelectric materials of the MXene family". In: *Phys. Chem. Chem. Phys.* 16 (2014), pp. 7841–7849. DOI: 10.1039/c4cp00467a.

[116] Anand Chandrasekaran, Avanish Mishra, and Abhishek Kumar Singh. "Ferroelectricity, Antiferroelectricity, and Ultrathin 2D Electron/Hole Gas in Multifunctional Monolayer MXene". In: *Nano Lett* 17 (2017), pp. 3290–3296. DOI: 10.1021/acs.nanolett.7b01035.

[117] Shiou Jyh Hwu, Robin P. Ziebarth, Samuel von Winbush, Jeff E. Ford, and John D. Corbett. "Synthesis and Structure of Double-Metal-Layered Scandium, Yttrium, and Zirconium Chloride Carbides and Nitrides, $M_2C_{12}C$ and $M_2C_{12}N$". In: *Inorganic Chemistry* 25 (1986), pp. 283–287. DOI: 10.1021/ic00223a011.

[118] Daniel L. Druffel, Matthew G. Lanetti, Jack D. Sundberg, Jacob T. Pawlik, Madeline S. Stark, Carrie L. Donley, Lauren M. McRae, Katie M. Scott, and Scott C. Warren. "Synthesis and Electronic Structure of a 3D Crystalline Stack of MXene-Like Sheets". In: *Chem. Mater* 31 (2019), pp. 9788–9796. DOI: 10.1021/acs.chemmater.9b03722. eprint: 1909.01490.

[119] Yury Gogotsi and Babak Anasori. "The Rise of MXenes". In: *ACS Nano* 13 (2019), pp. 8491–8494. DOI: 10.1021/acsnano.9b06394.

[120] Hyunho Kim and Husam N. Alshareef. "MXetronics: MXene-Enabled Electronic and Photonic Devices". In: *ACS Mater. Lett.* 2 (2020), pp. 55–70. DOI: 10.1021/acsmaterialslett.9b00419.

[121] Rodrigo Mantovani Ronchi, Jeverson Teodoro Arantes, and Sydney Ferreira Santos. "Synthesis, structure, properties and applications of MXenes: Current status and perspectives". In: *Ceram. Int.* 45 (2019), pp. 18167–18188. DOI: 10.1016/j.ceramint.2019.06.114.

[122] S. Bae, Y.-G. Kang, M. Khazaei, K. Ohno, Y.-H. Kim, M.J. Han, K.J. Chang, and H. Raebiger. "Electronic and magnetic properties of carbide MXenes—the role of electron correlations". In: *Mater. Today Adv.* 9 (2021), p. 100118. DOI: https://doi.org/10.1016/j.mtadv.2020.100118.

[123] Lei Zhang, Cheng Tang, Chunmei Zhang, and Aijun Du. "First-principles Screening of Novel Ferroelectric MXene Phases with Large Piezoelectric Response and Unusual Auxeticity". In: *Nanoscale* (2020). DOI: 10.1039/d0nr06609e.

[124] Youngbin Lee, Sung Beom Cho, and Yong Chae Chung. "Tunable indirect to direct band gap transition of monolayer Sc_2CO_2 by the strain effect". In: *ACS Appl. Mater. Interfaces* 6 (2014), pp. 14724–14728. DOI: 10.1021/am504233d.

[125] Avanish Mishra, Pooja Srivastava, Abel Carreras, Isao Tanaka, Hiroshi Mizuseki, Kwang Ryeol Lee, and Abhishek K. Singh. "Atomistic Origin of Phase Stability in Oxygen-Functionalized MXene: A Comparative Study". In: *J. Phys. Chem. C* 121 (2017), pp. 18947–18953. DOI: 10.1021/acs.jpcc.7b06162.

[126] Jie Zhou, Xian Hu Zha, Melike Yildizhan, Per Eklund, Jianming Xue, Meiyong Liao, Per O.Å. Persson, Shiyu Du, and Qing Huang. "Two-Dimensional Hydroxyl-Functionalized and Carbon-Deficient Scandium Carbide, ScC_xOH, a Direct Band Gap Semiconductor". In: *ACS Nano* 13 (2019), pp. 1195–1203. DOI: 10.1021/acsnano.8b06279.

[127] M. A. Ali, M. T. Nasir, M. R. Khatun, A. K.M.A. Islam, and S. H. Naqib. "An ab initio investigation of vibrational, thermodynamic, and optical properties of Sc_2AlC MAX compound". In: *Chinese Physics B* 25 (2016). DOI: 10.1088/1674-1056/25/10/103102.

[128] Haoming Ding, Ke Chen, Lu Chen, Mian Li, Qing Huang, Shiyu Du, Xiao Zhang, Yanqing qin, Yiming Zhang, Youbing Li, and Zhifang Chai. "Molten Salt Synthesis of Nanolaminated Sc_2SnC MAX Phase". In: *J. Inorg. Mater.* 36, 773 (2021), pp. 773–778. DOI: http://www.jim.org.cn/EN/10.15541/jim20200529.

[129] James E Saal, Scott Kirklin, Muratahan Aykol, Bryce Meredig, and Christopher Wolverton. "Materials design and discovery with high-throughput density functional theory: the open quantum materials database (OQMD)". In: *Jom* 65 (2013), pp. 1501–1509. DOI: https://doi.org/10.1007/s11837-013-0755-4.

[130] Scott Kirklin, James E Saal, Bryce Meredig, Alex Thompson, Jeff W Doak, Muratahan Aykol, Stephan Rühl, and Chris Wolverton. "The Open Quantum Materials Database (OQMD): assessing the accuracy of DFT formation energies". In: *Npj Comput. Mater.* 1 (2015), pp. 1–15. DOI: https://doi.org/10.1038/npjcompumats.2015.10.

[131] Anubhav Jain, Shyue Ping Ong, Geoffroy Hautier, Wei Chen, William Davidson Richards, Stephen Dacek, Shreyas Cholia, Dan Gunter, David Skinner, Gerbrand Ceder, and Kristin a. Persson. "The Materials Project: A materials genome approach to accelerating materials innovation". In: *APL Materials* 1 (2013), p. 011002. DOI: 10.1063/1.4812323.

[132] Koichi Momma and Fujio Izumi. "VESTA 3 for three-dimensional visualization of crystal, volumetric and morphology data". In: *J. Appl. Crystallogr.* 44 (2011), pp. 1272–1276. DOI: 10.1107/S0021889811038970.

[133] Daisuke Yoshida, Hannes Raebiger, Ken-ichi Shudo, and Koichi Ohno. "Core Electron Topologies in Chemical Compounds: Case Study of Carbon versus Silicon". In: *Angewandte Chemie* 130 (2018), pp. 7130–7136. DOI: 10.1002/ange.201713108.

[134] Erick A Juarez-Arellano, Björn Winkler, Lkhamsuren Bayarjargal, Alexandra Friedrich, Victor Milman, Daniel R Kammler, Simon M Clark, Jinyuan Yan, Monika Koch-Müller, Florian Schröder, and Miguel Avalos-Borja. "Formation of scandium carbides and scandium oxycarbide from the elements at high-(P, T) conditions". In: *J. Solid State Chem.* 183 (2010), pp. 975–983.

[135] Alexandra Friedrich, Björn Winkler, Erick A Juarez-Arellano, and Lkhamsuren Bayarjargal. "Synthesis of Binary Transition Metal Nitrides, Carbides and Borides from the Elements in the Laser-Heated Diamond Anvil Cell and Their Structure-Property Relations". In: *Materials* 4 (2011), pp. 1648–1692. DOI: https://doi.org/10.3390/ma4101648.

[136] Jing Wang, Hong-Man Ma, and Ying Liu. "$Sc_{20}C_{60}$: a volleyballene". In: *Nanoscale* 8 (2016), pp. 11441–11444.

[137] N H Krikorian, A L Giorgi, E G Szklarz, M C Krupka, and B T Matthias. "Preparation and superconductivity of germanium-stabilized $Sc_{13}C_{10}$". In: *J. less-common met.* 19 (1969), pp. 253–257.

[138] Jongho Park, Jae Yeol Hwang, Kyu Hyoung Lee, Seong Gon Kim, Kimoon Lee, and Sung Wng Kim. "Tuning the Spin-Alignment of Interstitial Electrons in Two-Dimensional Y_2C Electride via Chemical Pressure". In: *J. Am. Chem. Soc.* 139 (2017), pp. 17277–17280. DOI: 10.1021/jacs.7b10338.

[139] Huaqing Huang, Kyung Hwan Jin, Shunhong Zhang, and Feng Liu. "Topological Electride Y_2C". In: *Nano Lett.* 18 (2018), pp. 1972–1977. DOI: 10.1021/acs.nanolett.7b05386.

[140] Changwon Park, Sung Wng Kim, and Mina Yoon. "First-Principles Prediction of New Electrides with Nontrivial Band Topology Based on One-Dimensional Building Blocks". In: *Phys. Rev. Lett.* 120 (2018), p. 26401. DOI: 10.1103/PhysRevLett.120.026401.

[141] Motoaki Hirayama, Satoru Matsuishi, Hideo Hosono, and Shuichi Murakami. "Electrides as a New Platform of Topological Materials". In: *Phys. Rev. X* 8 (2018), p. 31067. DOI: 10.1103/PhysRevX.8.031067. eprint: 1801.03732.

[142] Motoaki Hirayama, Ryo Takahashi, Satoru Matsuishi, Hideo Hosono, and Shuichi Murakami. "Higher-order topological crystalline insulating phase and quantized hinge charge in topological electride apatite". In: *Phys. Rev. Research* 2 (4 2020), p. 043131. DOI: 10.1103/PhysRevResearch.2.043131.

[143] Alfredo Tlahuice-Flores. "Hydrogen Storage on Volleyballene: Prediction of the $Sc_{20}C_{60}H_{70}$ Cluster". In: *J. Phys. Chem. C* 122 (2018), pp. 14971–14978.

[144] L.E. Toth, W. Jeitschko, and C.M. Yen. "The superconducting behavior of several complex carbides and nitrides". In: *J. less-common met.* 10 (1966), pp. 29–32. DOI: 10.1016/0022-5088(66)90041-5.

[145] A. Chowdhury, M. A. Ali, M. M. Hossain, M. M. Uddin, S. H. Naqib, and A. K.M.A. Islam. "Predicted MAX Phase Sc2InC: Dynamical Stability, Vibrational and Optical Properties". In: *Physica Status Solidi (B) Basic Research* 255 (2018), pp. 1–9. DOI: 10.1002/pssb.201700235.

[146] Roald Hoffmann. "C_2 in all its guises". In: *Am. Sci.* 83 (1995), pp. 309–311.

[147] Rainer Pöttgen and Wolfgang Jeitschko. "$Sc_5Re_2C_7$, a Complex Carbide with C_3-Units". In: *Z. Naturforsch. B* 47 (1992), pp. 358–364. DOI: 10.1515/znb-1992-0309.

[148] Takeshi Inoshita, Sehoon Jeong, Noriaki Hamada, and Hideo Hosono. "Exploration for two-dimensional electrides via database screening and ab initio alculation". In: *Phys. Rev. X* 4 (2014), pp. 1–8. DOI: 10.1103/PhysRevX.4.031023.

[149] Biao Wan, Yangfan Lu, Zewen Xiao, Yoshinori Muraba, Junghwan Kim, Dajian Huang, Lailei Wu, Huiyang Gou, Jingwu Zhang, Faming Gao, Ho kwang Mao, and Hideo Hosono. "Identifying quasi-2D and 1D electrides in yttrium and scandium chlorides via geometrical identification". In: *Npj Comput. Mater.* 4 (2018), pp. 1–9. DOI: 10.1038/s41524-018-0136-1.

[150] Jochen Heyd and Gustavo E. Scuseria. "Efficient hybrid density functional calculations in solids: Assessment of the Heyd-Scuseria-Ernzerhof screened Coulomb hybrid functional". In: *J. Chem. Phys.* 121 (2004), pp. 1187–1192. DOI: 10.1063/1.1760074.

[151] D Karhk. *VASP-infrared-intensities*. https://github.com/dakarhanek/VASP-infrared-intensities, 2011.

[152] A. Fonari and S. Stauffer. *raman-sc*. https://github.com/raman-sc/VASP, 2011.

[153] M. Gajdoš, K. Hummer, G. Kresse, J. Furthmüller, and F. Bechstedt. "Linear optical properties in the projector-augmented wave methodology". In: *Phys. Rev. B* 73 (2006), pp. 1–9. DOI: 10.1103/PhysRevB.73.045112.

[154] Abel Carreras, Atsushi Togo, and Isao Tanaka. "DynaPhoPy: A code for extracting phonon quasiparticles from molecular dynamics simulations". In: *Comput. Phys. Commun.* 221 (2017), pp. 221–234. DOI: 10.1016/j.cpc.2017.08.017. eprint: 1708.03435.

[155] Shuichi Nosé. "A unified formulation of the constant temperature molecular dynamics methods". In: *J. Chem. Phys.* 81 (1984), pp. 511–519. DOI: https://doi.org/10.1063/1.447334.

[156] William G Hoover. "Canonical dynamics: Equilibrium phase-space distributions". In: *Phys. Rev. A* 31 (1985), pp. 1695–1697. DOI: 10.1103/PhysRevA.31.1695.

[157] Sune R. Bahn and Karsten W. Jacobsen. "An object-oriented scripting interface to a legacy electronic structure code". In: *Comput. Sci. Eng.* 4 (2002), pp. 56–66. DOI: 10.1109/5992.998641.

[158] Daniel Sheppard, Penghao Xiao, William Chemelewski, Duane D. Johnson, and Graeme Henkelman. "A generalized solid-state nudged elastic band method". In: *J. Chem. Phys.* 136 (2012). DOI: 10.1063/1.3684549.

[159] Penghao Xiao and Graeme Henkelman. "Communication: From graphite to diamond: Reaction pathways of the phase transition". In: *J. Chem. Phys.* 137 (2012). DOI: 10.1063/1.4752249.

[160] Penghao Xiao, Jin Guang Cheng, Jian Shi Zhou, John B. Goodenough, and Graeme Henkelman. "Mechanism of the $CaIrO_3$ post-perovskite phase transition under pressure". In: *Phys. Rev. B* 88 (2013), pp. 1–6. DOI: 10.1103/PhysRevB.88.144102.

[161] Graeme Henkelman, Blas P. Uberuaga, and Hannes Jónsson. "Climbing image nudged elastic band method for finding saddle points and minimum energy paths". In: *J. Chem. Phys.* 113 (2000), pp. 9901–9904. DOI: 10.1063/1.1329672.

[162] Graeme Henkelman and Hannes Jónsson. "Improved tangent estimate in the nudged elastic band method for finding minimum energy paths and saddle points". In: *J. Chem. Phys.* 113 (2000), pp. 9978–9985. DOI: 10.1063/1.1323224.

[163] Q Zheng. *VaspBandUnfolding*. https://github.com/QijingZheng/VaspBandUnfolding, 2020.

[164] E Gürbüz, S Cahangirov, E Durgun, and S Ciraci. "Single layers and multilayers of GaN and AlN in square-octagon structure: Stability, electronic properties, and functionalization". In: *Phys. Rev. B* 96 (2017), pp. 205427–12.

[165] Yuping Jia, Zhiming Shi, Wantong Hou, Hang Zang, Ke Jiang, Yang Chen, Shanli Zhang, Zhanbin Qi, Tong Wu, Xiaojuan Sun, and Dabing Li. "Elimination of the internal electrostatic field in two-dimensional GaN-based semiconductors". In: *Npj 2D Mater. Appl.* (2020), pp. 1–7.

[166] Karel Alexander N. Duerloo, Yao Li, and Evan J. Reed. "Structural phase transitions in two-dimensional Mo-and W-dichalcogenide monolayers". In: *Nature Communications* 5 (2014). DOI: 10.1038/ncomms5214.

[167] Wenbin Li and Ju Li. "Ferroelasticity and domain physics in two-dimensional transition metal dichalcogenide monolayers". In: *Nature Communications* 7 (2016). DOI: 10.1038/ncomms10843.

[168] Aravind Krishnamoorthy, Lindsay Bassman, Rajiv K. Kalia, Aiichiro Nakano, Fuyuki Shimojo, and Priya Vashishta. "Semiconductor-metal structural phase transformation in $MoTe_2$ monolayers by electronic excitation". In: *Nanoscale* 10 (2018), pp. 2742–2747. DOI: 10.1039/c7nr07890k.

[169] Roald Hoffmann and H. JüRgen Meyer. "The electronic structure of two novel carbides, $Ca_3Cl_2C_3$ and Sc_3C_4, containing C_3 units". In: *Z. Anorg. Allg. Chem.* 607 (1992), pp. 57–71. DOI: 10.1002/zaac.19926070112.

[170] Chang Liu, Sergey A. Nikolaev, Wei Ren, and Lee A. Burton. "Electrides: A review". In: *J. Mater. Chem. C* 8 (2020), pp. 10551–10567. DOI: 10.1039/d0tc01165g.

[171] Yoshitake Toda, Sung Wng Kim, Katsuro Hayashi, Masahiro Hirano, Toshio Kamiya, Hideo Hosono, Takeshi Haraguchi, and Hiroshi Yasuda. "Intense thermal field electron emission from room-temperature stable electride". In: *Appl. Phys. Lett.* 87 (2005), pp. 1–3. DOI: 10.1063/1.2149989.

[172] Yoshitake Toda, Hiroshi Yanagi, Eiji Ikenaga, Jung Jin Kim, Masaaki Kobata, Sigenori Ueda, Toshio Kamiya, Masahiro Hirano, Keisuke Kobayashi, and Hideo Hosono. "Work function of a room-temperature, stable electride $[Ca_{24}Al_{28}O_{64}]^{4+}(e^-)_4$". In: *Advanced Materials* 19 (2007), pp. 3564–3569. DOI: 10.1002/adma.200700663.

[173] Masaaki Kitano, Shinji Kanbara, Yasunori Inoue, Navaratnarajah Kuganathan, Peter V. Sushko, Toshiharu Yokoyama, Michikazu Hara, and Hideo Hosono. "Electride support boosts nitrogen dissociation over ruthenium catalyst and shifts the bottleneck in ammonia synthesis". In: *Nature Communications* 6 (2015), pp. 1–9. DOI: 10.1038/ncomms7731.

[174] Daniel L. Druffel, Kaci L. Kuntz, Adam H. Woomer, Francis M. Alcorn, Jun Hu, Carrie L. Donley, and Scott C. Warren. "Experimental Demonstration of an Electride as a 2D Material". In: *J. Am. Chem. Soc.* 138 (2016), pp. 16089–16094. DOI: 10.1021/jacs.6b10114.

[175] Songtao Zhao, Erjun Kan, and Zhenyu Li. "Electride: from computational characterization to theoretical design". In: *Wiley Interdiscip. Rev. Comput. Mol. Sci* 6 (2016), pp. 430–440. DOI: 10.1002/wcms.1258.

[176] T. Koopmans. "Ordering of wave functions and eigenenergies to the individual electrons of an atom". In: *Physica* 1 (1933), pp. 104–113. DOI: https://doi.org/10.1016/S0031-8914(34)90011-2.

[177] J Janak. "Proof that $\partial E/\partial n_i = \varepsilon$ in density-functional theory". In: *Phys. Rev. B* 18 (1978), pp. 7165–7168.

[178] John P. Perdew, Robert G. Parr, Mel Levy, and Jose L. Balduz. "Density-Functional Theory for Fractional Particle Number: Derivative Discontinuities of the Energy". In: *Physical Review Lett.* 49 (1982), pp. 1691–1694. DOI: 10.1103/PhysRevLett.49.1691.

[179] Alan Van Orden and Richard J. Saykally. "Small Carbon Clusters: Spectroscopy, Structure, and Energetics". In: *Chem. Rev.* 98 (1998), pp. 2313–2358. DOI: 10.1021/cr970086n.

[180] Sanchit Chhabra and Thogluva Janardhanan Dhilip Kumar. "Ab Initio Potential Energy Surfaces of C3 Collision with Proton and Quantum Dynamics of Rotational Transition". In: *J. Phys. Chem. A* 122 (2018), pp. 5437–5444. DOI: 10.1021/acs.jpca.8b01588.

[181] Shuichi Nosé. "A unified formulation of the constant temperature molecular dynamics methods". In: *J. Chem. Phys.* 81 (1984), pp. 511–519.

[182] William G Hoover. "Canonical dynamics: Equilibrium phase-space distributions". In: *Phys. Rev. A* 31 (1985), pp. 1695–1697.

[183] Junping Hu, Bo Xu, Chuying Ouyang, Shengyuan A. Yang, and Yugui Yao. "Investigations on V_2C and V_2CX_2 (X = F, OH) monolayer as a promising anode material for Li Ion batteries from first-principles calculations". In: *J. Phys. Chem. C* 118 (2014), pp. 24274–24281. DOI: 10.1021/jp507336x.

[184] Yierpan Aierken, Cem Sevik, O?uz Gülseren, François M. Peeters, and Deniz Çakir. "MXenes/graphene heterostructures for Li battery applications: A first principles study". In: *J. Mater. Chem. A* 6 (2018), pp. 2337–2345. DOI: 10.1039/c7ta09001c.

[185] Aurélie Champagne and Jean Christophe Charlier. "Physical properties of 2D MXenes: From a theoretical perspective". In: *JPhys Materials* 3 (2020). DOI: 10.1088/2515-7639/ab97ee.

[186] Kristin Persson, Yoyo Hinuma, Ying Shirley Meng, Anton Van Der Ven, and Gerbrand Ceder. "Thermodynamic and kinetic properties of the Li-graphite system from first-principles calculations". In: *Phys. Rev. B* 82 (2010), pp. 1–9. DOI: 10.1103/PhysRevB.82.125416.

[187] S. J. Pearton, J. C. Zolper, R. J. Shul, and F. Ren. "GaN: Processing, defects, and devices". In: *J. Appl. Phys.* 86 (1999), pp. 1–78. DOI: 10.1063/1.371145.

[188] B. Jayant Baliga. "Gallium nitride devices for power electronic applications". In: *Semicond. Sci .Technol.* 28 (2013). DOI: 10.1088/0268-1242/28/7/074011.

[189] Xiaofeng Ding, Yang Zhou, and Jiawei Cheng. "A review of gallium nitride power device and its applications in motor drive". In: *CES TEMS* 3 (2019), pp. 54–64. DOI: 10.30941/cestems.2019.00008.

[190] Bejoy N. Pushpakaran, Anitha S. Subburaj, and Stephen B. Bayne. "Commercial GaN-Based Power Electronic Systems: A Review". In: *J. Electron. Mater.* 49 (2020), pp. 6247–6262. DOI: 10.1007/s11664-020-08397-z.

[191] Shuji Nakamura, Takashi Mukai, and Masayuki Senoh. "Candela-class high-brightness InGaN/AlGaN double-heterostructure blue-light-emitting diodes". In: *Appl. Phys. Lett.* 64 (1994), pp. 1687–1689. DOI: 10.1063/1.111832.

[192] Shuji Nakamura. "Background Story of the Invention of Efficient InGaN Blue-Light-Emitting Diodes (Nobel Lecture)". In: *Angew. Chem., Int. Ed. Engl.* 54 (2015), pp. 7770–7788. DOI: 10.1002/anie.201500591.

[193] Michael A. Reshchikov and Hadis Morkoç. "Luminescence properties of defects in GaN". In: *J. Appl. Phys.* 97 (2005), p. 061301. DOI: 10.1063/1.1868059.

[194] S. M. Myers, B. L. Vaandrager, W. R. Wampler, and C. H. Seager. "Influence of ambient on hydrogen release from p-type gallium nitride". In: *J. Appl. Phys.* 95 (2004), pp. 76–83. DOI: 10.1063/1.1629135.

[195] S. Joblot, F. Semond, Y. Cordier, P. Lorenzini, and J. Massies. "High-electron-mobility AlGaN/GaN heterostructures grown on Si(001) by molecular-beam epitaxy". In: *Appl. Phys. Lett.* 87 (2005), pp. 1–3. DOI: 10.1063/1.2067698.

[196] Wen Cheng Ke, Shuo Jen Lee, Shiow Long Chen, Chia Yu Kao, and Wei Chung Houng. "Effects of growth conditions on the acceptor activation of Mg-doped p-GaN". In: *Mater. Chem. Phys.* 133 (2012), pp. 1029–1033. DOI: 10.1016/j.matchemphys.2012.01.128.

[197] Chien-Fong Lo, L. Liu, T. S. Kang, Fan Ren, O. Laboutin, Y. Cao, J. W. Johnson, Alexander Y. Polyakov, N. B. Smirnov, A. V. Govorkov, I. A. Belogorokhov, A. I. Belogorokhov, and S. J. Pearton. "Effect of buffer layer structure on electrical and structural properties of AlGaN/GaN high electron mobility transistors". In: *J. Vac. Sci. Technol. B* 30 (2012), p. 011205. DOI: 10.1116/1.3671020.

[198] Jing Yang, Degang Zhao, Desheng Jiang, Ping Chen, Jianjun Zhu, Zongshun Liu, Lingcong Le, Xiaoguang He, Xiaojing Li, Y. T. Zhang, and G. T. Du. "Influence of hydrogen impurities on p-type resistivity in Mg-doped GaN films". In: *J. Vac. Sci. Technol. B* 33 (2015), p. 021505. DOI: 10.1116/1.4904035.

[199] Fabio Bernardini, Vincenzo Fiorentini, and David Vanderbilt. "Spontaneous polarization and piezoelectric constants of III-V nitrides". In: *Phys. Rev. B* 56 (1997), R10024–R10027. DOI: 10.1103/PhysRevB.56.R10024. eprint: 9705105.

[200] Fabio Bernardini and Vincenzo Fiorentini. "Macroscopic polarization and band offsets at nitride heterojunctions". In: *Phys. Rev. B* 57 (1998), R9427–R9430. DOI: 10.1103/PhysRevB.57.R9427. eprint: 9712245 (cond-mat).

[201] Vincenzo Fiorentini, Fabio Bernardini, Fabio Della Sala, Aldo Di Carlo, and Paolo Lugli. "Effects of macroscopic polarization in III-V nitride multiple quantum wells". In: *Phys. Rev. B* 60 (1999), pp. 8849–8858. DOI: 10.1103/PhysRevB.60.8849.

[202] R. Langer, J. Simon, V. Ortiz, N. T. Pelekanos, A. Barski, R. André, and M. Godlewski. "Giant electric fields in unstrained GaN single quantum wells". In: *Appl. Phys. Lett.* 74 (1999), pp. 3827–3829. DOI: 10.1063/1.124193.

[203] Yi Xie, Yitai Qian, Shuyuan Zhang, Wenzhong Wang, Xianming Liu, and Yuheng Zhang. "Coexistence of wurtzite GaN with zinc blende and rocksalt studied by x-ray power diffraction and high-resolution transmission electron microscopy". In: *Appl. Phys. Lett.* 69 (1996), pp. 334–336. DOI: 10.1063/1.118051.

[204] Martin Frentrup, Lok Yi Lee, Suman Lata Sahonta, Menno J. Kappers, Fabien Massabuau, Priti Gupta, Rachel A. Oliver, Colin J. Humphreys, and David J. Wallis. "X-ray diffraction analysis of cubic zincblende III-nitrides". In: *J. Phys. D Appl. Phys.* 50 (2017). DOI: 10.1088/1361-6463/aa865e.

[205] A. V. Kolobov, P. Fons, J. Tominaga, B. Hyot, and B. André. "Instability and Spontaneous Reconstruction of Few-Monolayer Thick GaN Graphitic Structures". In: *Nano Lett.* 16 (2016), pp. 4849–4856. DOI: 10.1021/acs.nanolett.6b01225.

[206] Marcos Macias, Yenny Lucero Casallas-Moreno, Marlene Camacho-Reynoso, Mario Alberto Zambrano-Serrano, Briseida Guadalupe Pérez-Hernández, C. M. Yee-Rendón, Yuri G. Gurevich, Máximo López-López, and Alfredo Cruz-Orea. "Thermal properties of cubic GaN/GaAs heterostructures grown by molecular beam epitaxy". In: *J. Appl. Phys.* 128 (2020). DOI: 10.1063/5.0016496.

[207] Christoph J.M. Stark, Theeradetch Detchprohm, S. C. Lee, Y. B. Jiang, S. R.J. Brueck, and Christian Wetzel. "Green cubic GaInN/GaN light-emitting diode on microstructured silicon (100)". In: *Appl. Phys. Lett.* 103 (2013). DOI: 10.1063/1.4841555.

[208] Yi Chia Tsai and Can Bayram. "Mitigate self-compensation with high crystal symmetry: A first-principles study of formation and activation of impurities in GaN". In: *Comput. Mater. Sci.* 190 (2021), p. 110283. DOI: 10.1016/j.commatsci.2021.110283.

[209] Sergio Fernández-Garrido, Manfred Ramsteiner, Guanhui Gao, Lauren A. Galves, Bharat Sharma, Pierre Corfdir, Gabriele Calabrese, Ziani De Souza Schiaber, Carsten Pfüller, Achim Trampert, João Marcelo J. Lopes, Oliver Brandt, and Lutz Geelhaar. "Molecular Beam Epitaxy of GaN Nanowires on Epitaxial Graphene". In: *Nano Lett.* 17 (2017), pp. 5213–5221. DOI: 10.1021/acs.nanolett.7b01196.

[210] T. Journot, H. Okuno, N. Mollard, A. Michon, R. Dagher, P. Gergaud, J. Dijon, A. V. Kolobov, and B. Hyot. "Remote epitaxy using graphene enables growth of stress-free GaN". In: *Nanotechnology* 30 (2019), p. 505603. DOI: 10.1088/1361-6528/ab4501.

[211] Andreas Liudi Mulyo, Mohana Krishnappa Rajpalke, Haruhiko Kuroe, Per Erik Vullum, Helge Weman, Bjørn Ove Fimland, and Katsumi Kishino. "Vertical GaN nanocolumns grown on graphene intermediated with a thin AlN buffer layer". In: *Nanotechnology* 30 (2019), pp. 1–17. DOI: 10.1088/1361-6528/aae76b.

[212] Vishnuvarthan Kumaresan, Ludovic Largeau, Ali Madouri, Frank Glas, Hezhi Zhang, Fabrice Oehler, Antonella Cavanna, Andrey Babichev, Laurent Travers, Noelle Gogneau, Maria Tchernycheva, and Jean Christophe Harmand. "Epitaxy of GaN Nanowires on Graphene". In: *Nano Lett.* 16 (2016), pp. 4895–4902. DOI: 10.1021/acs.nanolett.6b01453.

[213] G Callsen, M R Wagner, T Kure, J S Reparaz, M. Bügler, J Brunnmeier, C Nenstiel, A. Hoffmann, M Hoffmann, J Tweedie, Z Bryan, S Aygun, R Kirste, R Collazo, and Z Sitar. "Optical signature of Mg-doped GaN: Transfer processes". In: *Phys. Rev. B* 86 (2012), pp. 1–14. DOI: 10.1103/PhysRevB.86.075207.

[214] W. Götz, N. M. Johnson, J. Walker, D. P. Bour, and R. A. Street. "Activation of acceptors in Mg-doped GaN grown by metalorganic chemical vapor deposition". In: *Appl. Phys. Lett.* 667 (1995), p. 667. DOI: 10.1063/1.116503.

[215] Stephan Lany and Alex Zunger. "Generalized Koopmans density functional calculations reveal the deep acceptor state of NO in ZnO". In: *Phys. Rev. B* 81 (2010), pp. 1–5. DOI: 10.1103/PhysRevB.81.205209.

[216] B Monemar, P P Paskov, G Pozina, C Hemmingsson, J P Bergman, T Kawashima, H Amano, I Akasaki, T Paskova, S Figge, D Hommel, and A Usui. "Evidence for two Mg related acceptors in GaN". In: *Phys. Rev. Lett.* 102 (2009), pp. 10–13. DOI: 10.1103/PhysRevLett.102.235501.

[217] D. Sztenkiel, M. Foltyn, G. P. Mazur, R. Adhikari, K. Kosiel, K. Gas, M. Zgirski, R. Kruszka, R. Jakiela, Tian Li, A. Piotrowska, A. Bonanni, M. Sawicki, and T. Dietl. "Stretching magnetism with an electric field in a nitride semiconductor". In: *Nat. Commun.* 7 (2016), pp. 1–9. DOI: 10.1038/ncomms13232.

[218] Sun-Woo Kim, Yoon-Gu Kang, Hyun-Jung Kim, and Jun-Hyung Cho. "Comment on "Quasi-One-Dimensional Metal-Insulator Transitions in Compound Semiconductor Surfaces"". In: *Phys. Rev. Lett.* 118 (2017), p. 239601. DOI: 10.1103/PhysRevLett.118.239601.

[219] Hendrik J. Monkhorst and James D. Pack. "Special points for Brillouin-zone integrations". In: *Phys. Rev. B* 13 (1976), pp. 5188–5192. DOI: 10.1103/PhysRevB.13.5188.

[220] Mauricio Chagas da Silva, Michael Lorke, Bálint Aradi, Meisam Farzalipour Tabriz, Thomas Frauenheim, Angel Rubio, Dario Rocca, and Peter Deák. "Self-Consistent Potential Correction for Charged Periodic Systems". In: *Phys. Rev. Lett.* 126 (2021), p. 076401. DOI: 10.1103/PhysRevLett.126.076401.

[221] Xavier Gonze and Changyol Lee. "Dynamical matrices, Born effective charges, dielectric permittivity tensors, and interatomic force constants from density-functional perturbation theory". In: *Phys. Rev. B* 55 (1997), pp. 10355–10368. DOI: 10.1103/PhysRevB.55.10355.

[222] Audrius Alkauskas, John L Lyons, Daniel Steiauf, and Chris G. Van De Walle. "First-principles calculations of luminescence spectrum line shapes for defects in semiconductors: The example of GaN and ZnO". In: *Phys. Rev. Lett.* 109 (2012), pp. 1–5. DOI: 10.1103/PhysRevLett.109.267401. eprint: 1303.3043.

[223] Audrius Alkauskas, Matthew D. McCluskey, and Chris G. Van De Walle. "Tutorial: Defects in semiconductors - Combining experiment and theory". In: *J. Appl. Phys.* 119 (2016). DOI: 10.1063/1.4948245.